Tampere University

ANTTI AALTO

Advanced Optical Techniques for Gas Sensing Using Supercontinuum Sources

Tampere University Dissertations 330

Tampere University Dissertations 330

ANTTI AALTO

Advanced Optical Techniques for Gas Sensing Using Supercontinuum Sources

ACADEMIC DISSERTATION
To be presented, with the permission of
the Faculty of Engineering and Natural Sciences
of Tampere University,
for public discussion in the auditorium TB109
of the Tietotalo Building, Korkeakoulunkatu 1, Tampere,
on 6 November 2020, at 12:15 PM.

ACADEMIC DISSERTATION
Tampere University, Faculty of Engineering and Natural Sciences
Finland

Responsible supervisor and Custos	Professor Juha Toivonen Tampere University Finland	
Pre-examiners	Assoc. Prof. Frans Harren Radboud University Netherlands	Assoc. Prof. Erik Vartiainen LUT University Finland
Opponent	Professor Zhipei Sun Aalto University Finland	

The originality of this thesis has been checked using the Turnitin OriginalityCheck service.

Cover design: Roihu Inc.

ISBN 978-952-03-1742-3 (print)
ISBN 978-952-03-1743-0 (pdf)
ISSN 2489-9860 (print)
ISSN 2490-0028 (pdf)
http://urn.fi/URN:ISBN:978-952-03-1743-0

PunaMusta Oy – Yliopistopaino
Vantaa 2020

PREFACE

This work was carried out in the Applied Optics group of the Photonics Laboratory at Tampere University in close collaboration with the Ultrafast Optics group. I acknowledge Academy of Finland, Business Finland (the former Tekes), and the Faculty of Engineering and Natural Sciences for financial support during different stages of the work.

I would like to thank my supervisor Prof. Juha Toivonen for the opportunity to carry out this research. I am sincerely grateful for your guidance and all the kindness, openness, and patience you have shown me over the years. I also thank Prof. Goëry Genty for invaluable help especially in the beginning of this work as well as for the scientific adventures we had around the world. Overall, working in the Photonics Laboratory (the former Optics Lab) has been a lot of fun due in no small part to such easy-going group leaders. I appreciate Dean Martti Kauranen for running the big show and making everything else possible. I want to thank Docent Toni Laurila for valuable discussions and everyone at Valmet for collaboration with the SC lidar. I would also like to thank my co-authors Abba, Caroline, and Piotr for excellent work as well as good times.

This has been a long journey, and I am lucky to have made many friends along the way. Starting from my research assistant days, I thank Jaakko and Tapio, the two older researchers who were always happy to help me. I also thank Miro and Samu, whom I shared a lot of laughter with, and Kalle, my dear eccentric friend. I especially want to mention Johan, who has been a trusted friend since forever, and Mariusz, whom I had so many adventures with. Towards the end of the journey, I am happy for having met Thomas and of course my good friend Léo, both of whom really encouraged me to finish this work. Outside of the laboratory, I would like to thank my dear childhood friends, especially Henri, as well as some newer friends, whom I am privileged to have in my life: Janne, Juha, Mirva, and Pertti.

Finally, I would like to thank my parents Petri and Päivi for giving me this wonderful life and for your unconditional love and support through all of it. Thank you, Ilona and Teemu, for being you. Last, I want to thank Juulia for supporting my growth through difficult times and consistently melting my heart with cuteness.

ABSTRACT

Optical spectroscopy can be used to analyze matter in many contexts: clinical, environmental, industrial, and beyond. Typical light sources employed for this are either spectrally broad lamps and LEDs or monochromatic lasers. Supercontinuum (SC) "white light" lasers constitute a unique class of light sources that combine the beam quality of lasers with a very broad spectral bandwidth. In this thesis, we have explored the potential of these promising instruments in gas sensing applications, such as cavity enhanced absorption spectroscopy and differential absorption lidar. In addition to developing bright and broadband ultraviolet and infrared SC sources and utilizing them in spectroscopic techniques, we have dedicated one study to analyzing SC stability in the long-pulse regime, as these types of sources are efficient yet intrinsically unstable.

In the context of simultaneous ultra-sensitive detection of multiple molecular species in a laboratory, we have researched and improved upon a technique called incoherent broadband cavity-enhanced absorption spectroscopy in two studies. First, by using a custom near-IR SC, we have achieved the highest recorded detection sensitivity for this technique, which is in the ppb-range. Secondly, by using a mid-IR SC, we have demonstrated this technique for the first time in the molecular fingerprint region, with the broadest reported measurement bandwidth, spanning over 400 nm. In the industrial measurement context, we have developed a completely novel short-range SC lidar for remote measurements of temperature and concentration profiles in combustion units. This technique shows a lot of promise, even if the initial measurement accuracy leaves room for improvement.

Although all of these results are somewhat handicapped by the intrinsic instability of the long-pulse SC sources used, we have shown that custom-tailored SC sources can be used to greatly enhance the performance of suitable spectroscopic techniques. They can also enable completely new types of measurement technologies, like the SC lidar, which will hopefully inspire future research.

CONTENTS

SYMBOLS AND ABBREVIATIONS

CARS	coherent anti-Stokes Raman scattering
CCD	charge-coupled device
CEAS	cavity-enhanced absorption spectroscopy
CU	combustion unit
CW	continuous wave
CRDS	cavity ring-down spectroscopy
DAS	direct absorption spectroscopy
DFB	distributed feedback
DIAL	differential absorption lidar
DOAS	differential optical absorption spectroscopy
DSF	dispersion-shifted fiber
FCS	frequency comb spectroscopy
FPI	Fabry-Pérot interferometer
FTIR	Fourier-transform infrared
IBB-CEAS	incoherent broadband cavity-enhanced absorption spectroscopy
ICCD	intensified charge-coupled device
ICOS	integrated cavity-output spectroscopy
LED	light emitting diode
LIBS	laser-induced breakdown spectroscopy
LIDAR	laser radar
LIF	laser-induced fluorescence
MDA	minimum detectable absorption coefficient
MEMS	micro-electro-mechanical system
MI	modulation instability
NDIR	non-dispersive infrared
NICE-OHMS	noise-immune cavity-enhanced optical-heterodyne molecular spectroscopy
OSA	optical spectrum analyzer

PAS	photoacoustic spectroscopy
PCF	photonic crystal fiber
QCL	quantum cascade laser
SC	supercontinuum
SHG	second-harmonic generation
SLD	superluminescent diode
SMF	single-mode fiber
SNR	signal-to-noise ratio
SPM	self-phase modulation
SRS	stimulated Raman-scattering
SSFS	soliton self-frequency shift
STEAM	serial time-encoded amplified microscopy
TDLAS	tunable diode laser absorption spectroscopy
VCSEL	vertical-cavity surface-emitting laser
VECSEL	vertical-external-cavity surface-emitting laser
ZBLAN	ZrF_4-BaF_2-LaF_3-AlF_3-NaF glass
ZDW	zero-dispersion wavelength

a	absorption coefficient
d_0	cavity length
D	optical density
ϵ	mirror loss correction parameter
g	spectrometer response function
I	intensity
λ	wavelength
l	optical path length
M	Pareto-like metric
N	molecular number density
ϱ	mirror losses
R	reflectance
σ	absorption cross-section
τ	optical depth
T	transmittance

LIST OF PUBLICATIONS

Paper I A. Aalto, G. Genty, and J. Toivonen, "Extreme-value statistics in supercontinuum generation by cascaded stimulated Raman scattering," *Optics Express*, vol. 18, no. 2, pp. 1234-1239, 2010.

Paper II A. Aalto, G. Genty, T. Laurila, and J. Toivonen, "Incoherent broadband cavity enhanced absorption spectroscopy using supercontinuum and superluminescent diode sources," *Optics Express*, vol. 23, no. 19, pp. 25225-25234, 2015.

Paper III C. Amiot, A. Aalto, P. Ryczkowski, J. Toivonen, and G. Genty, "Cavity enhanced absorption spectroscopy in the mid-infrared using a supercontinuum source," *Applied Physics Letters*, vol 111, no. 6, p. 061103, 2017.

Paper IV A. Saleh, A. Aalto, P. Ryczkowski, G. Genty, and J. Toivonen, "Short-range supercontinuum-based lidar for temperature profiling," *Optics Letters*, vol. 44, no. 17, pp. 4223-4226, 2019.

OTHER RELATED PUBLICATIONS

RP I T. Mikkonen, C. Amiot, A. Aalto, K. Patokoski, G. Genty, and J. Toivonen, ”Broadband cantilever-enhanced photoacoustic spectroscopy in the mid-IR using a supercontinuum,” Optics letters, vol. 43, no. 20, pp. 5094-5097, 2018.

Patent I J. Toivonen, A. Aalto, M. Sarén, and J. Roppo, "Method for measuring temperature, molecular number density, and/or pressure of a gaseous compound from a thermal device, and a thermal system," U.S. Patent 9,857,345, issued January 2, 2018.

AUTHOR'S CONTRIBUTION

This thesis summarizes four peer-reviewed scientific publications related to supercontinuum light sources and their use in novel gas sensing techniques. The author's contribution to each of these publications is listed below.

Paper I This work is an experimental study on long-pulse supercontinuum stability that quantifies extreme pulse-to-pulse fluctuations. The experiment was planned by G. Genty and J. Toivonen. The author built the experimental setup, conducted the experiments, and analyzed the data. The complementary numerical simulations were run by G. Genty. The author wrote the manuscript with help from G. Genty and J. Toivonen.

Paper II In this publication, we demonstrate incoherent broadband cavity-enhanced absorption spectroscopy in the near-IR using a supercontinuum source with record brightness. All of the co-authors took part in the ideation and planning of the spectrometer setup. The author developed the supercontinuum source based on G. Genty's preliminary numerical simulations. The author built the setup, conducted the experiments, and developed the method for data analysis. The manuscript was prepared by the author. G. Genty and J. Toivonen contributed to finalizing the publication.

Paper III This letter is the first report of incoherent broadband cavity-enhanced absorption spectroscopy using a mid-IR supercontinuum source. The measurement was planned by G. Genty, J. Toivonen, and the author. The author planned the technical implementation. The author prepared the experimental arrangement including the pump laser, the spectrograph, the optical cavity, and the samples. C. Amiot assembled and aligned the experimental setup and conducted the experiments with help from P. Ryczkowski, G. Genty, and the author. The data analysis was performed according to the author's instructions. The manuscript was prepared primarily by C. Amiot and G. Genty.

Paper IV This paper reports on a novel supercontinuum lidar for remote temperature profiling in combustion units. The measurement

principle was planned by J. Toivonen and the author. The author studied the spectral characteristics of high temperature water vapor and developed a suitable supercontinuum source with help from G. Genty. The author developed the first prototype of the measurement setup. The final working measurement setup was built by A. Saleh with help from P. Ryczkowski, J. Toivonen, and the author. The experiments, data analysis, and manuscript preparation were performed primarily by A. Saleh with help from co-authors.

1 INTRODUCTION

Out of all our senses, the sense of sight is arguably the most important, as it provides us with the largest amount of information about our surroundings. And when it comes to technology, optical sensors play a similar role – they constitute the highest bandwidth links between physical and digital worlds. This is reflected in vast majority of global data traffic being visual data. However, the opportunities of this link go way beyond using digital cinematography to stimulate our retinas with internet video. Light can interact with matter in numerous ways, all of which can be used to probe the physical world. And where the cones in our retinas can normally sense light as a combination of three colors corresponding to three partially overlapping wavelength bands of visible electromagnetic radiation, spectroscopic devices can record high-resolution spectra extending from ultraviolet to far-infrared, consisting of light recorded at tens of thousands of individual wavelengths. This makes it possible to harness light to gain vast amounts of information, whether it is about the health of our bodies and environments, about the quality of our consumables, or the materials involved in industrial processes.

In biomedical laboratories all over the world, optical spectroscopy is used to help understand the cause of diseases and to facilitate early diagnosis. Compared to other methods, optical measurements are fast and non-invasive; the results of a test or a screening can often be received in real-time without taking fluid or tissue samples. As an example in dermatology, skin cancer, which is traditionally diagnosed using visual assessment and biopsy, can now be detected using laser-induced fluorescence spectroscopy to identify malignant tissue based on the spectrograph of a patient's skin [1]. Another interesting field of application is the analysis of exhaled breath. Breath is already used in early detection of illnesses such as asthma, based on the amount of exhaled nitric oxide [2], and various dietary disabilities such as fructose intolerance, based on the amount of exhaled hydrogen and methane [3]. However, the number of potential biomarkers in the breath is huge. Breath carries out the metabolites of various cells, whether they belong to healthy tissue, tumors, or microbes, which provides opportunities for non-invasive screening of diseases such as multiple cancers [4]. One can only speculate about the

diagnostic advances made possible if the full "breath fingerprint" consisting of trace levels of hundreds or thousands of different molecules could be easily measured, and this information was combined with modern tools such as big data analytics, machine learning, and artificial intelligence. Obtaining this diagnostic data requires ultra-sensitive measurements of multiple gas components.

Just as healthcare is becoming more data-driven, so are our cities and industries. This overall process of fusing the physical, digital, and biological worlds is sometimes called The Fourth Industrial Revolution or Industry 4.0. In cities and factories, the trend is towards automation and data exchange between machines that are augmented with wireless sensors. Combined with cloud computing and artificial intelligence, autonomous cars, and smart factories will be able to either make decisions on their own, or in cooperation with humans. Optical sensors play a key role in this development by providing the largest amount of data to support these decisions. While cameras and lidar (laser radar) systems are used to identify and locate objects, optical spectroscopy is crucial for identifying materials and quantifying their compositions in real-time. As an example close to home, the Finnish pulp and paper industry is already ahead in this development, making use of optical spectroscopy measurements to monitor important process control parameters such as moisture [5]. In the future, these techniques will most likely see more widespread implementation in many major fields such as chemical and pharmaceutical industries, as well as energy production. Compared to laboratory measurements, where sensitivity and multi-component measurement capabilities are important, industrial measurement devices will have to be compact, robust, and cost-effective in order to be successful. Here, the remote measurement capability is an important edge that optical devices have over other sensor technologies.

Although some spectroscopy techniques make use of environment light that is transmitted, reflected, or emitted by the sample, most techniques rely on active light sources. Various lamps and LEDs can be used to provide efficient illumination covering different regions of the electromagnetic spectrum. These light sources can be bright and spectrally broadband, but they cannot be efficiently collimated to form a narrow beam or focused to a microscopic point. Lasers, on the other hand, are the real precision instruments of light. However, when it comes to spectroscopy, the monochromatic nature of laser light severely limits its applicability. Some lasers, such as the quantum cascade laser, can be tuned so that they scan over a spectral region [6], and optical parameter oscillators can sometimes be used to generate laser-like light at regions far away from the laser

wavelength [7]. However, these sources are still spectrally rather limited and narrowband, as opposed to lamps and LEDs.

Supercontinuum lasers are a unique class of light sources that combine the beam quality of lasers with a broad spectral bandwidth [8]. These truly spectacular sources of light are sometimes called "white lasers" – an example of which can be seen in Figure 1. Despite this nickname, supercontinuum light can in many cases be completely invisible to the human eye, such as when the source is built to cover broad bandwidths in the ultraviolet or infrared. The mid-infrared region is especially interesting, as it opens up possibilities for sensing in the molecular fingerprint region, where light-matter interaction is particularly strong.

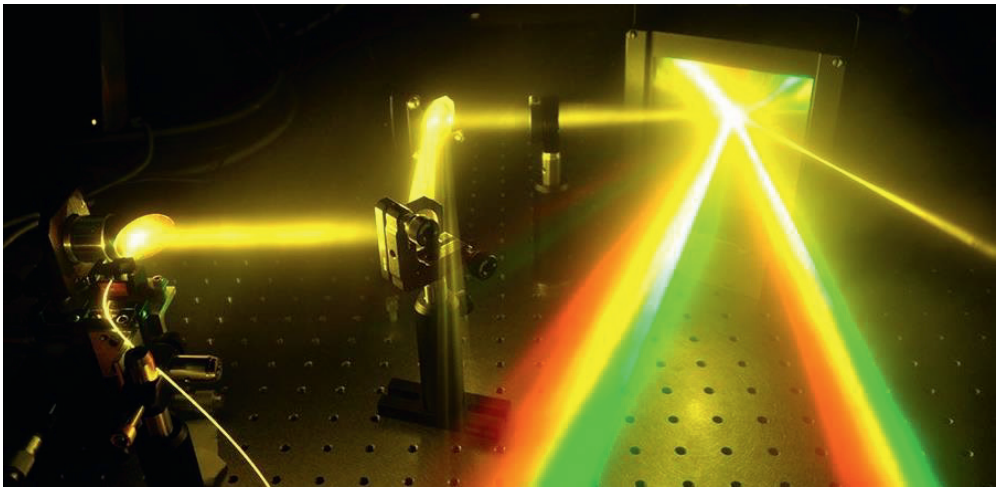

Figure 1. Supercontinuum light that is generated by injecting femtosecond pulses into a photonic crystal fiber. After exiting the fiber seen on the left, the light is collimated, steered with mirrors, and finally focused on a diffraction grating, which causes spectral components to diverge into different directions. Photographed by the author.

Recent advances in laser technology and nonlinear fiber optics have made it possible to build small and cost-effective supercontinuum sources [9], setting the stage for further developing these sources for specific spectroscopic applications. Because supercontinuum light is generated through complex nonlinear dynamics involving exponential amplification of noise, it is important to understand the stability properties of these light sources, so that they can be efficiently utilized. When harnessed properly, supecontinuum light has the potential to both improve the performance of existing spectroscopic techniques, as well as to enable completely novel methods, that were not feasible using conventional light sources.

1.1 Aim and scope of the work

The aim of this thesis is to study and develop supercontinuum sources for gas sensing applications in both laboratory and industrial measurement contexts. The research has been carried out in Photonics Laboratory at Tampere University (previously known as Optics Laboratory at Tampere University of Technology), and was motivated by the unique opportunity of combining the internationally renowned expertise of two research groups into a single research topic. More specifically, this work makes use of the supercontinuum expertise of the Ultrafast Optics group and the spectroscopy expertise of the Applied Optics group. The work began with a statistical analysis of supercontinuum generation in the long-pulse regime and then proceeded to develop new sources in the near- and mid-IR wavelength regions and using these sources in novel gas sensing applications.

The research objectives can be summarized as follows:

- Characterizing pulse-to-pulse spectral fluctuations in nanosecond supercontinuum generation
- Developing a custom high-brightness near-IR supercontinuum source and using it in cavity-enhanced gas sensing
- Developing a mid-IR supercontinuum source for gas sensing in the molecular fingerprint region
- First study of cavity-enhanced absorption spectroscopy using a mid-IR supercontinuum source
- Developing a novel short-range near-IR supercontinuum lidar for temperature profiling in combustion units

The scope of the thesis was limited to developing these light sources and techniques in the laboratory, performing proof-of-concept measurements, and reporting the results in peer-reviewed scientific journals (**Papers I–IV)**. An exception of this is the supercontinuum lidar technique, which we developed in collaboration with Valmet Technologies and patented prior to publishing the scientific paper. **Patent I** is listed in this thesis as a related publication. At the time of writing this thesis, the supercontinuum lidar technique shows significant potential for future industrial applications, and is being further researched in the Applied Optics group. Closely associated with the work is the related publication **RP I**, which describes the first study of photoacoustic spectroscopy using a mid-IR supercontinuum source.

2 ABSORPTION SPECTROSCOPY

Absorption spectroscopy is the most frequently used tool for identifying and quantifying substances using light. In this chapter, we give a brief introduction to absorption spectroscopy as an experimental science. We discuss the origin of absorption lines in the spectrum and how these can be used to identify and quantify specific atoms and molecules in a sample. Finally, we discuss different methods and techniques of optical spectroscopy that are relevant to the techniques we have developed and published in **Papers II – IV**.

2.1 Absorption spectroscopy as an experimental science

Absorption spectroscopy is a field of science and a collection of techniques that is a part of a larger field of optical spectroscopy – a very old branch of physics, which studies the interaction between matter and electromagnetic radiation. The name "spectroscopy" refers to the electromagnetic spectrum, i.e. the distribution of radiation intensity as a function of wavelength or frequency, which is used as a tool for this inquiry. The most common light-matter interactions are emission, absorption, transmission, reflection and scattering. There are more exotic interactions as well, such as the various nonlinear interactions, which are discussed in Chapter 3 in the context of supercontinuum generation. Whereas all of these interactions can act as the basis for their specific spectroscopies, absorption spectroscopy focuses on absorption as the primary means of gaining information about matter.

Perhaps the simplest way to obtain an absorption spectrum is to shine light from a broadband source, such as a lamp, through a gaseous sample and measure the intensity of the transmitted light as a function of wavelength. This technique is called direct absorption spectroscopy (DAS). The spectrum can be measured using a spectrograph containing a dispersive element, such as a prism or a grating, to separate different wavelengths spatially. The measured spectrum consists of the light source spectrum with darker lines corresponding to material-specific

wavelengths where the photons have been absorbed from the incident light. For example, the visible spectrum of sunlight can be seen to contain dark lines corresponding to wavelengths where light has been absorbed by elements in the sun's outer atmosphere. This is demonstrated in Figure 2.

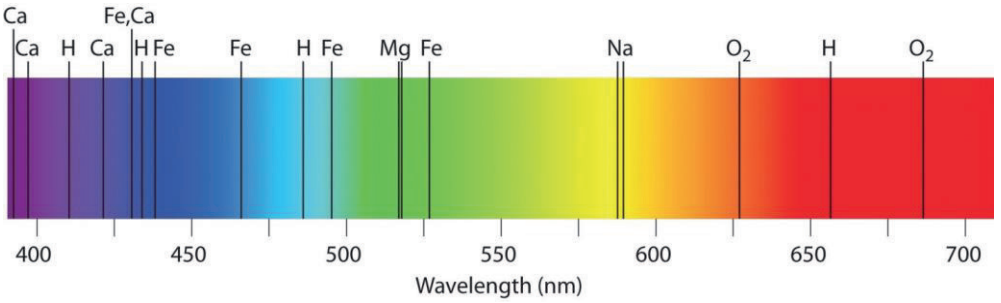

Figure 2. The visible spectrum of sunlight. The characteristic dark lines are due to the absorption of light by elements that are present in the outer part of the sun's atmosphere. [10]

2.2 The Beer-Lambert law

The Beer-Lambert law describes the attenuation of light as it passes through matter. Specifically, it relates the exponential decay of intensity with material parameters. The Beer-Lambert law can be presented in differential or integrated forms, with varying terms and symbols being used in different fields within physics and chemistry. In the context of this work, we use the following form for transmittance, i.e. the ratio of intensities after and before a uniform sample:

$$T(\lambda) = e^{-\tau(\lambda)} \approx 1 - \tau(\lambda), \tag{1}$$

where $T(\lambda)$ is the wavelength-dependent transmittance, $\tau(\lambda)$ is the optical depth, and the approximation is valid for small values of optical depth, such as when measuring very small concentrations of the absorbing molecule. The optical depth is related to sample properties:

$$\tau(\lambda) = \sum_j \sigma(\lambda)_j N_j l, \tag{2}$$

where $\sigma(\lambda)_j$ are the absorption cross-sections of the molecular species, N_j are their number densities, and l is the optical path length. Absorption cross-section

measures the probability of an absorption process. It can be determined experimentally or it can be modeled and calculated using quantum optics. For a detailed quantum mechanical treatment of light-matter interaction, see e.g. Refs. [11, 12]. Next, we will shortly discuss the different types of transitions between quantum-mechanical states that are associated with absorption lines at different regions of the electro-magnetic spectrum.

2.3 Electronic, vibrational, and rotational transitions

The absorption of a photon involves a change of states in the absorbing atom or molecule from a lower to a higher energy state. Absorption is most likely to occur when the frequency (the energy of the photon) matches the corresponding energy difference between the two states, giving rise to a line in the spectrum. In the case of atoms, these states are defined by the arrangement of electrons in atomic orbitals, and absorption corresponds to an electronic transition. Each element has a unique structure of states and therefore a unique set of allowed transitions between them, making it possible to analyze the elemental composition of a sample based on the absorption spectrum. Owing to the large energy difference between electronic states, a high energy photon is required, which is why electronic absorption lines are typically observed at X-ray, ultraviolet, and visible regions of the electromagnetic spectrum.

In the case of molecules, the absorption spectra are more complicated. In addition to electronic states, molecules have states that are defined by modes of vibration and rotation. Just like electronic states, these states are quantized and can be excited by the absorption of a single photon. A nonlinear-shaped molecule with N atoms has $3N - 6$ modes of vibration (a linear molecule has $3N - 5$), which can be excited by absorbing a photon. In terms of energy, vibrational states are more closely packed that the electronic states, thus requiring a smaller energy photon for excitation, which explains why vibrational lines are typically found in the infrared spectral region. Transitions, where a vibrational mode is excited from the ground state to the first excited state, are called fundamental transitions and they typically occur in the mid-infrared. Overtone transitions correspond to excitations to higher states and combination transitions correspond to simultaneous excitation of more than one vibrational mode. These transitions require higher photon energies than the fundamental transitions, and some of their corresponding absorption lines can be found in the near-infrared spectral region.

Compared to vibrational transitions, rotational excitation requires even less energy and rotational lines are found in the microwave region of the spectrum. While microwave photons can only excite rotational transitions, infrared photons can excite transitions that involve a change in both the vibrational and rotational state of the molecule. The molecule ends up in a higher vibrational state, but the final rotational state can be higher or lower, following the molecule-specific selection rules for the transitions between the two quantum mechanical states. Because of this, the art of infrared spectroscopy mainly deals with rotational-vibrational or rovibrational transitions. Instead of seeing a single line for a vibrational transition in the infrared spectrum, a band structure is observed. The band center corresponds to pure vibrational transition, and the branches on both sides correspond to various changes in rotational state that accompany the vibrational transition. The majority of absorption lines measured in this work correspond to rovibrational overtone and combination overtone transitions.

Electronic transitions tend to be accompanied by vibrational and rotational transitions as well, resulting in rotational-vibrational-electronic or rovibronic transitions. Therefore, where the atomic absorption spectra show single lines, the absorption spectra of molecules show bands in the visible and ultraviolet regions. Figure 3 shows a typical energy level diagram of a diatomic molecule along with arrows indicating pure electronic, vibrational, and rotational transitions.

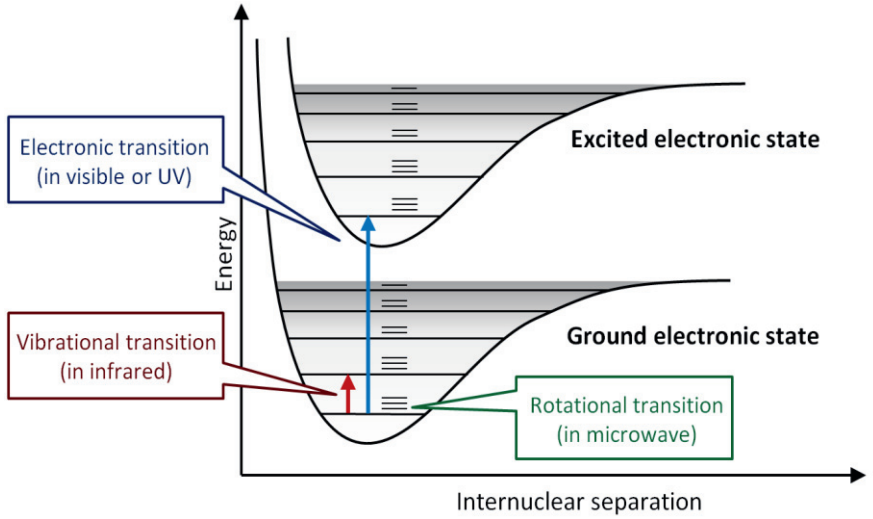

Figure 3. Three types of transitions in a diatomic molecule: electronic, vibrational, and rotational. Rovibrational transitions combine vibrational and rotational transitions, and rovibronic combine all three.

It is important to note that although the transitions take place between discrete quantum mechanical states, absorption lines are never infinitely sharp, but instead are subject to various line broadening mechanisms, such as natural broadening, Doppler broadening, and pressure broadening, which depend on sample pressure and temperature. A thorough treatment of different line broadening mechanisms can be found e.g. in Refs. [11, 13].

Excited molecules will eventually relax either by emitting a photon (spontaneous or stimulated emission) or more commonly through various non-radiative processes. While radiative relaxation forms a basis for many important techniques, such as laser induced fluorescence spectroscopy, non-radiative relaxation in the form of thermal energy is what makes techniques such as laser breakdown spectroscopy and photoacoustic spectroscopy possible.

2.4 Absorption band intensities in the infrared

The intensity of an infrared absorption band is proportional to the square of the change in the molecular electric dipole moment associated with the vibrational transition [14]. This means that a vibrational normal mode is only infrared active if the mode alters the dipole moment of the molecule. Most molecules have strong absorption bands in the mid-infrared region that are associated with fundamental transitions of different vibrational modes and much weaker bands in the near-infrared associated with overtone and combination transitions. This is visualized in Figure 4, which shows the absorption bands of water, methane, and carbon dioxide plotted from one to five microns. One can notice, for example, that the absorption band of CO_2 at 4300 nm is more than five orders of magnitude stronger compared to the band at 1600 nm.

Complex absorption spectra consisting of thousands of lines, such as those shown in Figure 4 can be modeled with the help of spectral databases. The spectra in Figure 4 were calculated using line intensity data from the HITRAN2012 database [15] and a modified Matlab code from Ref. [16]. At the time of writing, HITRAN2016 [17] contains the most complete set of molecular absorption data, combining line parameters of the most common trace gas species in the Earth's atmosphere. There are other similar databases as well, such as HITEMP [18], GEISA [19], PNNL [20], ATMOS [21], and NIST [22]. Detailed instructions on how to use molecular databases and model complete spectra in measurement conditions using line broadening mechanisms can be found e.g. in Refs. [16, 17].

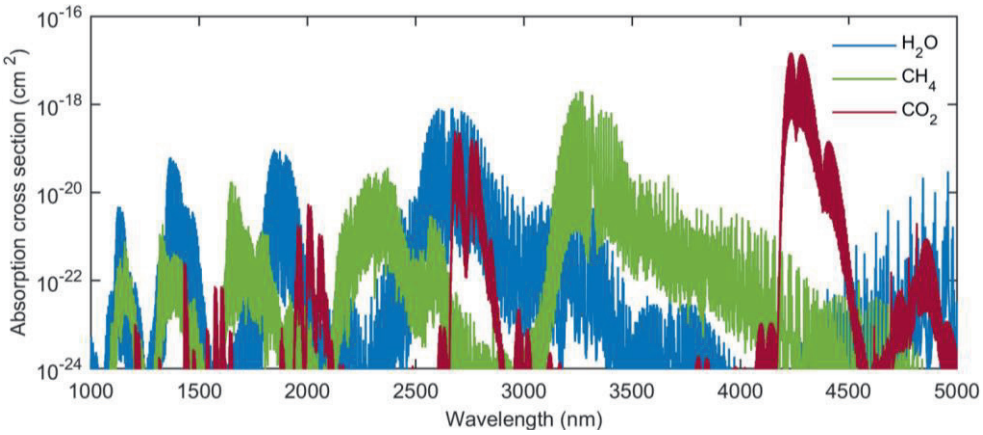

Figure 4. Absorption cross sections of H_2O, CH_4, and CO_2 (in standard conditions) corresponding to rovibrational transitions plotted from near- to mid-infrared. Notice the logarithmic scale.

2.5 Spectroscopic techniques

While the main focus of this work is in the cavity-enhanced and lidar techniques, there are many other optical spectroscopy techniques that they can be compared to, each with their own strengths and weaknesses. Here, we shortly discuss some of them for context. The techniques are chosen on the basis of them being relevant, comparative or complementary to the techniques developed in this work. For a more comprehensive review, the reader is encouraged to see Refs. [11, 23-25].

Direct absorption spectroscopy (DAS) can be used as an umbrella term for various techniques, where the light passes the sample only once and the amount of absorption is used to quantify molecular concentrations or other sample properties. A simple DAS setup might consist of a broadband LED light source, two spectral filters, and a photodetector. If the target molecule has differing absorption characteristics at wavelengths where the two different filters pass light, the concentration can be measured by switching filters and comparing intensity signals. In industrial measurement context, these types of devices are often called non-dispersive infrared (NDIR) sensors. A more advanced dispersive device might contain a fixed grating and an array detector to measure the spectrum. These types of devices can be small, robust and cost-effective but lack selectivity, versatility and sensitivity.

Tunable diode laser absorption spectroscopy (TDLAS) is one of the simplest and most commonly used spectroscopy techniques. In this technique, the

wavelength of a diode laser is tuned to hit an absorption line of a molecule and the transmitted intensity is measured. This intensity is compared to that measured without the absorbing species present or to that measured at another wavelength, where there are no absorption lines. The difference in intensity is then used to calculate the concentration of the molecule. The main weakness of this technique is that it is difficult to measure changes in intensity that are smaller than 10^{-3} due to technical noise [26], which severely limits the sensitivity. This can be improved upon by using modulation schemes, where the laser line is continuously scanned over the absorption line, so that the absorption signal can be measured at a high frequency where technical noise is smaller. The most commonly used lasers are distributed feedback lasers (DFBs), vertical-cavity surface-emitting lasers (VCSELs) vertical-external-cavity surface-emitting lasers (VECSELs), and quantum cascade lasers (QCLs). The selection of available center wavelengths as well as tuning ranges is expanding into the mid-IR [27, 28] and it is likely that TDLAS continues to be an attractive technique in the future, whenever extreme sensitivity is not required.

Differential optical absorption spectroscopy (DOAS) was originally developed to measure trace gas species in the atmosphere over long optical path lengths [29], but the name can be used for any broadband direct absorption measurement, such as measurements carried out in combustion boilers [30]. In an active DOAS measurement, light from a broadband source is shined through a gaseous sample, and the transmitted spectrum is measured using either a scanning monochromator or a spectrograph. In passive atmospheric DOAS measurements, the sun or the moon can act as the light source. The most difficult part of DOAS is the data analysis. The transmitted broadband spectrum can show many overlapping absorption bands, as well as effects from molecular (Rayleigh) and aerosol (Mie) scattering in addition to technical noise and system drifts. However, advanced spectral modeling and fitting methods have been developed for DOAS, making it possible to retrieve concentrations accurately even when the data appears noisy. Nevertheless, the sensitivity of DOAS is still limited by the same problem as DAS and TLDS – it is difficult to detect small changes in intensity caused by small concentrations of absorbing species without enhancing the signal using long measurement distances, multi-pass cells or cavities.

Cavity-enhanced absorption spectroscopy (CEAS) is a term that can be used for various techniques where the sample is placed in a cavity in order to increase the absorption path length and attain very high sensitivities. These techniques can employ a wide range of light sources and detection schemes.

Supercontinuum sources are especially attractive, owing to their broad bandwidth, high brightness, and high beam quality, which is what we have aimed to demonstrate in **Papers II & III**. A review of these techniques is given in Chapter 3.

Fourier transform infrared spectroscopy (FTIR) refers to a group of techniques where dispersive detection of the absorption spectrum is replaced with interferometric detection. More specifically, a Michelson interferometer consisting of a beam splitter and two arms, where the length of one arm be adjusted mechanically, is used. By scanning the movable mirror, an interferogram is measured at the detector arm where the two beams are recombined. The mathematical operation that turns the interferogram into a spectrum is called Fourier transform. FTIR has three major advantages over dispersive spectrometers [11]. Firstly, the wavelength axis can be self-calibrated using a laser of known frequency (Connes' advantage). Secondly, the circular aperture has a much larger area compared to the slit of a monochromator, allowing higher throughput (Jacquinot's advantage). Thirdly, all wavelengths hit the detector at the same time, as opposed to a wavelength scanning (Fellgett's advantage). The last two advantages allow for higher signal-to-noise ratios per measurement time, resulting in higher sensitivity or faster measurements. Typical light sources are broadband black body radiators and discharge lamps, both of which require large optics in order to form a beam with acceptable quality and pass it through the interferometer. On the other hand, supercontinuum sources have excellent beam quality and brightness, making them attractive for both increasing the signal-to-noise ratio and miniaturization of the spectrometer. On the detection arm, pyroelectric detectors are typically used in far-to-mid-infrared devices, while photodiodes are can be used in the near-IR. FTIR can be used in combination with cavity-enhanced [31] or photoacoustic techniques (**RP I**) to increase the sensitivity.

Frequency comb spectroscopy (FCS) utilizes optical frequency combs, which are pulsed light sources whose spectrum consists of hundreds of thousands of precisely equidistant lines. In recent years, frequency combs have enabled some truly novel spectroscopic techniques, and they are being researched extensively [32]. For example, dual-frequency comb spectroscopy [33-36] makes it possible to record broadband absorption spectra using a photodetector and radio frequency electronics, without the need for any dispersive elements or scanning interferometers. This is done by measuring the beat notes generated by two combs that have slightly different line spacings. Frequency combs can be mode-matched with external cavities, so that the optical throughput of cavity enhanced absorption

spectroscopy can be greatly increased. This technique is further discussed in the review in the beginning of Chapter 3. Frequency comb light sources are typically mode-locked femtosecond lasers, such as Ti:sapphire solid-state lasers or Er:fiber lasers, and their spectra can be extended to cover different regions from UV to mid-IR using nonlinear processes and supercontinuum generation [37-39].

Raman spectroscopy is based on the inelastic form of scattering called Raman scattering. When light from a monochromatic source hits a sample, a small amount (typically in the order of 10^{-7}) can be converted to light with a slightly lower or higher wavelength through Raman scattering [14]. This scattering results from the interaction of light with molecular (or crystal) vibrations and the shift in photon energy gives information about the vibrational modes of the system. Raman spectroscopy can be seen as a complementary technique to infrared absorption spectroscopy. Where infrared spectroscopy detects vibrations involving a change in dipole moment, Raman spectroscopy detects vibrations involving a change in polarizability. This results in different selection rules, making it possible for Raman spectrometers to probe vibrational modes that are not active in the IR absorption spectrum. Light sources for Raman spectroscopy are typically continuous wave (CW) lasers operating in the visible and near-IR regions of the spectrum. Detection can be done with dispersive or FTIR spectrometers. Because of the extremely weak scattering signal, care must be taken to filter out the much stronger Rayleigh scattered light, and to avoid exciting fluorescence in any of the sample species. The signal can be made stronger with stimulated scattering using a technique called coherent anti-Stokes Raman scattering (CARS) spectroscopy that employs two pulsed lasers [14, 23]. Compared to IR absorption spectroscopy, both Raman spectroscopy and CARS are very spatially sensitive and suitable for sensing substances in all states.

Laser-induced fluorescence (LIF) is a technique where laser light is used to excite sample molecules onto higher electronic states, and the photons released through radiative relaxation are detected. Most of these photons have lower energy compared to the laser, resulting from the fact that molecules that are excited to higher rovibronic states can undergo many stages of nonradiative decay before the eventual radiative relaxation. A major benefit of LIF is that the signal is basically background free, i.e. fluorescence light is observed after the laser pulse, it is emitted in all directions, and it has a different wavelength. This makes LIF more sensitive than direct absorption spectroscopy and it can achieve sensitivities that are comparable to cavity-enhanced methods. LIF is also very spatially sensitive and is often used to analyze biological samples, such as tumors [1]. Because the

technique requires electronic excitation, lasers operating in the UV and visible regions of the spectrum are used.

Laser-induced breakdown spectroscopy (LIBS) uses short and intense laser pulses to heat and atomize the surface of the sample, producing a small plasma plume. This plume contains excited atoms and ions, which will relax after a short time by emitting photons. The emitted light is collected and analyzed using a spectrograph, giving qualitative and quantitative information about the elemental composition of the sample. LIBS is a very convenient and moderately sensitive technique that requires very little sample preparation and can be used to analyze samples in virtually any form. Because of the similarities between Raman spectroscopy, LIF, and LIBS, it is possible to build instruments that combine two or three of these techniques [40].

Photoacoustic spectroscopy (PAS) is in principle similar to LIF and LIBS, i.e. they are all based on exciting atoms or molecules to higher states and measuring the results of the relaxation process. As opposed to LIF and LIBS, PAS is based on nonradiative relaxation, where some or all of the absorbed energy is converted to thermal energy. This results in a local change in the temperature and pressure of the sample, creating an acoustic wave which can be measured using a sensitive microphone. Photoacoustic spectroscopy is one of the most sensitive optical spectroscopy techniques, especially when an acoustically resonant chamber or a cantilever based detector is used [41]. The main benefit of the photoacoustic method is that instead of having to measure very small changes in an optical signal, as in direct absorption measurements, the photoacoustic spectroscopy is background free, i.e. when there is no absorption, there is no sound. The signal-to-noise ratio in PAS scales linearly with light source intensity, as opposed to the typical square-root dependence in absorption spectroscopy. This makes it an attractive candidate for high brightness supercontinuum light sources, which is the topic of **RP I**.

A lidar is a remote-measurement device, whose name can be considered an acronym for either "laser radar" or "light detection and ranging" [42]. A simple ranging transceiver works by transmitting laser pulses towards a target, and then recording the time it takes for the backscattered pulses to return and hit the detector. These types of devices can be used to map the environment as a digital 3D point cloud, with applications ranging from astronomy and forestry to autonomous driving and urban design. The velocity of objects (e.g. wind speed) can be mapped by measuring the Doppler-shift of backscattered light; this is typically done using a technique known as heterodyne detection. A differential

absorption lidar (DIAL) is a device that allows for remote spectroscopic measurements over large distances. It functions by recording the time-dependent backscattered signal at two wavelengths, selected so that the gas of interest only has strong absorption at one wavelength. Comparing these two signals makes it possible to profile the molecular concentration, or other gas parameters such as temperature and pressure. Differential absorption lidars are typically used in atmospheric measurements with tunable lasers as light sources, but the technique lends itself to short-range measurements using supercontinuum light sources as well, which is the topic of **Paper IV**.

Figure 5 gives a visual summary of these techniques by positioning them on an applicability-versus-sensitivity graph. The positions are based on ad hoc approximations of factors such as instrument cost, size, complexity; measurement selectivity and accuracy; real-time-, multi-component- and remote measurement capabilities; and spatial sensitivity. Some of these techniques, such as frequency comb spectroscopy, are undergoing rapid development, making it especially difficult to pinpoint their position. One way to describe the work presented in this thesis is that we aim to improve the colored techniques by using supercontinuum sources, essentially moving them closer to the top right corner of this graph.

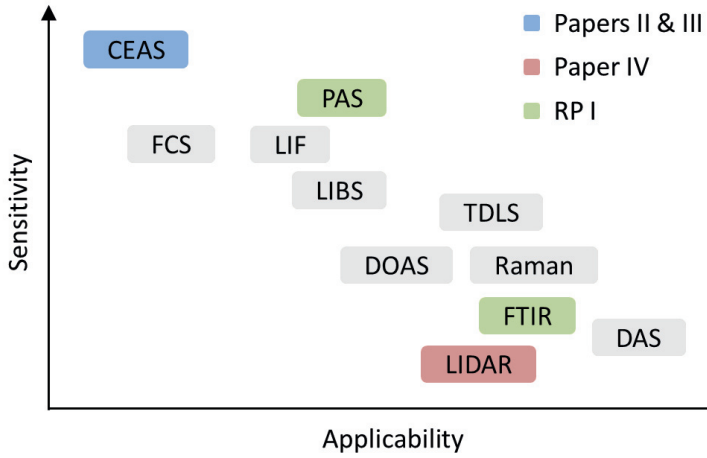

Figure 5. Qualitative comparison of different spectroscopic techniques in terms of sensitivity and applicability. The CEAS techniques of **Papers II & III** are best suited for laboratory measurements, whereas the LIDAR and photoacoustic techniques of **Paper IV** and **RP I**, for example, have more potential for industrial applications.

3 SUPERCONTINUUM GENERATION USING LONG PULSES

Supercontinuum light sources possess a unique combination of high spectral brightness and spatial coherence together with a broad spectral bandwidth. In other words, they combine a laser-like beam quality with a lamp-like breadth of wavelengths, making them ideal candidates for spectroscopic applications. Unfortunately, only femtosecond supercontinuum sources are intrinsically stable. In the long-pulse regime, the sources are inherently unstable, limiting their usability, but also making them an interesting experimental playground for studying nonlinear noise amplification mechanics, which can help in understanding extreme amplitude events in other mediums such as rogue waves in the ocean. This chapter begins with a short overview of the history of the supercontinuum, after which the physical mechanisms of the supercontinuum generation process are discussed. We then focus on supercontinuum stability in the long-pulse regime and discuss the experimental results of **Paper I**. This analysis helps in interpreting the role of noise in the results presented in the subsequent chapters.

3.1 Short history of supercontinuum light sources

Supercontinuum generation is a process where laser light is turned into light with a very broad spectral bandwidth. The generation of new spectral components is one of the core features of nonlinear optics. The field was born in the 1960's, one year after the invention of the Q-switched pulsed laser, when Franken et al. reported on a surprising observation of the appearance of a new beam with double the frequency after focusing intense laser pulses into a quartz sample [43]. The phenomenon is now known as second harmonic generation (SHG). It results from the nonlinear polarization of matter – the effect where the polarization does not respond linearly to the electric field, and higher-order factors of susceptibility come into play. A 1970-paper by Alfano et al. reports on a generation of a "white-light source" between 400 and 700 nanometers, and is considered the first report of a

supercontinuum [44]. This continuum was generated by focusing gigawatt-picosecond pulses from a frequency-doubled Nd:glass laser into borosilicate glass, and the effect was attributed to stimulated Raman scattering (SRS) and self-phase modulation (SPM). The term "supercontinuum" was coined ten years later in a publication by the same group [45].

The invention of the single-mode fiber (SMF) in the 1970's made it possible to greatly increase the optical path length over which tightly confined laser pulses can interact matter, effectively birthing the field of nonlinear fiber optics and bringing supercontinuum technology closer to practical applications. However, the real turning point was the invention of the photonic crystal fiber (PCF) in 1996 [46]. This new type of microstructured silica fiber contained air holes in the cladding, making it possible to have more control over the dispersive and nonlinear properties of the fiber [47-50]. A few years later, the first octave-spanning supercontinuum was generated from 400 to 1600 nanometers by pumping an engineered PCF with femtosecond pulses from a titanium-sapphire laser [51] – see Figure 1 for visual reference. Since then, supercontinuum generation has been researched extensively, and the relevant nonlinear mechanisms are now well known [9]. Because the dynamics behind the process are complex and difficult to follow experimentally, numerical simulations have played a major role in reaching this understanding. In recent years, the main research focus has been in understanding and improving the supercontinuum coherence [52-58], and extending the wavelength range further into UV [56, 59, 60] and mid-IR [61-69] regions.

3.2 Mechanisms of supercontinuum generation

Supercontinuum light can be generated using a wide variety of different types of pump lasers and nonlinear fibers. The pulse width can range from femtoseconds to nanoseconds, and in some nonlinear mediums, even continuous-wave light can be used [70, 71]. One or more pump sources can be used with laser wavelengths ranging from ultraviolet [72] to the mid-infrared [62]. The nonlinear fiber can be single- or multi-mode with cladding geometries ranging from regular step-index [73, 74] fibers to various types of microstructured fibers such as the hollow core PCF fiber [56, 75, 76]. When extending the supercontinuum to the mid-IR, normal silica fibers become opaque, and more exotic soft glasses such as tellurite [66], fluoride [67, 77], and chalcogenide [68, 69, 78] must be used.

The dynamics of supercontinuum generation can be categorized into four groups based on pulse width (short vs. long) and dispersion regime (normal vs. anomalous). The short-pulse regime is extremely interesting for the generation of coherent femtosecond supercontinuum frequency combs [52-54]. However, most lasers emit light that is either continuous-wave or consists of nanosecond or picosecond pulses, which is why the long-pulse regime is important for practical applications. It is also the regime where all of the supercontinuum sources developed in this work operate. Here, we will shortly discuss the basic dynamics of supercontinuum generation using long pulses. A more thorough treatment covering all the different regimes can be found in Refs. [8, 9, 37].

When intense pico- or nanosecond pulses (i.e. long pulses) are launched into the normal dispersion regime of a fiber, the spectral broadening is dominated by stimulated Raman scattering (SRS). Stimulated Raman scattering broadens the spectrum towards the red by transferring energy from the pump wave to the Stokes wave, which grows exponentially from either spontaneous Raman scattering or input noise. The peak of the Raman gain curve is roughly at 13.5 THz for silica, designating the most probable spectral location for the first Stokes wave. When the Stokes wave becomes strong enough, it will start acting as a pump wave for a new SRS process, and light the red side of the Stokes wave gets amplified, generating an another, further red-shifted peak in the spectrum. This cascade continues until the end of the fiber is reached or the intensity of the Stokes wave drops below the SRS threshold through of dispersive pulse broadening or material attenuation. The result is the so-called Raman continuum, which is studied in **Paper I**. If the Raman cascade reaches the zero-dispersion wavelength of the fiber, anomalous dispersion regime dynamics start dominating the spectral broadening process.

In the anomalous dispersion regime, the spectral broadening of long pulses is dominated by modulation instability (MI) and soliton dynamics. The process starts with modulation instability amplifying the random noise on top of the pulse envelope. This modulation grows exponentially, eventually breaking the pulse, or even CW light, into a train of solitons, each having a random duration and amplitude. If the spectrum of a soliton extends over to the normal dispersion regime of the fiber, it can shed some of its energy towards the blue end of the spectrum in the form of dispersive waves. Solitons undergo continuous soliton self-frequency shift (SSFS), effectively shifting their central wavelength towards the red through self-seeded stimulated Raman scattering. Random solitons traveling at different group velocities will also experience collisions, during which the spectrum gets momentarily wider, causing SRS to shift even more energy towards the red

and more dispersive waves being shed in the vicinity of the ZDW. The solitons keep shifting towards longer wavelengths until the physical end of the fiber or the end of the transparency window of the medium is reached. This results in a broadband, predominately red-shifted soliton continuum. The supercontinuum sources developed in **Papers II–IV** were generated mainly through these dynamics.

3.3 Supercontinuum stability in the long-pulse regime

Since the process of supercontinuum generation in the long pulse regime starts from the amplification of input noise, any broadband spectrum generated this way will show large pulse-to-pulse fluctuations, which are heavily dependent on the input conditions. The time-averaged spectrum can still be relatively stable, as it consists of thousands of pulses, which makes e.g. slow-scanning spectroscopic measurements feasible even with the source having large shot-to-shot fluctuations. Nevertheless, understanding the noise amplification mechanics of supercontinuum generation and characterizing the spectral and temporal fluctuations is important for the development of more stable sources. This research has led to various new schemes for stabilizing the source [55-58], which has enabled long pulse SC sources to be used e.g. in ultrafast serial time-encoded amplified microscopy (STEAM) [79].

In the last ten or so years, there has been significant research interest in "optical rogue waves" – extremely intense temporal events observed at the output of a nonlinear fiber. The interest started in 2007 after Solli et al. published an original paper in Nature with the above-quoted title [80]. The authors pointed out the connection between these intense optical events and oceanic rogue waves – the large and destructive waves that seem to appear out of nowhere. Both of these nonlinear systems are described by the nonlinear Schrödinger equation, and in both systems modulation instability and soliton dynamics can give rise to these extreme events. Studying one system can help to understand the other. Rogue waves are associated with L-shaped, fat-tailed, extreme value statistics, indicating that while they are rare, they occur much more often compared to what Gaussian statistics or common intuition might suggest. Rogue waves and rogue-wave-like statistics have since been reported in various regimes of nonlinear pulse propagation such as Raman amplifiers [81] or during laser filamentation in air [82], and studying them has practically started a new subfield within optics [83, 84].

In **Paper I**, we report on an experimental study of extreme spectral fluctuations observed in a supercontinuum that is generated in the normal dispersion regime through cascaded stimulated Raman scattering. By measuring and analyzing the single-shot spectra, we show that the statistics of these fluctuations are heavily wavelength-dependent, evolving from Gaussian in the saturated region near the pump to L-shaped extreme value distribution near the unsaturated red edge of the spectrum. Next, we will shortly discuss the UV supercontinuum source, the setup for acquiring single-shot spectra, and the experimental results of this work.

3.3.1 UV supercontinuum source

Ultraviolet supercontinuum sources are interesting for many applications such as spectroscopy and microscopy [85]. Perhaps the simplest way to generate a UV supercontinuum source is to use a short-wavelength pump together with a narrow-core single-mode fiber in order to generate a cascaded Raman continuum. This method is especially effective in the UV because SRS is stronger at shorter wavelengths. The supercontinuum source studied in **Paper I** was generated by using an electro-optically Q-switched, frequency-tripled Nd:YAG laser that produces 8-ns pulses at 355 nm. The pulses were launched into a 40-meter-long single-mode polarization-maintaining fiber that has a core diameter of 2.3 μm. Prior to coupling, the pulse energy was attenuated to around 2 μJ to prevent damaging the fiber. The coupling was achieved with a combination of a UV microscope objective and an XYZ-flexure stage, with an average coupling efficiency of 50 %. The result was a broadband UV supercontinuum generated mainly through cascaded SRS, as described above in Chapter 3.2. Figure 6 shows the full experimental setup and a typical single-shot spectrum.

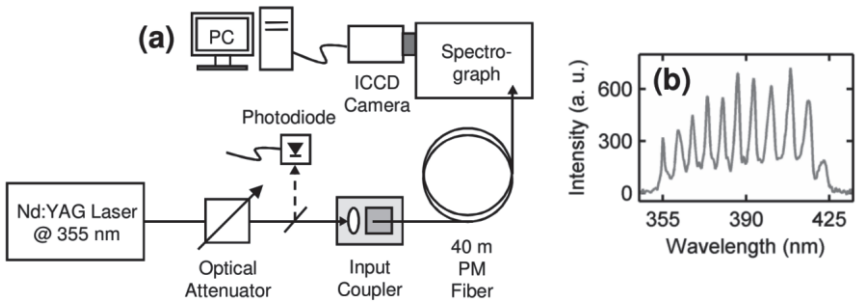

Figure 6. (a) The experimental setup for UV supercontinuum generation and capturing single-shot spectra. (b) Example of a single-shot supercontinuum spectrum. Adapted from Paper I.

3.3.2 Setup for capturing pulse-to-pulse spectra

The supercontinuum spectrum was recorded using a spectrograph with an ICCD camera mounted on the exit aperture. This allowed for the measurement of complete single-shot SC spectra, making it possible to analyze the dynamics of nonlinear propagation and noise effects that are not apparent in averaged measurements. The spectra that were measured in this way showed significant wavelength-dependent fluctuations. Since these fluctuations originate from the amplification of input noise, the pump pulses were measured and analyzed as well. Specifically, the temporal profile of the pump pulses was monitored using a fast silicon photodiode connected to a two-gigahertz oscilloscope. The pulse envelopes showed a varying but strong modulation originating from the beating of multiple longitudinal modes inside the cavity of the pump laser. This type of noise has previously been shown to affect the growth of Stokes orders [86]. Other sources of noise, such as the variations in coupling efficiency, were also considered and found to constitute a negligible source of additional noise. The pulse peak power distribution was observed to be close to Gaussian with a relative standard deviation of approximately 23 % of the mean value.

3.3.3 Statistical analysis of extreme spectral fluctuations

Two sets of 9000 single-shot SC spectra were recorded, corresponding to average coupled pulse energies of 1.0 μJ and 0.2 μJ. While extreme spectral fluctuations were observed in both sets, here we focus on the results obtained using the higher input energy. The fluctuations are demonstrated in Figure 7 (a), which superimposes 500 spectra together with the mean spectrum that was calculated for the entire set of 9000. To further highlight these differences, Figures 7 (b-d) show three individual spectra corresponding to narrow, intermediate and large spectral bandwidth, respectively. A discrepancy as large as six Stokes orders can be seen between these cases.

Histograms of spectral intensities were calculated at wavelengths highlighted by the arrows in Fig. 3.2. These histograms, which are presented in **Paper I**, showed a rapid transformation from a close-to-Gaussian distribution near the pump wavelength into an L-shaped distribution near the red end of the spectrum. This type of evolution has been previously associated with optical rogue waves [80], and constitutes a demonstration of extreme value events associated with nonlinear pulse propagation.

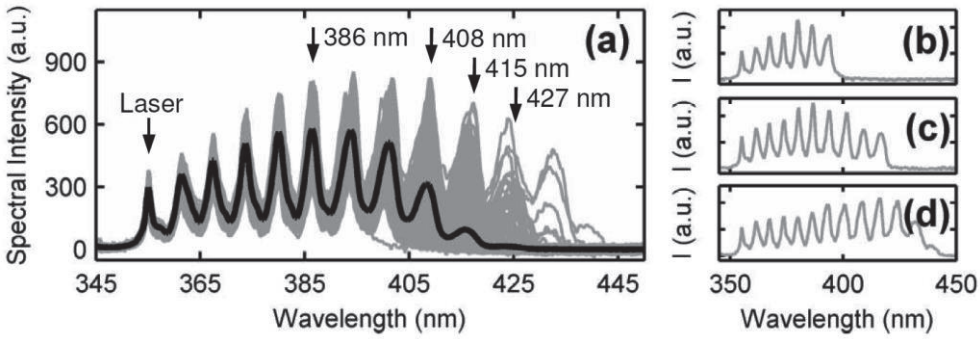

Figure 7. (a) Five hundred superimposed single-shot spectra (gray lines) together with the mean spectrum calculated over 9000 spectra (black line). (b–d) Examples of individual SC spectra highlighting significant shot-to-shot variations. Adapted from Paper I

To further characterize the extremity of spectral fluctuations across the full supercontinuum spectrum, a "Pareto-like" metric $M(\lambda)$ was used. This metric was introduced in Ref. [82] to characterize the skewness of a distribution. It is defined as the contribution of 20 % of the largest measured intensities to the total sum of all measured intensities at a given wavelength. The lowest possible value for M is 0.2, indicating a uniform distribution, whereas $M = 0.44$ corresponds to a Gaussian distribution, and values exceeding 0.5 indicate an L-shaped extreme value distribution. Figure 3.3 shows the mean spectrum together with the calculated $M(\lambda)$ for the two ensembles of 9000 spectra recorded using (a) low and (b) high input energy pulses, respectively. The appearance of L-shaped extreme value statistics can be clearly seen to correlate with a sudden increase in the Pareto-metric. This shift happens at around 410 nm for the high-energy case, corresponding to the 9th Stokes order. It is also present in the low energy regime of SRS, where the statistics start to exhibit extreme value behavior after around 380 nm, corresponding to the 5th Stokes order and above. These findings are in agreement with the numerical predictions of Ref. [87] calculated for similar pump noise conditions. The spectral regions exhibiting Gaussian and L-shaped fluctuations are called the saturated and unsaturated regimes of cascaded SRS, respectively.

To clarify the origin of these fluctuations, we ran numerical simulations of nonlinear pulse propagation for 1000 pulses whose peak power was normally distributed with a relative standard deviation of 23 %, corresponding to the experimental distribution. A simplified numerical model was used, which only contained spontaneous and stimulated Raman scattering as well as fiber losses. The

"Pareto-like" metric $M(\lambda)$ was then calculated for the simulated set of 1000 spectra. The results are shown in Fig. 8 (c). Although the numerical model was greatly simplified, it reproduced the experimental results well – the mean spectrum contains the same amount of Stokes orders and the metric $M(\lambda)$ increases sharply near the unsaturated regime. These results suggest that cascaded SRS can indeed transfer relatively small temporal fluctuations on the input pulse envelope into massive spectral fluctuations at the output.

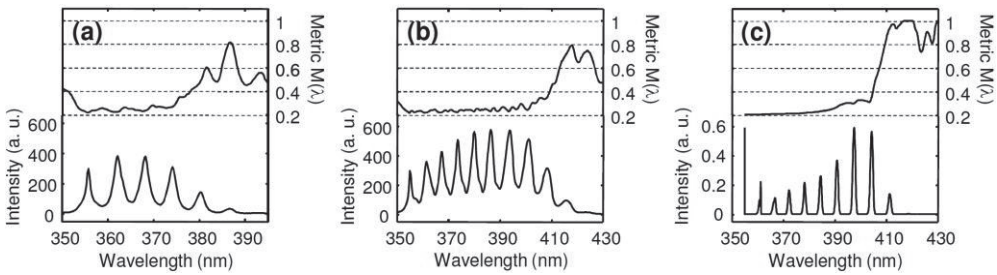

Figure 8. Mean spectrum (left axis) together with the Pareto metric $M(\lambda)$ (right axis) for (a) low input energy measurement and (b) high energy measurement. (c) Simulated results. Adapted from Paper I.

3.3.4 Correlation map analysis of cascaded Raman continuum

In addition to analyzing the skewness of the distribution, we made full use of the ability to measure shot-to-shot spectra and performed a correlation map analysis of Raman supercontinuum generation. This analysis, which was not published in **Paper I**, was motivated by the work presented in Refs. [88, 89], where correlation maps were used to study the noise transfer and energy exchange dynamics in SC generation through modulation instability. Here, we have applied the same analysis to SC generation through stimulated Raman scattering.

The intensity correlation map plots the spectral correlation between two wavelengths, and can be calculated using Eq. (1) in Ref. [89]. The spectral correlation varies between plus one and minus one, where a positive value indicates that intensities at two wavelengths increase or decrease together. A negative correlation indicates anti-correlation – when intensity increases at one wavelength, it decreases at the other. Figure 9 shows the correlation maps calculated for the sets of experimental and simulated spectra. The agreement between the two maps is fair; the main discrepancy is the lack of the checkerboard pattern in the simulated map. This is due to the fact that in order to have consistency with

Paper I, the simulated input pulses were temporally smooth with varying peak power. When the accurate intra-pulse modulation was included, the checkerboard pattern appeared.

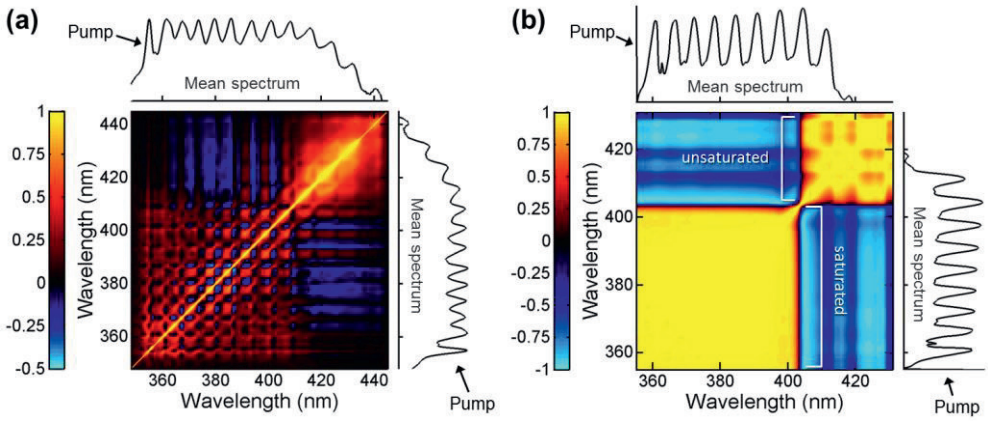

Figure 9. Intensity correlation maps calculated for the (a) experimental, and (b) simulated spectra. The color scale ranges from yellow (positive correlation) to cyan (anti-correlation) with black in the middle (no correlation). Two distinct regimes can be seen, corresponding to the saturated and unsaturated regimes of cascaded SRS. To aid in interpretation, the mean spectrum is shown on a logarithmic scale.

Both of the correlation maps show an interesting feature: light at the unsaturated region of the spectrum is anti-correlated with light at the saturated region. This indicates that there is a special set of very broadband spectra that exhibit more efficient energy transfer towards the long wavelength side at the expense of less light remaining closer to the pump. Once the unsaturated region is reached, it becomes probable that the spectrum extends even further, as indicated by the positive correlation within this region. These types of unique noise properties of long-pulse supercontinuum sources affect the performance of all of the spectroscopy techniques presented in this thesis.

4 INCOHERENT BROADBAND CAVITY-ENHANCED ABSORPTION SPECTROSCOPY

Incoherent broadband cavity-enhanced absorption spectroscopy (IBB-CEAS) is a technique for measuring molecular concentrations in gaseous or liquid samples. Compared to other optical techniques, IBB-CEAS provides an unusual combination of sensitivity and bandwidth. That is, very small concentrations of many different molecules can be measured simultaneously. This chapter begins with a brief overview of cavity enhanced spectroscopy methods in general, after which we focus on IBB-CEAS. We then go through the theory required for modeling and analyzing experimentally acquired IBB-CEAS spectra. Finally, we discuss the supercontinuum light sources, spectrometer setups, and experimental results for the near- and mid-infrared spectrometers first published in **Papers II & III**.

4.1 Cavity enhancement of absorption

The concept of using a high finesse cavity to enhance absorption dates back to the 1980's, to the development of cavity ring-down spectroscopy (CRDS) [90]. In this technique, optical pulses are coupled into a cavity, where they bounce back and forth, while experiencing an exponential decay of intensity caused by cavity losses such as gas absorption and mirror transmission. This exponential decay, i.e. the ring-down, is measured using a photodetector placed behind one of the mirrors. The decay rate is compared in the presence and absence of an absorber, which allows the concentration to be calculated. Since the invention of CRDS, many narrow- as well as broadband cavity-based methods have been developed. What all of these techniques have in common, and where their sensitivity originates from, is the long absorption path length in the cavity. Whereas other common direct absorption techniques, such as tunable diode laser absorption spectroscopy (TDLAS) can utilize multi-pass cells to bring the absorption path length to a

maximum of couple of hundred meters, cavity-enhanced methods can routinely achieve path lengths of tens of kilometers.

Cavity enhanced techniques can be divided into narrow- and broad-bandwidth methods. Narrow-bandwidth methods such as pulsed and continuous-wave CRDS [91-93], on- and off-axis ICOS [94], OF-CEAS [95], and NICE-OHMS [96] can achieve sensitivities more than three orders of magnitude higher compared to absorption spectroscopy methods where no cavity is used. This has opened new fields of applications for optical spectroscopy, with CRDS and ICOS now being used in techniques such as biomedical breath analysis [97-100] and atmospheric monitoring [101-108], where very high single-species sensitivity is required. While most of the cavity-enhanced spectroscopy has been done in the visible and near-IR parts of the spectrum, the research has recently extended to mid-IR spectral region, and parts-per-trillion single-species sensitivities have been reported using narrowband OF-CEAS [95, 109-111] and NICE-OHMS [112] techniques.

Broadband systems do not generally achieve the same sensitivity as the most advanced single-frequency methods. However, the point in broadband methods is to obtain sufficient sensitivity across a wide spectrum to enable selective multi-component measurement. This makes it possible for the same instrument to serve various diagnostic purposes, or to provide better understanding of complex dynamic processes by tracking multiple chemical species in real time [113]. It is also one of the only ways to selectively measure mixtures of very large molecules, whose absorption spectra lack distinct peaks. In addition to being robust against the effect of interfering absorbers, broad bandwidth also makes it easier to resolve absorption from scattering effects or system drifts. Broadband CRDS [114-116], phase-shift CRDS [117], IBB-CEAS [118, 119], and cavity-enhanced frequency comb spectroscopy [120] have achieved ppm-to-ppb level sensitivities, with varying degrees of experimental complexity. In the case of broadband CRDS, the complexity originates from the fact that a scheme for recording wavelength-dependent ring-down times is required. This can be achieved with a fast-rotating mirror in conjugation with a diffraction grating [121] or a two-dimensional clocked CCD array at the exit port of a spectrograph [114]. The main benefit of the frequency-comb techniques is that the light source can be coupled very efficiently to the cavity, allowing very high transmission to be recorded on the other side [122, 123]. However, they require complex mode-matching schemes, especially over a wider bandwidth. Dual-comb techniques enable a high-resolution absorption spectrum to be measured at high speed without diffractive elements using two coherent frequency combs [120].

Out of all the different broadband cavity enhanced absorption techniques, IBB-CEAS is arguably the simplest. The main components are an incoherent broadband light source, a cavity and a spectrometer. The spectrometer can be a scanning monochromator, while array detectors and FTIR spectrometers allow for faster acquisition. The main drawback of IBB-CEAS is the low transmittance of the cavity owing to the incoherent nature of the light source. This limits the signal-to-noise ratio and sets an upper limit to the reflectivity of the mirrors that can be used. However, compared to CRDS or frequency comb methods, where the light is only momentarily coupled to the cavity, IBB-CEAS has a higher duty cycle, which partially compensates for this drawback. IBB-CEAS was first demonstrated using an Xe-arc light source [118], but lamp, LED and SLED light sources are more typically used [124]. Because of the low transmission, the benefits of using a high brightness source with good beam quality become pronounced, and indeed supercontinuum sources have recently been demonstrated for IBB-CEAS [125-128]. Yet, the bandwidth of the sources has been filtered significantly to match that of the mirrors' spectral reflectivity, resulting in total intensity of only a few milliwatts.

In our work, we have attempted to demonstrate the full potential of IBB-CEAS technique first in near-IR region by using a fiber-based supercontinuum source whose spectrum is tailored to match the high reflectivity bandwidth of the cavity mirrors. Compared to previous studies, the source has two orders of magnitude higher spectral brightness at the measurement bandwidth. The full results are presented in **Paper II**. Furthermore, in **Paper III** we have demonstrated, for the first time, multi-component measurement using IBB-CEAS in the mid-IR wavelength region with the broadest reported IBB-CEAS bandwidth. Both of these projects make use of an advanced spectral fitting method based on differential optical absorption spectroscopy, which was first published in **Paper II**. The method is able to account for the combined effect of absorption line saturation and limited spectral resolution of the detection, increasing the dynamic range of the instrument and making it better suited for real-world applications.

4.2 Theory and analytical tools

While the basic concept of IBB-CEAS is as simple as increasing the absorption path length of a direct broadband absorption measurement by using a cavity, the theory of IBB-CEAS is more complex than simply using the cavity's effective path

length to calculate absorption. This is because the absorption itself affects the photon lifetime and therefore the effective path length in the cavity. In addition, the analysis of broadband data can be done in many ways, some of which are more advanced than others. The ultimate goal is to be able to retrieve trace gas concentrations of many species simultaneously, with high sensitivity and selectivity, in the presence of interfering absorbers, system drifts, Rayleigh scattering, Mie scattering, and so forth. Arguably, the most advanced way of doing this is differential optical absorption spectroscopy (DOAS), originally developed for long-range atmospheric measurements [29]. In DOAS, a modeled differential absorption spectrum is fitted to the experimental spectrum using a least-squares method. The concentrations are then retrieved as the fitting parameters. The important benefit of the DOAS method is to be able to separate the absorption of molecules, which typically varies rapidly as a function of wavelength, from smoothly varying background effects, such as Rayleigh scattering and system drifts. This is achieved by high pass filtering of the spectrum, or more commonly by including a low order polynomial in the fit. In **Paper II**, we have published and shortly discussed a DOAS-based method for analyzing broadband cavity-enhanced spectra. Here, we present the method in more detail.

In order to use a DOAS based fitting method in IBB-CEAS, a model is required for cavity enhancement of broadband spectra. The theory of cavity enhancement for incoherent sources was first given in the original paper by Fiedler et al. [118], where the treatment is done in time domain. Later on, Triki et al. have arrived at the same results using a frequency domain approach [124]. These are the primary results that have been used in the retrieval of concentrations from measured IBB-CEAS spectra in various studies [31, 125, 127-134]. They can be used to model the wavelength-dependent cavity-enhanced absorption coefficient for a given trace gas concentration assuming that the mirror reflectance curve and the spectral absorption cross section of the molecule are known. However, since the results are given for the absorption coefficient, and not the transmittance, which is what is actually measured by the spectrometer, implementation of spectrometer resolution is not straight-forward. The primary way of accounting for the instrument resolution has been to convolve the molecular absorption cross section with the instrument slit function. This can lead to distortions in the modeled spectrum, since the sharp physical absorption features are made artificially wider, and the real effect of the saturation of strong absorption peaks in the cavity is not properly accounted for. This neglect was first noted in Ref. [125]. In a low-resolution case, the modeled spectrum becomes distorted as soon as the single-pass

absorption losses become comparable to the mirror losses. The saturation arises from the fact that the effective path length in the cavity depends not only on the mirrors but also on the wavelength dependent absorption losses. This dependence was first explicitly pointed out by Platt et al. [135], with the motivation of using established DOAS methodology and software in the analysis of IBB-CEAS spectra. However, their method is not straight-forward to implement in a limited-resolution measurement, such as what was the case here.

The full derivation of the DOAS-based spectral fitting model of **Paper II** is given below. The treatment starts from the intermediate results given in Ref. [135], which are used to model the cavity-enhanced differential transmittance spectrum. Let us consider an optically stable cavity that consists of two mirrors with reflectance R. We assume that the pulses are incoherent so that the total intensity can be obtained as a linear superposition of the pulse intensities in the cavity. In addition, we assume that the spectral resolution of the detection is worse than the free spectral range of the cavity so that it is sufficient to look at the average spectral transmittance over many longitudinal cavity modes. Initially, only the fraction $\varrho = 1 - R$ of the radiation emitted by the light source enters the resonator (assuming lossless mirrors). Equation (11) in Ref. [135] describes the decay of the intensity of a light pulse I_{in} inside the cavity as it bounces back and forth between the mirrors. The decay can be derived from the change in one transverse of the resonator:

$$-\frac{dI_{in}(n)}{dn} = I_{in}(n)(1-T_{gas}R), \tag{3}$$

where T_{gas} is the single-pass transmittance of the gas within the cavity, R is the reflectance of the mirrors, and n is the number of passes through the cavity. To simplify the treatment, the wavelength dependence of the variables is omitted for now. Note that the number of passes n is used as a continuous variable, although in reality it can only assume discrete values. By integrating with the boundary condition $I_{in}(n = 0) = I_{in}(0)$, we get:

$$I_{in}(n) = I_{in}(0)e^{-(1-T_{gas}R)n}. \tag{4}$$

Re-writing $T_{gas} = 1 - \tau$ and $R = 1 - \varrho$, with $\tau, \varrho \ll 1$ for small single-pass absorption and mirror losses, we obtain:

$$T_{gas}R = (1-\tau)(1-\rho) = 1-\tau-\rho+\tau\rho \approx 1-\tau-\rho. \tag{5}$$

Equation (4) can now be written as:

$$I_{in}(n) = I_{in}(0)\,\mathrm{e}^{-(\tau+\rho)n}, \tag{6}$$

where $I_{in}(n)$ is the intensity inside the cavity after n reflections or passes through the cavity. Outside of the cavity, behind the output mirror, the intensity is smaller by a multiplier of ρ / 2 = (1 R) / 2, where the denominator two comes from the fact that the light is leaking out through both of the mirrors. The cavity-enhanced differential transmittance can then be calculated from total intensities measured with and without the absorbing gas species present:

$$\frac{I}{I_0} = \frac{\int_0^\infty \frac{\rho}{2} I_{in}(n)dn}{\int_0^\infty \frac{\rho}{2} I_{in0}(n)dn} = \frac{\int_0^\infty \frac{\rho}{2} I_{in}(0)e^{-(\tau+\rho)n}dn}{\int_0^\infty \frac{\rho}{2} I_{in}(0)e^{-(\rho)n}dn} = \frac{\int_0^\infty e^{-(\tau+\rho)n}dn}{\int_0^\infty e^{-(\rho)n}dn}, \tag{7}$$

where I_0 is the intensity with no absorbing species present, so that $\tau = 0$ (cavity flushed with nitrogen or dry air). Evaluating the integral yields:

$$\frac{I}{I_0} = \frac{\rho}{\rho+\tau}, \tag{8}$$

which is now the integrated cavity-enhanced differential transmittance. Here the number of passes n was treated as a continuous variable although in reality it can only assume discrete values. A discrete treatment is given in [118] and it leads to the same result. We now include the wavelength-dependence of the variables in the equation. The term $\rho(\lambda)$ represents the wavelength-dependent mirror losses, or the mirror transmittance curve, assuming high-quality mirrors, and it can be obtained using a calibration measurement. The small wavelength-dependent single-pass absorption losses $\tau(\lambda)$ can be calculated from the linear approximation of the Beer-Lambert law (2), where the transmittance of the sample gas can be written as $T(\lambda) = 1 - \tau(\lambda)$, and

$$\tau(\lambda) = \sum\nolimits_j \sigma(\lambda)_j N_j d_0, \tag{9}$$

where $\sigma(\lambda)_j$ are the absorption cross-sections of the gas species, N_j their number densities and d_0 is the cavity length. The cavity enhanced differential transmittance can now be written as:

$$\frac{I(\lambda)}{I_0(\lambda)} = \frac{\rho(\lambda)}{\rho(\lambda) + \sum_j \sigma(\lambda)_j N_j d_0}. \tag{10}$$

The instrument resolution directly affects how this transmittance spectrum is measured. We implemented this in the model by convolving the transmittance with an instrument slit function $g(\lambda)$. Finally, we apply the DOAS-principle by first calculating the optical density, which is given as the inverse natural logarithm of the transmittance. We then add a low degree polynomial to the modeled spectrum to account for background effects such as smoothly varying absorbers, scattering, and system drifts. The final equation for the modeled optical density is then given as:

$$D_{fit}(\lambda) = -\ln\left(\frac{\rho(\lambda)}{\rho(\lambda) + \sum_j \sigma(\lambda)_j N_j d_0} * g(\lambda) \right) + \sum_k a_k \lambda^k, \tag{11}$$

where the number densities Nj and polynomial coefficients a_k are used as fitting parameters. Typically a third-degree polynomial is sufficient, but higher degrees can also be used as long as the polynomial varies smoothly compared to the absorption features. The absorption cross-sections $\sigma(\lambda)_j$ can be modeled beforehand using a spectral database, such as HITRAN 2012 [15], and well-known line-broadening mechanisms. In order to retrieve the molecular number densities N_j from measured data, Equation (11) is fitted to the measured optical density spectrum using a least squares fitting method such as the Levenberg-Marguardt algorithm. The fit also gives the polynomial coefficients a_k, which are typically not used, but can reveal information about e.g. the aerosol extinction coefficient.

Equation (11) can also be used in the calibration of the instrument, i.e. in determining the mirror losses $\varrho(\lambda)$. In this case, a measurement is made with a reference sample of known concentration. It is preferable to use a gas that has absorption features covering the whole measurement bandwidth. In the calibration fitting procedure, a function that contains the fitting parameters is used for $\varrho(\lambda)$, whereas the polynomial coefficients a_k can still be allowed to be fitted freely. One option is to use the mirror transmittance curve provided by the manufacturer as a starting point for $\varrho(\lambda)$ and add a small constant wavelength-independent fitting

parameter to represent additional losses such that $\varrho(\lambda) = \varrho(\lambda)_{\text{trans}} + \epsilon$. This correction parameter ϵ is then retrieved from the least squares fit. A more broadband calibration is also possible by replacing the constant ϵ with a curve $\epsilon(\lambda)$, for example a low degree polynomial, whose coefficients then act as the calibration parameters. Doing this increases the accuracy of the calibration over the full mirror bandwidth. It is worth noting that although the term $\varrho(\lambda)$ is referred to as mirror losses, it actually contains all additional losses, which are present in the measurements of $I(\lambda)$ and $I_0(\lambda)$. Most notable of these losses are Rayleigh scattering losses caused by scattering from the molecules of the carrier gas and diffraction losses caused by cavity misalignment.

4.3 Near-infrared supercontinuum light source

The objective of the work reported in **Paper II** was to attempt to demonstrate the full potential of supercontinuum sources in IBB-CEAS. In contrast to previous reports, where most of the optical power has been wasted, here the near-IR SC source was designed specifically for the application, so that the spectrum matches the reflectance curve of the cavity mirrors. The spectral brightness of the source is about two orders of magnitude higher compared to previous studies.

The supercontnuum is generated by injecting 700-ps pulses at 1.5 μm into the anomalous dispersion regime of a standard single-mode fiber. As discussed in Chapter 3, the mechanisms of spectral broadening in this long-pulse, anomalous dispersion regime are dominated by noise-seeded modulation instability and soliton dynamics [37]. The result is a broadband supercontinuum with more than 250 nm of total bandwidth, extending from 1500 nm to over 1750 nm with a total optical power of 800 mW. Figure 10 (a) shows the time-averaged supercontinuum spectrum for different values of input pulse peak power. The processes of modulation instability and soliton self-frequency shift are evident in the figure as the growing sidebands around the pump, and efficient spectral broadening towards longer wavelengths, respectively. Higher peak powers were attempted, but ultimately disregarded as they caused the bump in the middle of the spectrum to shift even further to the red, while also increasing the risk of optical damage to the fiber interface. In order to demonstrate the benefits of using such a source, the SC was compared against an SLD source, which was also chosen to best match the IBB-CEAS setup. Figure 10 (b) shows a comparison between the SC and SLD spectra, together with the mirror reflectance curve.

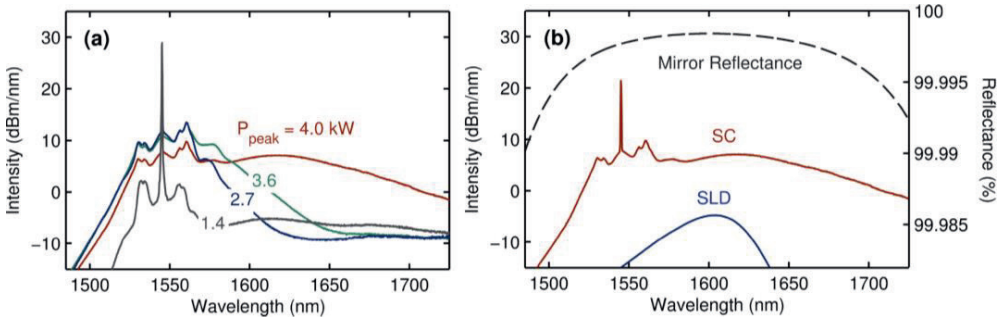

Figure 10. (a) Supercontinuum spectrum for different input pulse powers. (b) Comparison of supercontinuum (SC) and superluminescent diode (SLD) spectra together with the mirror reflectance curve. The reflectance is calculated from the transmittance curve measured by the manufacturer assuming zero losses

As explained in Chapter 2, any supercontinuum generated in the long-pulse regime will show extreme pulse-to-pulse fluctuations. However, the average spectrum can remain sufficiently stable when using a high repetition rate laser and long integration times. Besides pulse-to-pulse fluctuations, another major source of detection noise can arise from the residual light at the pump wavelength, which is seen as the sharp peak in Fig. 10 (a). This is an intrinsic feature of any supercontinuum generated in the long pulse regime. In time domain, the peak at the laser wavelength corresponds mostly to the leading and trailing edges of the pulse, where the intensity is not high enough to undergo nonlinear spectral broadening. If this coherent laser peak is not filtered out, optical feedback can cause the pump laser to momentarily lock to the IBB-CEAS cavity modes, resulting in massive stray light noise at the detector. This locking behavior was observed in the measurements carried out for **Paper II**, and subsequently suppressed by slightly misaligning the cavity as well as mechanically vibrating one of the cavity mirrors. It should be noted that a better way to suppress the feedback would be to use a narrowband notch filter in combination with an optical isolator.

4.4 Near-infrared spectrometer setup and calibration

Figure 11 shows the full near-infrared spectrometer setup. The IBB-CEAS setup is very simple in design, which is a major benefit for application considerations. The near-confocal cavity consists of two mirrors, each having a reflectance exceeding 99.99 % between 1520 nm and 1670 nm. Such high reflectance results in effective path lengths of over 10 km, but this also results in the average transmission of the

cavity for an incoherent source being lower than 0.5×10^{-4} [124]. The transmission is especially low at the center of the mirror bandwidth where the reflectance is higher than 99.998 %. However, this is also where the SC spectrum has roughly the highest intensity, allowing for a significant increase in signal-to-noise ratio of detection compared to lower brightness sources.

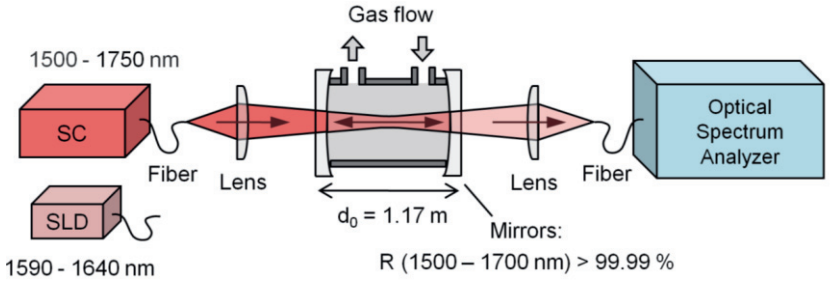

Figure 11. Experimental setup for near-IR IBB-CEAS. Light from either the supercontinuum (SC) or the superluminescent diode (SLD) source is collimated and focused into a cavity containing the gas sample. Light leaking through the output mirror is focused into a multi-mode fiber, which is connected to an optical spectrum analyzer. Adapted from Paper II.

The instrument calibration was performed by measuring the mirror losses $\varrho(\lambda)$ with the help of a reference sample. Specifically, an optical density spectrum was measured using a sample of 100 ppm CO_2, after which a small wavelength-independent loss parameter ϵ was added to the manufacturer-specified mirror transmission and retrieved using a fitting process described in Chapter 4.2. Mirror loss parameters of 12.1×10^{-6} and 8.8×10^{-6} were retrieved for the SC and SLD sources, respectively. The discrepancy is attributed to the intentional misalignment of the cavity in the SC measurements, which was done in order to suppress the mode-locking effects. The total mirror losses at the center of the mirror bandwidth correspond to effective path lengths of 40 km and 46 km for the SC and SLD source, respectively. The calibration using a reference sample is a simple and reliable method, but other authors have also demonstrated calibration using a more complex broadband phase-shift CRDS [136], or by using a ring-down measurement with a separate diode laser [131]. The latter was deemed unreliable, since the mirror losses found to be depend on the light source alignment, which can be noticed from these results as well.

4.5 Near-infrared spectrometer performance

The performance of the IBB-CEAS instrument using SC and SLD light sources was evaluated by measuring varying concentrations of carbon dioxide. Figure 12 shows the weak $3\nu_1 + \nu_3$ combination overtone absorption band of CO_2 measured from a 200 ppm sample using (a) the SLD source, (b) the SC source, as well as (c) the result of the least squares fit to (b) using Eq. (11). The superior brightness of the SC source can be seen to result in a much less noisy spectrum compared to the SLD. The modeled spectrum is in excellent agreement with the measured spectrum, which was also the case for the SLD measurement (modeled spectrum not shown here), including a compensation for the baseline drift made possible by the extra polynomial in Eq. (11). Concentrations of 196 ppm and 194 ppm were retrieved from the fits. Lower signal-to-noise ratio measurements were also carried out for a concentration of 40 ppm with similar results, as described in **Paper II**.

The detection limit for CO_2 was determined for both sources by repeatedly measuring CO_2 concentration from a nitrogen-flushed cavity where no CO_2 was present. The CO_2 absorption spectrum was nevertheless fitted to the measured spectra. Histograms of retrieved concentrations showed Gaussian distributions around zero concentration with standard deviations of 0.41 ppm for the SC source and 1.12 ppm for the SLD source. From these values, 3σ detection limits for CO_2 were defined as 1.2 ppm and 3.4 ppm for the SC and SLD source, respectively, with a scanning time of 2.5 minutes. The difference is smaller than expected, which is most likely a result of the slightly misaligned cavity as well as higher relative amplitude noise in the case of the supercontinuum. However, the supercontinuum offers much broader usable bandwidth, the benefit of which was demonstrated by measuring the 80-nm-wide absorption spectrum of methane, which could not be done using the SLD source. This broadband experimental spectrum is shown in Figure 13.

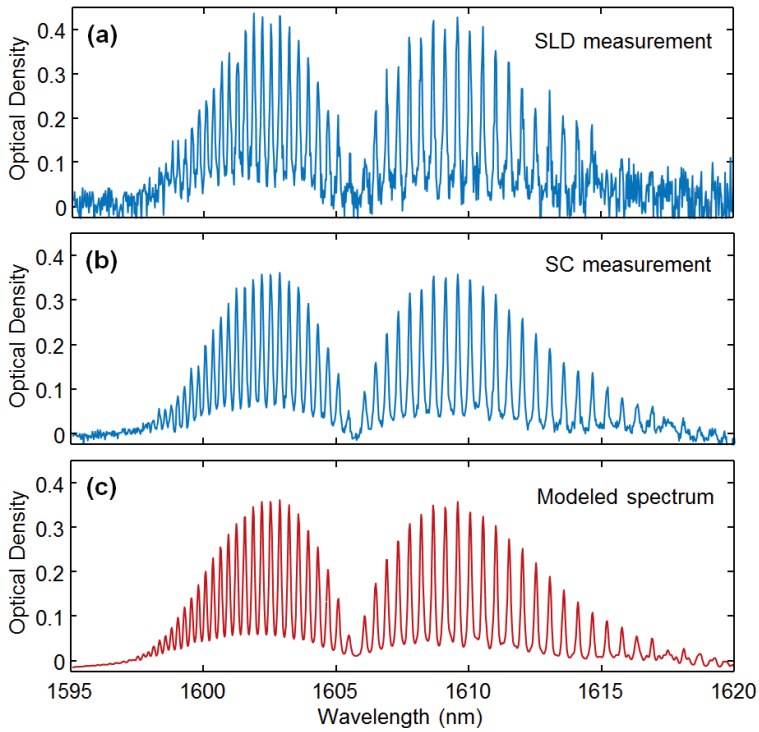

Figure 12. Experimental CO2 absorption spectrum measured from a concentration of 200 ppm using (a) the SLD source and (b) the SC source, together with (c) the modeled spectrum that is fitted to the experimental SC spectrum in (b). A concentration of 194 ppm was retrieved from the fit.

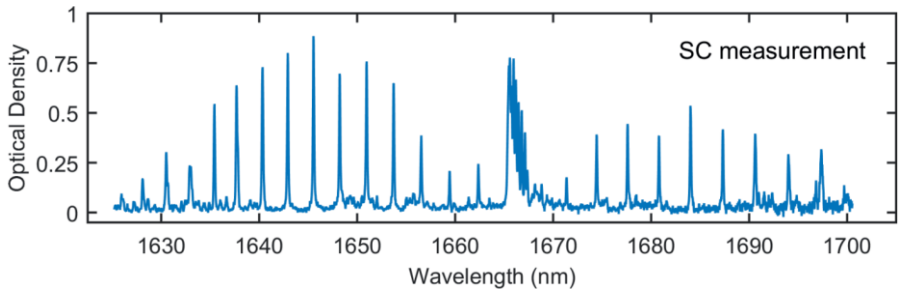

Figure 13. Broadband absorption spectrum of CH4 measured from a concentration of 4 ppm using the near-IR supercontinuum source.

4.6 Mid-infrared supercontinuum light source

The main motivation for developing an IBB-CEAS spectrometer operating in the mid-infrared spectral region is the abundance of strong rovibrational absorption bands in this region. The wavelength region from 3000 nm to 5000 nm is especially interesting, since it contains very few absorption lines of the water molecule that can interfere with the measurement (see Figure 4), while at the same time containing abundant rovibrational bands associated with fundamental excitations of common group vibrations, e.g. stretches of C-H, O-H, and N-H bonds, which allow a vast number of molecules to be detected.

The mid-infrared supercontinuum source of **Paper III** employs the same pump laser (Keopsys Kult) as the near-infrared source. The 700-ps pulses with 10 kW peak power at 1547 nm are first injected into the anomalous-dispersion regime of a four-meter single-mode dispersion-shifted fiber (DSF). The initial spectral broadening is dominated by noise-seeded modulation instability, which leads to soliton formation and soliton self-frequency shift. These dynamics expand the spectrum towards longer wavelengths up to the limit of the transparency window of silica at 2400 nm. The red-shifted solitons are then injected into a 7-m step-index fluoride (ZBLAN) fiber, which is transparent up to 4000 nm, and has anomalous dispersion for wavelengths above 1620 nm. The solitons undergo additional Raman self-frequency shift in the ZBLAN fiber, extending the spectrum to 3700 nm. The supercontinuum source has an average output power of 160 mW, limited by coupling and absorption losses. The average spectrum, which is shown in Figure 14, is smooth and stable, but underneath the source most probably exhibits large pulse-to-pulse spectral fluctuations typical for a long-pulse supercontinuum.

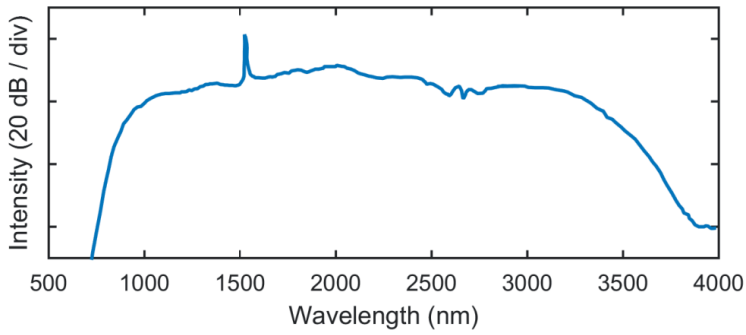

Figure 14. Mid-infrared supercontinuum spectrum generated in a four-meter dispersion-shifted silica fiber that is coupled to a seven-meter ZBLAN fiber.

4.7 Mid-infrared spectrometer setup and calibration

The mid-infrared IBB-CEAS spectrometer setup is illustrated in Figure 15. The setup is very similar to the near-infrared spectrometer, with the main exception of a more complex detection scheme pictured on the right side of the cavity. The all-in-one optical spectrum analyzer is replaced by a half-a-meter monochromator with an external liquid-nitrogen-cooled InAs photodetector at the output. Additionally, a lock-in amplifier is used together with an optical chopper to enhance the signal-to-noise ratio. Compared to the near-IR setup, the fiber-to-fiber coupling is also more challenging and lossy here between silica and fluoride fibers, as is fiber-to-air collimation when using a speciality soft glass fiber with no connectors. These changes highlight some of the difficulties faced when measuring in the mid-IR region.

The cavity mirrors have a nominal reflectance of R > 99.95 between 3000 nm and 3450 nm. Compared to the near-IR setup, less reflective (more transmissive) mirrors are used to compensate for the lower spectral brightness of the source and the less sensitive detection scheme. Indeed, the filtered part of the SC spectrum that is coupled into the cavity has an optical power of 4 mW, which is significantly lower than the 800 mW that was used in the near-IR setup. However, the measurement bandwidth is much broader. Calibration of the instrument was performed using a reference sample of known concentration (Chapter 4.2 methodology), and it yielded a mirror loss curve corresponding to a reflectance of R > 99.7 over the 450-nm measurement bandwidth, resulting in an effective path length of around 300 meters.

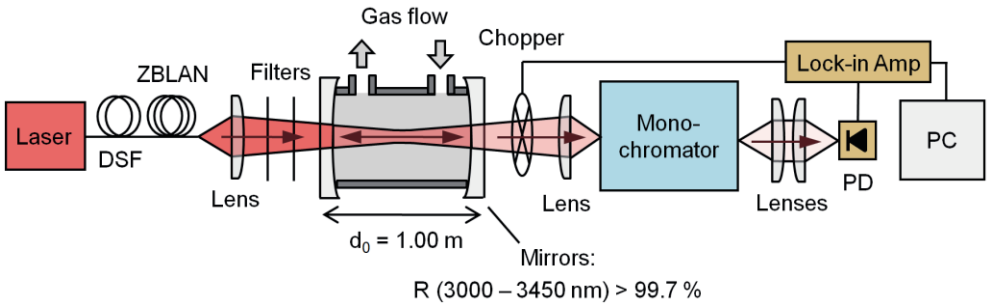

Figure 15. Experimental setup of the mid-IR IBB-CEAS spectrometer. See Paper III for technical details.

4.8 Mid-infrared spectrometer performance

The response of the mid-infrared IBB-CEAS spectrometer was evaluated by measuring varying concentrations of acetylene and methane, and applying the DOAS-based spectral fitting method to the data. The resulting spectra are presented in **Paper III**, showing a good match between measured and modeled curves. The detection also showed a linear response to varying concentrations between 0.25 ppm and 10 ppm for both gases. While no measurements were made at the noise floor, the smallest measured concentrations were 0.5 ppm and 0.25 ppm for acetylene and methane, respectively. These values indicate the upper bounds for the detection limits. Although the broadband fitting response was still linear, the spectrum was no longer visibly distinguishable from the noise, suggesting that the actual detection limits are close to these values.

After measuring the response for individual gases, both acetylene and methane were flown through the cavity and measured simultaneously. This was done in order to demonstrate the capability for exceptionally broadband measurement afforded by the supercontinuum light source. Figure 16 shows the experimental spectrum that is measured over the full 450-nm range of the mirrors' high-reflectance bandwidth, together with the modeled spectrum that is fitted to the data. To the best of our knowledge, this is the broadest IBB-CEAS spectrum ever reported. The measured and modeled spectra are in very good agreement, and the retrieved concentrations match the ones set by the nominal flow rates of the two gases very closely. We note that although dry N_2 was used as both the carrier and the reference gas, using room air is also feasible since the bandwidth is free from interfering absorption by H_2O or CO_2 – see Figure 4 for reference.

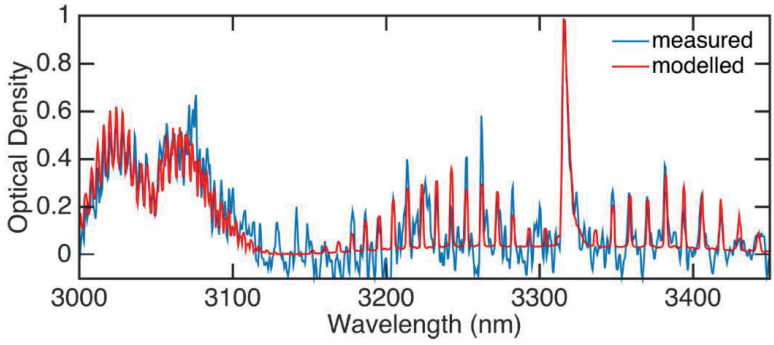

Figure 16. Broadband multi-component measurement of acetylene (3000 nm – 3100 nm) and methane (3150 nm – 3450 nm) together with the least-squares-fitted modeled spectrum. Adapted from Paper III.

4.9 Comparison of the techniques

In order to compare the sensitivity of the techniques, the detection limits for individual gases were generalized by calculating corresponding minimum detectable absorption coefficients (*MDA*s). The *MDA* is calculated based on the detection limit by assuming it was obtained via a hypothetical single-wavelength using the strongest line of the spectrum within the measurement bandwidth. In other words, $MDA = a_{min} = \sigma_{max} N_{min}$, where σ_{max} is the highest value for the absorption cross section in the computer-modeled Voigt-broadened absorption band, and N_{min} is the molecular number density corresponding to the achieved detection limit. Although *MDA* does not take into account the shape of the absorption spectrum, it is an acceptable metric for the overall sensitivity of the technique, especially when given together with light source parameters and measurement time. The minimum detectable absorption coefficient can then be used to calculate hypothetical detection limits for gases with known absorption cross sections within the measurement bandwidth, as long as the overall spectrum has a similar line structure. Table 1 shows the comparison of the different techniques presented in this chapter in terms of optical parameters and achieved *MDA* values. For the near-IR techniques, *MDA* was calculated based on the achieved carbon dioxide detection limits and the modeled CO_2 absorption cross-section, while the mid-IR *MDA* calculation is based on those of methane.

Table 1. Optical parameters and detection sensitivities of the IBB-CEAS spectrometers built in this work using different light sources.

	Near-IR SLD	Near-IR SC	Mid-IR SC
Center wavelength	1600 nm	1600 nm	2200 nm
-10dB bandwidth	90 nm	230 nm[a]	2300 nm[a]
Optical power	17 mW	800 mW	160 mW
Power at mirror bandwidth	17 mW	800 mW	4 mW
Effective path length	46 km	40 km	0.3 km
Carbon dioxide detection limit	3.4 ppm	1.2 ppm	N.A.[b]
Methane detection limit	14 ppb[c]	4.9 ppb[c]	< 0.25 ppm
Acetylene detection limit	N.A.[b]	1.7 ppb[c]	< 0.5 ppm
Measurement time	150 s	150 s	600 s
Minimum detectable absorption coefficient	6.2×10^{-9} cm^{-1}	2.2×10^{-9} cm^{-1}	$< 1.3 \times 10^{-5}$ cm^{-1}

[a]Ignoring the laser peak. [b]No absorption bands available within the measurement bandwidth. [c]Calculated based on *MDA* and the strongest line in the measurement bandwidth.

Looking first at the near-IR results of **Paper II**, the achieved sensitivity is only slightly higher compared to previous IBB-CEAS studies performed using a supercontinuum source, such as Ref. [125] and Ref. [31]. This can be surprising at first, since a source with much higher spectral brightness was used in this work. However, these studies utilized more optimized detection schemes, namely an array detector and a Fourier-transform spectrometer, which are able to collect much more light. It can be anticipated that using a similar detection scheme would result in a much higher sensitivity. The sensitivity could be further increased by optimizing the cavity and coupling parameters according to guidelines given in [137] and by suppressing optical feedback through the use of an optical isolator or spectral filters. Even without these optimizations, the sensitivity is higher than most other broadband CRDS-methods [114], and it does not fall much behind from the most advanced single-wavelength methods, where the typical *MDA* is in the range of 10^{-11} cm^{-1} – 10^{-10} cm^{-1} [102-104, 138].

The mid-IR spectrometer of **Paper III** constituted the first report of IBB-CEAS using a mid-infrared supercontinuum source. Furthermore, to the best of our knowledge, the bandwidth of the measurement was the broadest ever reported for this technique. However, as can be seen from Table 1, the sensitivity fell far behind the near-IR results. This is due to the combination of multiple effects that make the mid-IR measurement challenging. Most of the SC power is lost due to lossy fiber-to-fiber coupling, the remaining power is not well-distributed over the mirror bandwidth, the cavity coupling is inefficient, and the measurement utilizes the red end of the spectrum, which is the noisiest part of the SC, as discussed in Chapter 3 and **Paper I**. In addition, detectors are generally noisier in the mid-IR, resulting in poorer signal-to-noise ratios. However, the there are plenty of opportunities to increase the sensitivity. The cavity coupling could presumably be much better, as is evident from the large discrepancy between nominal and measured mirror losses. The mid-IR source could be optimized by fusion splicing the silica and ZBLAN fibers [139], resulting in more optical power and a broader spectrum, pushing the unstable red edge further away. On the detection side, FTIR or novel mid-IR array detectors [140] could be used, or if the resolution is not critical, even a Fabry-Perot interferometer [141] could be used to replace the bulky and lossy monochromator. Another interesting possibility is MIR-to-NIR upconversion together with silicon-based detectors [142]. The improvements do not have to be massive in order for the detection limits to be somewhat comparable to near-IR methods, since absorption cross-sections are typically two or more orders of magnitude stronger in the mid-IR.

5 SUPERCONTINUUM LIDAR

In this chapter, we discuss the supercontinuum lidar, which is being developed for remote 3D-profiling of gas temperature in large-scale combustion units. Compared to the laboratory-oriented techniques of previous chapters, this is an industrial application with very different optical requirements. With this in mind, we begin with a few general notes on the role of spectral resolution and remote measurement capabilities in the industrial context. We then present the measurement problem and discuss the various techniques that have been developed in an attempt to solve it. The rest of this chapter describes our supercontinuum lidar setup, the initial laboratory results, initial backscattering results at a large-scale combustion unit, and finally the future prospects of this technique.

5.1 Low-spectral-resolution and remote measurement

While high sensitivity and spectral resolution are key in laboratory applications, cost, size, and ease of use are typically the most important factors when industrial applications are considered. These factors naturally limit the spectral resolution, since in most broadband devices, such as dispersive spectrometers and FTIR devices, high resolution comes with large instrument size and cost, with larger instruments being more sensitive to optical alignment as well. Therefore, fixed filter arrays and filter wheels are often used. Where a moderate resolution is needed, compact grating spectrometers that contain an array detector are commonly utilized. Recently, there have been interesting developments in miniaturization of the classical monochromator [143, 144], the Fabry-Pérot interferometer (FPI) [145], and the FTIR spectrometer [146] by using MEMS technology. These devices aim for similar or better performance compared to the compact grating-array detectors, but with much smaller cost and size.

The interest in remote optical measurement has been growing consistently, with trends ranging from earth observation using microsatellites [147] to autonomous

driving [148] and facial recognition [149]. When it comes to beam steering, compact, robust, and mass-manufacturable micro-electro-mechanical systems (MEMS) are currently being developed for various consumer devices, some of the most notable ones being portable projectors, head-mounted displays, and automotive lidars. When MEMS technology matures, these components will most probably be employed for spectroscopy, as has been the case with telecom technology, which is now widely used in near-infrared spectroscopy.

In order to remotely measure material compositions, spectral data needs to be gathered. This is where high spectral resolution is especially difficult to achieve. In addition to the above concerns about the size, cost, and complexity, the amount of light that can be remotely captured is typically small, and passing it through a dispersive element would lower the signal-to-noise ratio even further. These concerns apply especially to active devices such as lidars, but are also true for passive devices such as hyperspectral cameras. Remote spectral measurement is nevertheless a very valuable family of techniques that has massive future potential. It is currently used in specialty applications in fields such as agriculture, mining, forestry, meteorology, climate science, military, and astronomy.

5.2 Optical combustion thermometry

The goal of the work presented in **Paper IV** is to develop a short-range, low-spectral-resolution supercontinuum lidar for real-time 3D-mapping of various gas parameters, such as temperature and concentration, in power plant combustion units (CU) using only one inspection window. This type of hard-to-get data could be used to manage, control, and optimize the combustion process in terms of efficiency and cleanliness, which is especially important in waste and biomass combustion, owing to the inhomogeneous nature of the fuel.

The instrument published in **Paper IV** is one of the first short-range supercontinuum lidars [150-153], and is a first attempt of bringing this technology to combustion monitoring, where the management currently mostly relies on basic thermocouples [154] for temperature information. The supercontinuum lidar is a unique contribution to the field of combustion thermometry, where it competes with other techniques such as ultrasound [155] and diode laser [156-160] grids, that have already seen implementation, and more advanced techniques such as picosecond lidar [161-163], atomic fluorescence [164], and CPFAAS [165] based thermometry techniques that are being researched.

5.3 Short-range supercontinuum lidar setup

In order for the lidar to remotely measure the temperature distribution with high spatial resolution, it needs to probe gas parameters that are temperature dependent using short enough pulses of light. One example of this is the picosecond lidar, presented in Refs. [161-163], which is based on Rayleigh thermometry, i.e. the measurement of temperature via the intensity of molecular scattering, which is density and therefore temperature dependent. Here, we use the temperature dependence of the water absorption spectrum, which we probe using a Differential Absorption Lidar (DIAL). The physical basis for this effect is that temperature affects the distribution of molecules in the higher excited ro-vibrational states, which alters the absorption spectrum especially at higher temperatures where higher vibrational states are being populated, and the so-called "hot bands" become active. The benefits of this approach are: 1) water is one of the main hydrocarbon combustion products, and therefore always present in high concentration, and 2) the signal comes from light that is backscattered by soot or ash particles, which is much stronger than light scattered by molecules. Where most other optical thermometry methods become unusable in the presence of soot or ash, this method can work as long as there is some visibility through the combustion unit.

To find suitable wavelength bandwidths, the temperature dependence of the H_2O absorption cross-section was modeled from one to five microns using the HITEMP [18] database, which includes the hot bands that are relevant at CU temperatures. After identifying the region around 1.4 μm to be a preferred candidate based on both the strength and the high temperature dependence of absorption, a nanosecond supercontinuum source with high spectral intensity over that region was developed. The benefit of using an SC source is that there is no need to accurately tune the laser to hit any line in the complex spectrum, especially since the line shapes are temperature and pressure dependent, and the environment is turbulent. Another significant advantage is the ability to gain a lot of spectral data over a broad bandwidth. The source, whose technical details and output spectrum can be found in **Paper IV**, is very similar to the ones described in Chapter 3. Principally, it uses a small, robust, and cost-effective nanosecond fiber-laser to pump a standard single-mode fiber, and the spectral broadening is caused mainly by stimulated Raman scattering. The full experimental setup is shown in Figure 17.

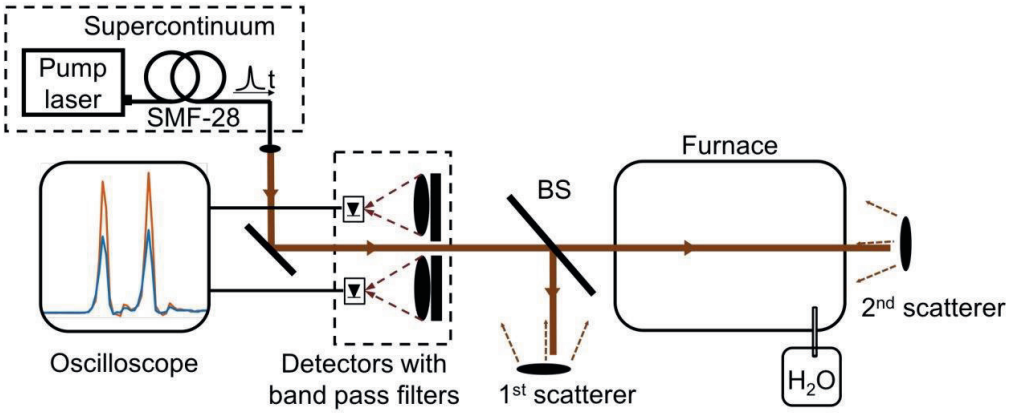

Figure 17. Experimental setup for supercontinuum lidar measurements. Adapted from Paper IV.

5.4 Laboratory measurements of furnace temperature

The initial experiments consisted of remotely determining the temperature in a furnace by measuring the wavelength-dependent absorption of water vapor at two wavelength bands using two filters, with signal collected from scatterers before and after the furnace. After this proof of concept, the work can proceed to repeating the measurements in a full-scale combustion unit, while also extending the measurement to cover other variables, such as concentrations of different molecular species, by including more wavelength bands.

The results of this initial measurement are presented in Figure 18, which shows the temperature-dependent transmittance through the one-meter furnace filled with 100 % H_2O vapor for the two wavelength channels (Ch1 and Ch2). The first channel shows no change in transmittance when the temperature increased, while the second channel clearly does. The results are in reasonable agreement with the modeled transmittances, with temperature measurement accuracy of around 50 °C in the 600 °C – 900 °C region. See **Paper IV**, for a more complete discussion on the results and factors affecting the measurement accuracy.

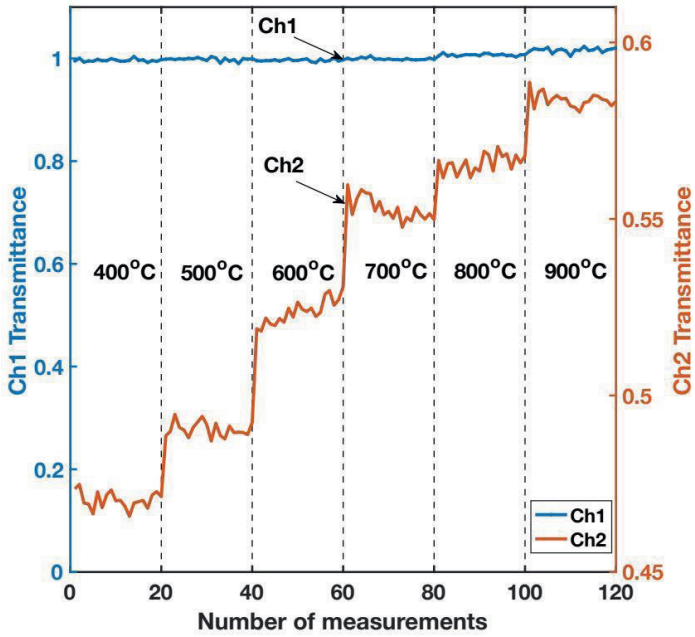

Figure 18. Measured transmittance of the furnace as a function of temperature for two wavelength channels (Ch1 and Ch2). Each data point in the curve consists of ten thousand laser pulses. Adapted from Paper IV.

5.5 Backscattering measurements at a large-scale combustion unit

In order for the supercontinuum lidar to work on-site, it needs to be able to collect light that is backscattered from soot and ash particles. This ability was evaluated by carrying out a one-day measurement campaign at Naistenlahti combined heat and power plant in Tampere, Finland. The results are not included in **Paper IV** but are shortly discussed here as they are relevant for the applicability of the technique. Naistenlahti 2 uses a mixture of wood and peat as fuel, generating 60 MW of electricity and 120 MW of heat. The combustion unit is ten meters wide with a few inspection windows on most floors, one of which was used to gain optical access to the CU – see Fig. 19 (a).

Rather than attempting to accurately quantify backscattering parameters, the goal was to see if any backscattered light could be detected at all. We devised an ad-hoc setup consisting of a nanosecond laser, together with two-inch collection

optics and an avalanche photodiode module in a coaxial configuration. The laser produced 800 mW of average power at 1.5 μm with 700-ps pulse width. Some of the results are shown in Figure 19 (b). Even though the signal-to-noise ratio was relatively poor, and the optics were not optimized to collect light along the full ten-meter distance, we were able to detect relatively strong signal from soot and ash particles. The signal strength was comparable to the instrument reflection and the back wall reflection signals, which suggests that soot and fly-ash can be utilized as effective backscatterers with these pulse parameters. Furthermore, we note that the continuous thermal radiation seen in Figure 19 (a) is a negligible source of noise compared to the instantaneous laser pulse power at nanosecond timescale.

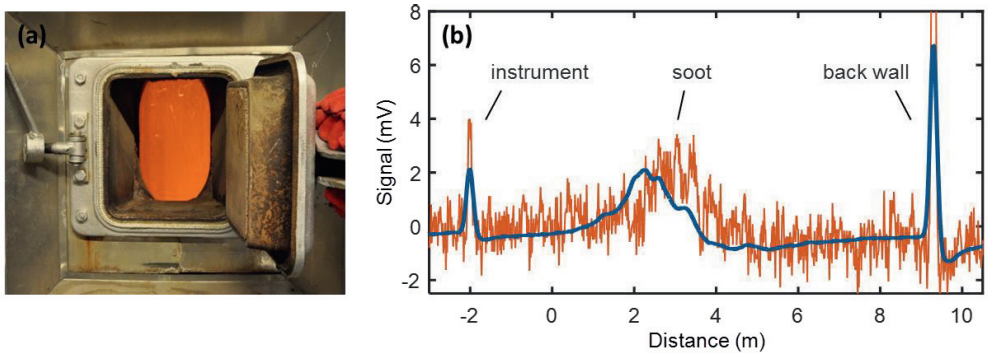

Figure 19. **(a)** Photograph taken through an inspection window of the combustion unit at Naistenlahti power plant. The back wall of the combustion unit can just be seen. **(b)** Single-pulse and 1000-pulse mean backscattering signal. Parts of the signal coming from different scatterers on the beam path are marked.

5.6 Future prospects of the supercontinuum lidar

The supercontinuum lidar is currently being further developed. The first step is to repeat the temperature measurements of **Paper IV** in a large-scale combustion unit. The main challenge is the lower back-scattering signal strength compared to the laboratory conditions. Hypothetically, this can be compensated for by using better collection optics and more sensitive detectors, such as avalanche photodiodes. Since the concentration of water vapor is unknown and varies on the beam bath, the measurement must be carried out over at least three wavelength bandwidths to solve both, the concentration and the temperature profiles of H_2O. Finally, there is a possibility of observing unexpected scattering or wavelength-dependent absorption effects, which do not cancel out in the calculation. This

could potentially constitute a major source of noise, limiting the applicability of this technique.

In case the above problems are solved, there is great potential for optimization and miniaturization of the device by using modern near-IR photonics- and MEMS technology. Firstly, the pump source could be replaced with e.g. a microchip laser or a high-pulse-energy multi-mode fiber laser. Because of the short distance, beam quality is not critical, and supercontinuum generation has even been shown to enhance the output beam quality of a multimode pump laser [153]. Secondly, the multiplex filter system could be replaced with a single MEMS Fabry-Perot interferometer [145], allowing for rapid wavelength scanning. This would enable the lidar to gather spectral data over a broad bandwidth using a simpler setup that at the same time collects more light. With these and other improvements, the short-range supercontinuum lidar has the potential to act as a versatile temperature and concentration profiler in combustion monitoring as well as other short-range gas sensing applications.

6 SUMMARY AND OUTLOOK

There is an ever-increasing need to measure the physical world, whether it is to improve our health, to understand the changing environment, or to guide decisions made by an automated system. Light is one of the most elegant tools that we can use for this, as it allows for remote measurements, and interacts with matter in a subtle yet precise and instantaneous way. Alternative techniques based on separation of mixtures, chemical reactions or electrical probes may seem crude in comparison. New light sources, detectors and other photonics devices are currently being researched and developed with considerable investment – leading to some futurologists calling 21st century the century of photonics, following the century of electronics. This thesis contributes to this overall development by studying new types of supercontinuum light sources and their potential in novel gas sensing applications. Here, we will briefly summarize the specific contributions of this work, as well as discuss future prospects of these techniques.

While the physical mechanisms of supercontinuum generation are now well-known, there is still much work to be done in understanding and improving the coherence properties of these sources as well as developing them for new regions of the electromagnetic spectrum. In **Paper I**, we contributed to this work by investigating spectral fluctuations observed in a supercontinuum that was generated in the UV region. These fluctuations were found to exhibit Gaussian statistics in the "saturated region" of the Raman-continuum, which suddenly changed to extreme-value statistics near the red-wavelength edge or the "unsaturated region". These effects are very similar to those observed in other regimes of nonlinear pulse propagation, such as those driven by modulation instability [80]. Inspired by the analysis published in Refs. [88, 89], the statistical treatment was further expanded in Chapter 3 of this thesis by including a previously unpublished correlation map analysis. The significance of this work can be looked at in two ways. On the one hand, these results are a unique contribution to the field of optical rogue waves [84, 166], which studies extreme amplitude effects in optical systems. On the other hand, the results are of practical interest to anyone dealing with ultraviolet or long-pulse supercontinuum sources, as well as fiber lasers and amplifiers [56, 81, 166-

168]. Most importantly, they suggest that poor noise performance can be expected in the unsaturated region of a Raman-continuum due to the fact that a relatively small number of pulses contribute to most of the light observed at these wavelengths.

After studying supercontinuum stability, we focused on coherent broadband cavity-enhanced absorption spectroscopy, which is an ultra-sensitive method for the multi-component gas sensing – a technique greatly benefits from the brightness, beam quality, and bandwidth of the supercontinuum. In **Paper II**, we demonstrated a record-breaking sensitivity for this technique using a custom near-IR light source that had more than a hundred times more spectral intensity compared to previous reports [118, 124-128]. This record ppb-level multi-component detection sensitivity for IBB-CEAS compares favorably to even the most advanced single-wavelength cavity-enhanced methods, such as cavity ring-down spectroscopy [107]. In addition, we published a data analysis method that fixed some of the oversights of previous reports, increasing the accuracy and dynamic range of the technique. While there are many things that could be done to perfect the technique, the proof-of-concept IBB-CEAS spectrometer already has enough bandwidth and sensitivity to be used in e.g. exhaled breath analysis [99], climate studies [101], or other applications that require ppm-to-ppb level multi-component detection, as long as the target molecules have some weak absorption bands in the near-IR measurement range.

Ultimately though, the mid-infrared spectral window contains the strongest molecular absorption, making it the most desirable region for gas sensing. Laser spectroscopy in this region is typically performed using optical parametric oscillators and quantum cascade lasers [27, 63, 169-171]. To reach these wavelengths, a new supercontinuum source was developed by utilizing a compact fiber laser and an exotic soft-glass ZBLAN fiber. In the work reported in **Paper III**, we used this source to extend the IBB-CEAS technique to the mid-IR region for the first time, while at the same time achieving the broadest reported measurement bandwidth for this technique. However, the achieved sensitivity was roughly four orders of magnitude inferior compared to the near-IR setup and other previous reports [118, 124-128]. This was attributed to much lower spectral intensity, mirror reflectance, and detector sensitivity, as well as having to use the most unstable part of the SC spectrum. Even though the spectrometer setup could be improved upon in many ways, and strong absorption bands compensate for the lack of sensitivity, the technique is further away from practical applications than the

near-IR spectrometer. These results highlight some of the challenges that must be faced when pushing these techniques to longer wavelengths.

We also studied the use of supercontinuum light in an industrial measurement application. In **Paper IV**, we reported on a novel short-range lidar designed for profiling the temperature inside a large-scale combustion unit. This work was directly motivated by the urgent need for this type of data. When using inhomogeneous fuel, such as renewable biofuel, optimizing the combustion process requires spatially sensitive real-time measurements, so that the feeds of fuel, oxygen, and other process parameters can be accurately controlled. Doing so can significantly improve the efficiency, as well as reduce the amount of harmful emissions. This is a difficult problem that has been attempted to solve using thermocouple- [154], ultrasound- [155], and diode laser [159] grids, as well as Rayleigh- [163], and atomic fluorescence [172] thermometers with varying results. Our proof-of-concept supercontinuum differential absorption lidar achieved a remote temperature measurement accuracy of about 50 °C in laboratory conditions, which is better than what has been achieved with e.g. picosecond- [162, 163] and Scheimpflug [172, 173] lidars. The SC lidar is currently being further developed for higher sensitivity, measurement accuracy, and H_2O concentration measurement capability, with the goal of eventually being able to perform real-time 3D-profiling of these and other parameters in full scale combustion units. This novel work is likely to inspire ideas for developing supercontinuum laser radars for other applications as well.

To conclude, light-based technologies are behind many of the innovations that have changed our lives in the 21st century, but their brightest future is yet to come. When it comes to optical sensing techniques, the results of this thesis suggest that when harnessed correctly, supercontinuum sources might have a role to play in making that future even brighter.

REFERENCES

[1] E. G. Borisova, L. P. Angelova, and E. P. Pavlova, "Endogenous and Exogenous Fluorescence Skin Cancer Diagnostics for Clinical Applications," *IEEE Journal of Selected Topics in Quantum Electronics*, vol. 20, no. 2, pp. 211-222, 2014.

[2] S. Kharitonov, D. Yates, R. Robbins, P. Barnes, R. Logan-Sinclair, and E. Shinebourne, "Increased nitric oxide in exhaled air of asthmatic patients," *The Lancet*, vol. 343, no. 8890, pp. 133-135, 1994.

[3] A. Rezaie, M. Buresi, A. Lembo, H. Lin, R. McCallum, S. Rao, M. Schmulson, M. Valdovinos, S. Zakko, and M. Pimentel, "Hydrogen and methane-based breath testing in gastrointestinal disorders: the North American Consensus," *The American journal of gastroenterology*, vol. 112, no. 5, p. 775, 2017.

[4] A. Krilaviciute, J. A. Heiss, M. Leja, J. Kupcinskas, H. Haick, and H. Brenner, "Detection of cancer through exhaled breath: a systematic review," *Oncotarget*, vol. 6, no. 36, p. 38643, 2015.

[5] J. Paaso, *Moisture depth profiling in paper using near-infrared spectroscopy*. University of Oulu, 2007.

[6] J. Li, W. Chen, and H. Fischer, "Quantum cascade laser spectrometry techniques: a new trend in atmospheric chemistry," *Applied Spectroscopy Reviews*, vol. 48, no. 7, pp. 523-559, 2013.

[7] D. D. Arslanov, M. Spunei, J. Mandon, S. M. Cristescu, S. T. Persijn, and F. J. Harren, "Continuous-wave optical parametric oscillator based infrared spectroscopy for sensitive molecular gas sensing," *Laser & Photonics Reviews*, vol. 7, no. 2, pp. 188-206, 2013.

[8] R. R. Alfano, *The supercontinuum laser source: fundamentals with updated references*. Springer Verlag, 2006

[9] J. M. Dudley and J. R. Taylor, *Supercontinuum generation in optical fibers*. Cambridge University Press, 2010

[10] J. Alpern. "Line Spectra and the Bohr Model". Electronic Structure of Atoms 2019 [cited 10.10. 2020]; Available from: https://chem.libretexts.org.

[11] J. M. Hollas, *Modern spectroscopy*. John Wiley & Sons, 2004

[12] G. Grynberg, A. Aspect, and C. Fabre, *Introduction to quantum optics: from the semi-classical approach to quantized light*. Cambridge university press, 2010

[13] J. Buldyreva, N. Lavrentieva, and V. Starikov, *Collisional Line Broadening and Shifting of Atmospheric Gases: A Practical Guide for Line Shape Modeling by Current Semi-classical Approaches*. World Scientific, 2011

[14] S. Wartewig, *IR and Raman spectroscopy: fundamental processing*. John Wiley & Sons, 2006

[15] L. S. Rothman, I. E. Gordon, Y. Babikov, A. Barbe, D. Chris Benner, P. F. Bernath, M. Birk, L. Bizzocchi, V. Boudon, L. R. Brown, A. Campargue, K. Chance, et al., "The HITRAN2012 molecular spectroscopic database," *Journal of Quantitative Spectroscopy and Radiative Transfer*, vol. 130, pp. 4-50, 2013.

[16] J. Tarhasaari, *Atomi- ja molekyylispektritietokantojen hyödyntäminen MATLAB-ympäristössä*. Tampereen Teknillinen Yliopisto, 2010.

[17] I. E. Gordon, L. S. Rothman, C. Hill, R. V. Kochanov, Y. Tan, P. F. Bernath, M. Birk, V. Boudon, A. Campargue, and K. Chance, "The HITRAN2016 molecular spectroscopic database," *Journal of Quantitative Spectroscopy and Radiative Transfer*, vol. 203, pp. 3-69, 2017.

[18] L. Rothman, I. Gordon, R. Barber, H. Dothe, R. Gamache, A. Goldman, V. Perevalov, S. Tashkun, and J. Tennyson, "HITEMP, the high-temperature molecular spectroscopic database," *Journal of Quantitative Spectroscopy and Radiative Transfer*, vol. 111, no. 15, pp. 2139-2150, 2010.

[19] N. Jacquinet-Husson, J. Ballard, A. Barbe, G. Bjoraker, B. Bonnet, L. Brown, C. Camy-Peyret, J. P. Champion, A. Chédin, and A. Chursin, "The 1997 spectroscopic GEISA databank," *Journal of quantitative spectroscopy & radiative transfer*, vol. 62, no. 2, pp. 205-254, 1999.

[20] S. W. Sharpe, T. J. Johnson, R. L. Sams, P. M. Chu, G. C. Rhoderick, and P. A. Johnson, "Gas-phase databases for quantitative infrared spectroscopy," *Applied spectroscopy*, vol. 58, no. 12, pp. 1452-1461, 2004.

[21] L. Brown, M. Gunson, R. Toth, F. Irion, C. Rinsland, and A. Goldman, "1995 atmospheric trace molecule spectroscopy (ATMOS) linelist," *Applied optics*, vol. 35, no. 16, pp. 2828-2848, 1996.

[22] P. M. Chu, F. R. Guenther, G. C. Rhoderick, and W. J. Lafferty, "The NIST quantitative infrared database," *Journal of research of the National Institute of Standards and Technology*, vol. 104, no. 1, p. 59, 1999.

[23] D. L. Andrews and A. A. Demidov, *An introduction to laser spectroscopy*. Springer Science & Business Media, 2012

[24] W. Demtröder, *Laser spectroscopy: basic concepts and instrumentation*. Springer Science & Business Media, 2013

[25] K. C. Cossel, E. M. Waxman, I. A. Finneran, G. A. Blake, J. Ye, and N. R. Newbury, "Gas-phase broadband spectroscopy using active sources: progress, status, and applications [Invited]," *Journal of the Optical Society of America B*, vol. 34, no. 1, pp. 104-129, 2017.

[26] A. Fried and D. Richter, "Infrared absorption spectroscopy," *Analytical Techniques for Atmospheric Measurement*, pp. 72-146, 2006.

[27] W. Ye, C. Li, C. Zheng, N. P. Sanchez, A. K. Gluszek, A. J. Hudzikowski, L. Dong, R. J. Griffin, and F. K. Tittel, "Mid-infrared dual-gas sensor for simultaneous detection of methane and ethane using a single continuous-wave interband cascade laser," *Optics Express*, vol. 24, no. 15, pp. 16973-16985, 2016.

[28] P. Werle, F. Slemr, K. Maurer, R. Kormann, R. Mücke, and B. Jänker, "Near- and mid-infrared laser-optical sensors for gas analysis," *Optics and Lasers in Engineering*, vol. 37, no. 2, pp. 101-114, 2002.

[29] U. Platt and J. Stutz, *Differential optical absorption spectroscopy: principles and applications*. Springer Verlag, 2008

[30] W. Weng, C. Brackmann, T. Leffler, M. Alden, and Z. Li, "Ultraviolet Absorption Cross Sections of KOH and KCl for Nonintrusive Species-Specific Quantitative Detection in Hot Flue Gases," *Analytical chemistry*, vol. 91, no. 7, pp. 4719-4726, 2019.

[31] W. Denzer, G. Hancock, M. Islam, C. E. Langley, R. Peverall, G. A. D. Ritchie, and D. Taylor, "Trace species detection in the near infrared using Fourier transform broadband cavity enhanced absorption spectroscopy: initial studies on potential breath analytes," *Analyst*, vol. 136, pp. 801-806, 2011.

[32] N. Picqué and T. W. Hänsch, "Frequency comb spectroscopy," *Nature Photonics*, vol. 13, no. 3, pp. 146-157, 2019.

[33] G. Millot, S. Pitois, M. Yan, T. Hovhannisyan, A. Bendahmane, T. W. Hänsch, and N. Picqué, "Frequency-agile dual-comb spectroscopy," *Nature Photonics*, vol. 10, no. 1, pp. 27-30, 2016.

[34] G. Ycas, F. R. Giorgetta, E. Baumann, I. Coddington, D. Herman, S. A. Diddams, and N. R. Newbury, "High-coherence mid-infrared dual-comb spectroscopy spanning 2.6 to 5.2 μm," *Nature Photonics*, vol. 12, no. 4, pp. 202-208, 2018.

[35] M. Yan, P.-L. Luo, K. Iwakuni, G. Millot, T. W. Hänsch, and N. Picqué, "Mid-infrared dual-comb spectroscopy with electro-optic modulators," *Light: Science &Amp; Applications*, vol. 6, p. e17076, 2017.

[36] Z. Chen, T. W. Hänsch, and N. Picqué, "Mid-infrared feed-forward dual-comb spectroscopy," *Proceedings of the National Academy of Sciences*, p. 201819082, 2019.

[37] J. M. Dudley, G. Genty, and S. Coen, "Supercontinuum generation in photonic crystal fiber," *Reviews of modern physics*, vol. 78, pp. 1135-1184, 2006.

[38] A. Schliesser, N. Picqué, and T. W. Hänsch, "Mid-infrared frequency combs," *Nature Photonics*, vol. 6, p. 440, 2012.

[39] M. Yu, Y. Okawachi, A. G. Griffith, N. Picqué, M. Lipson, and A. L. Gaeta, "Silicon-chip-based mid-infrared dual-comb spectroscopy," *Nature Communications*, vol. 9, no. 1, p. 1869, 2018.

[40] Q. Lin, G. Niu, Q. Wang, Q. Yu, and Y. Duan, "Combined laser-induced breakdown with Raman spectroscopy: historical technology development and recent applications," *Applied Spectroscopy Reviews*, vol. 48, no. 6, pp. 487-508, 2013.

[41] V. Koskinen, J. Fonsen, K. Roth, and J. Kauppinen, "Progress in cantilever enhanced photoacoustic spectroscopy," *Vibrational spectroscopy*, vol. 48, no. 1, pp. 16-21, 2008.

[42] C. Weitkamp, *Lidar: range-resolved optical remote sensing of the atmosphere*. Vol. 102: Springer Science & Business, 2006

[43] P. A. Franken, A. E. Hill, C. W. Peters, and G. Weinreich, "Generation of Optical Harmonics," *Phys. Rev. Lett.*, vol. 7, pp. 118-119, 1961.

[44] R. R. Alfano and S. L. Shapiro, "Observation of self-phase modulation and small-scale filaments in crystals and glasses," *Physical Review Letters*, vol. 24, pp. 592-594, 1970.

[45] J. I. Gersten, R. Alfano, and M. Belic, "Combined stimulated Raman scattering and continuum self-phase modulations," *Physical review A*, vol. 21, no. 4, p. 1222, 1980.

[46] J. Knight, T. Birks, P. S. J. Russell, and D. Atkin, "All-silica single-mode optical fiber with photonic crystal cladding," *Optics letters*, vol. 21, no. 19, pp. 1547-1549, 1996.

[47] K. Saitoh and M. Koshiba, "Empirical relations for simple design of photonic crystal fibers," *Opt. Express*, vol. 13, pp. 267-274, 2005.

[48] T. A. Birks, J. C. Knight, and P. S. J. Russell, "Endlessly single-mode photonic crystal fiber," *Optics letters*, vol. 22, pp. 961-963, 1997.

[49] S. Coen, A. H. L. Chau, R. Leonhardt, J. D. Harvey, J. C. Knight, W. J. Wadsworth, and P. S. J. Russell, "Supercontinuum generation by stimulated Raman scattering and parametric four-wave mixing in photonic crystal fibers," *J. Opt. Soc. Am. B*, vol. 19, pp. 753-764, 2002.

[50] A. Aguirre, N. Nishizawa, J. Fujimoto, W. Seitz, M. Lederer, and D. Kopf, "Continuum generation in a novel photonic crystal fiber for ultrahigh resolution optical coherence tomography at 800 nm and 1300 nm," *Opt. Express*, vol. 14, pp. 1145-1160, 2006.

[51] J. K. Ranka, R. S. Windeler, and A. J. Stentz, "Visible continuum generation in air-silica microstructure optical fibers with anomalous dispersion at 800 nm," *Optics letters*, vol. 25, pp. 25-27, 2000.

[52] A. M. Heidt, A. Hartung, G. W. Bosman, P. Krok, E. G. Rohwer, H. Schwoerer, and H. Bartelt, "Coherent octave spanning near-infrared and visible supercontinuum generation in all-normal dispersion photonic crystal fibers," *Optics express*, vol. 19, no. 4, pp. 3775-3787, 2011.

[53] N. Nishizawa, "Generation and application of high-quality supercontinuum sources," *Optical Fiber Technology*, vol. 18, no. 5, pp. 394-402, 2012.

[54] A. Demircan, S. Amiranashvili, C. Brée, U. Morgner, and G. Steinmeyer, "Supercontinuum generation by multiple scatterings at a group velocity horizon," *Optics Express*, vol. 22, no. 4, pp. 3866-3879, 2014.

[55] R. D. Engelsholm and O. Bang, "Supercontinuum noise reduction by fiber undertapering," *Optics express*, vol. 27, no. 7, pp. 10320-10331, 2019.

[56] A. I. Adamu, M. S. Habib, C. R. Smith, J. E. A. Lopez, P. U. Jepsen, R. Amezcua-Correa, O. Bang, and C. Markos, "Noise and spectral stability of deep-UV gas-filled fiber-based supercontinuum sources driven by ultrafast mid-IR pulses," *Scientific reports*, vol. 10, no. 1, pp. 1-10, 2020.

[57] K. Kwarkye, M. Jensen, R. D. Engelsholm, M. K. Dasa, D. Jain, P. Bowen, P. M. Moselund, C. R. Petersen, and O. Bang, "In-amplifier and cascaded mid-infrared supercontinuum sources with low noise through gain-induced soliton spectral alignment," *Scientific Reports*, vol. 10, no. 1, pp. 1-11, 2020.

[58] S. R. DS, R. D. Engelsholm, I. B. Gonzalo, B. Zhou, P. Bowen, P. M. Moselund, O. Bang, and M. Bache, "Ultra-low-noise supercontinuum generation with a flat near-zero normal dispersion fiber," *Optics letters*, vol. 44, no. 9, pp. 2216-2219, 2019.

[59] S. Stark, J. Travers, and P. S. J. Russell, "Extreme supercontinuum generation to the deep UV," *Optics letters*, vol. 37, no. 5, pp. 770-772, 2012.

[60] K. F. Mak, J. C. Travers, P. Hölzer, N. Y. Joly, and P. S. J. Russell, "Tunable vacuum-UV to visible ultrafast pulse source based on gas-filled Kagome-PCF," *Optics express*, vol. 21, no. 9, pp. 10942-10953, 2013.

[61] Y. Yu, B. Zhang, X. Gai, C. Zhai, S. Qi, W. Guo, Z. Yang, R. Wang, D.-Y. Choi, and S. Madden, "1.8-10 μm mid-infrared supercontinuum generated in a step-index chalcogenide fiber using low peak pump power," *Optics letters*, vol. 40, no. 6, pp. 1081-1084, 2015.

[62] C. R. Petersen, U. Møller, I. Kubat, B. Zhou, S. Dupont, J. Ramsay, T. Benson, S. Sujecki, N. Abdel-Moneim, and Z. Tang, "Mid-infrared supercontinuum covering the 1.4–13.3 μm molecular fingerprint region using ultra-high NA chalcogenide step-index fibre," *Nature Photonics*, vol. 8, no. 11, p. 830, 2014.

[63] O. Mouawad, P. Béjot, F. Billard, P. Mathey, B. Kibler, F. Désévédavy, G. Gadret, J.-C. Jules, O. Faucher, and F. Smektala, "Filament-induced visible-to-mid-IR supercontinuum in a ZnSe crystal: Towards multi-octave supercontinuum absorption spectroscopy," *Optical Materials*, vol. 60, pp. 355-358, 2016.

[64] M. Belal, L. Xu, P. Horak, L. Shen, X. Feng, M. Ettabib, D. J. Richardson, P. Petropoulos, and J. H. V. Price, "Mid-infrared supercontinuum generation in

suspended core tellurite microstructured optical fibers," *Optics Letters*, vol. 40, no. 10, pp. 2237-2240, 2015.

[65] J. H. V. Price, T. M. Monro, H. Ebendorff-Heidepriem, F. Poletti, P. Horak, V. Finazzi, J. Y. Y. Leong, P. Petropoulos, J. C. Flanagan, G. Brambilla, and others, "Mid-IR supercontinuum generation from nonsilica microstructured optical fibers," *Selected Topics in Quantum Electronics, IEEE Journal of*, vol. 13, pp. 738-749, 2007.

[66] P. Domachuk, N. A. Wolchover, M. Cronin-Golomb, A. Wang, A. K. George, C. M. B. Cordeiro, J. C. Knight, and F. G. Omenetto, "Over 4000 nm bandwidth of mid-IR supercontinuum generation in sub-centimeter segments of highly nonlinear tellurite PCFs," *Optics Express*, vol. 16, pp. 7161-7168, 2008.

[67] C. Xia, M. Kumar, M.-Y. Cheng, R. S. Hegde, M. N. Islam, A. Galvanauskas, H. G. Winful, Fred L. Terry, Jr., M. J. Freeman, M. Poulain, and G. Mazé, "Power scalable mid-infrared supercontinuum generation in ZBLAN fluoride fibers with up to 1.3 watts time-averaged power," *Opt. Express*, vol. 15, pp. 865-871, 2007.

[68] D.-I. Yeom, E. C. Mägi, M. R. E. Lamont, M. A. F. Roelens, L. Fu, and B. J. Eggleton, "Low-threshold supercontinuum generation in highly nonlinear chalcogenide nanowires," *Opt. Lett.*, vol. 33, pp. 660-662, 2008.

[69] D. Jayasuriya, C. R. Petersen, D. Furniss, C. Markos, Z. Tang, M. S. Habib, O. Bang, T. M. Benson, and A. B. Seddon, "Mid-IR supercontinuum generation in birefringent, low loss, ultra-high numerical aperture Ge-As-Se-Te chalcogenide step-index fiber," *Optical Materials Express*, vol. 9, no. 6, pp. 2617-2629, 2019.

[70] B. Cumberland, J. Travers, S. Popov, and J. Taylor, "Toward visible cw-pumped supercontinua," *Optics letters*, vol. 33, no. 18, pp. 2122-2124, 2008.

[71] A. Kudlinski, G. Bouwmans, Y. Quiquempois, and A. Mussot, "Experimental demonstration of multiwatt continuous-wave supercontinuum tailoring in photonic crystal fibers," *Applied Physics Letters*, vol. 92, pp. 141103-141103, 2008.

[72] R. J. Bartula, J. W. Walewski, and S. T. Sanders, "Generation of ultraviolet broadband light in a single-mode fiber," *Applied Physics B: Lasers and Optics*, vol. 84, pp. 395-400, 2006.

[73] R. S. Watt, C. F. Kaminski, and J. Hult, "Generation of supercontinuum radiation in conventional single-mode fibre and its application to broadband absorption spectroscopy," *Applied Physics B: Lasers and Optics*, vol. 90, pp. 47-53, 2008.

[74] J. W. Walewski, J. A. Filipa, C. L. Hagen, and S. T. Sanders, "Standard single-mode fibers as convenient means for the generation of ultrafast high-pulse-energy super-continua," *Applied Physics B: Lasers and Optics*, vol. 83, pp. 75-79, 2006.

[75] G. Genty, S. Coen, and J. M. Dudley, "Fiber supercontinuum sources," *JOSA B*, vol. 24, no. 8, pp. 1771-1785, 2007.

[76] J. Grgic, S. Xiao, J. Mork, A.-P. Jauho, and N. A. Mortensen, "Slow-light enhanced absorption in a hollow-core fiber," *Opt. Express*, vol. 18, pp. 14270-14279, 2010.

[77] G. Qin, X. Yan, C. Kito, M. Liao, C. Chaudhari, T. Suzuki, and Y. Ohishi, "Ultrabroadband supercontinuum generation from ultraviolet to 6.28 mu m in a fluoride fiber," *Applied Physics Letters*, vol. 95, pp. 161103-161103, 2009.

[78] A. N. Ghosh, M. Meneghetti, C. R. Petersen, O. Bang, L. Brilland, S. Venck, J. Troles, J. M. Dudley, and T. Sylvestre, "Chalcogenide-glass polarization-maintaining photonic crystal fiber for mid-infrared supercontinuum generation," *Journal of Physics: Photonics*, vol. 1, no. 4, p. 044003, 2019.

[79] C. Zhang, Y. Qiu, R. Zhu, K. K. Wong, and K. K. Tsia, "Serial time-encoded amplified microscopy (STEAM) based on a stabilized picosecond supercontinuum source," *Optics express*, vol. 19, no. 17, pp. 15810-15816, 2011.

[80] D. R. Solli, C. Ropers, P. Koonath, and B. Jalali, "Optical rogue waves," *Nature*, vol. 450, no. 7172, pp. 1054-1057, 2007.

[81] K. Hammani, C. Finot, J. M. Dudley, and G. Millot, "Optical rogue-wave-like extreme value fluctuations in fiber Raman amplifiers," *Optics express*, vol. 16, no. 21, pp. 16467-16474, 2008.

[82] J. Kasparian, P. Béjot, J.-P. Wolf, and J. M. Dudley, "Optical rogue wave statistics in laser filamentation," *Optics express*, vol. 17, no. 14, pp. 12070-12075, 2009.

[83] J. M. Dudley, F. Dias, M. Erkintalo, and G. Genty, "Instabilities, breathers and rogue waves in optics," *Nature Photonics*, vol. 8, no. 10, p. 755, 2014.

[84] N. Akhmediev, B. Kibler, F. Baronio, M. Belić, W.-P. Zhong, Y. Zhang, W. Chang, J. M. Soto-Crespo, P. Vouzas, and P. Grelu, "Roadmap on optical rogue waves and extreme events," *Journal of Optics*, vol. 18, no. 6, p. 063001, 2016.

[85] B. R. Rankin, R. R. Kellner, and S. W. Hell, "Stimulated-emission-depletion microscopy with a multicolor stimulated-Raman-scattering light source," *Optics letters*, vol. 33, no. 21, pp. 2491-2493, 2008.

[86] L. Garcia, J. Jenkins, Y. Lee, N. Poole, K. Salit, P. Sidereas, C. G. Goedde, and J. R. Thompson, "Influence of classical pump noise on long-pulse multiorder stimulated Raman scattering in optical fiber," *JOSA B*, vol. 19, no. 11, pp. 2727-2736, 2002.

[87] A. Betlej, P. Schmitt, P. Sidereas, R. Tracy, C. G. Goedde, and J. R. Thompson, "Increased Stokes pulse energy variation from amplified classical noise in a fiber Raman generator," *Optics Express*, vol. 13, no. 8, pp. 2948-2960, 2005.

[88] D. Solli, G. Herink, B. Jalali, and C. Ropers, "Fluctuations and correlations in modulation instability," *Nature Photonics*, vol. 6, no. 7, p. 463, 2012.

[89] B. Wetzel, A. Stefani, L. Larger, P.-A. Lacourt, J.-M. Merolla, T. Sylvestre, A. Kudlinski, A. Mussot, G. Genty, and F. Dias, "Real-time full bandwidth measurement of spectral noise in supercontinuum generation," *Scientific reports*, vol. 2, p. 882, 2012.

[90] A. Okeefe and D. A. G. Deacon, "Cavity ring-down optical spectrometer for absorption measurements using pulsed laser sources," *Review of Scientific Instruments*, vol. 59, pp. 2544-2551, 1988.

[91] G. Berden and R. Engeln, *Cavity ring-down spectroscopy: techniques and applications*. John Wiley & Sons, 2009

[92] K. W. Busch and M. A. Busch, *Cavity-Ringdown Spectroscopy*. ACS Symposium Series. Vol. 720: American Chemical Society, 292, 1999

[93] G. Meijer, M. G. H. Boogaarts, R. T. Jongma, D. H. Parker, and A. M. Wodtke, "Coherent cavity ring down spectroscopy," *Chemical Physics Letters*, vol. 217, pp. 112-116, 1994.

[94] A. O'Keefe, "Integrated cavity output analysis of ultra-weak absorption," *Chemical Physics Letters*, vol. 293, pp. 331-336, 1998.

[95] I. Ventrillard, P. Gorrotxategi-Carbajo, and D. Romanini, "Part per trillion nitric oxide measurement by optical feedback cavity-enhanced absorption spectroscopy in the mid-infrared," *Applied Physics B*, vol. 123, no. 6, p. 180, 2017.

[96] J. Ye, L.-S. Ma, and J. L. Hall, "Ultrasensitive detections in atomic and molecular physics: demonstration in molecular overtone spectroscopy," *J. Opt. Soc. Am. B*, vol. 15, pp. 6-15, 1998.

[97] L. Ciaffoni, R. Peverall, and G. A. D. Ritchie, "Laser spectroscopy on volatile sulfur compounds: possibilities for breath analysis," *Journal of Breath Research*, vol. 5, pp. 024002-024002, 2011.

[98] M. R. McCurdy, Y. Bakhirkin, G. Wysocki, R. Lewicki, and F. K. Tittel, "Recent advances of laser-spectroscopy-based techniques for applications in breath analysis," *Journal of Breath Research*, vol. 1, pp. 014001-014001, 2007.

[99] C. Wang and P. Sahay, "Breath analysis using laser spectroscopic techniques: breath biomarkers, spectral fingerprints, and detection limits," *Sensors*, vol. 9, no. 10, pp. 8230-8262, 2009.

[100] F. M. Schmidt, M. Metsälä, O. Vaittinen, and L. Halonen, "Background levels and diurnal variations of hydrogen cyanide in breath and emitted from skin," *Journal of Breath Research*, vol. 5, pp. 046004-046004, 2011.

[101] D. B. Atkinson, "Solving chemical problems of environmental importance using cavity ring-down spectroscopy," *Analyst*, vol. 128, pp. 117-125, 2003.

[102] J. D. Ayers, R. L. Apodaca, W. R. Simpson, and D. S. Baer, "Off-axis cavity ringdown spectroscopy: application to atmospheric nitrate radical detection," *Appl. Opt.*, vol. 44, pp. 7239-7242, 2005.

[103] W. P. Dubé, S. S. Brown, H. D. Osthoff, M. R. Nunley, S. J. Ciciora, M. W. Paris, R. J. McLaughlin, and A. R. Ravishankara, "Aircraft instrument for simultaneous, in situ measurement of NO3 and N2O5 via pulsed cavity ring-down spectroscopy," *Review of scientific instruments*, vol. 77, pp. 034101-034101, 2006.

[104] J. Morville, D. Romanini, A. A. Kachanov, and M. Chenevier, "Two schemes for trace detection using cavity ringdown spectroscopy," *Applied Physics B: Lasers and Optics*, vol. 78, pp. 465-476, 2004.

[105] S. S. Brown, "Absorption spectroscopy in high-finesse cavities for atmospheric studies," *Chemical reviews*, vol. 103, pp. 5219-5238, 2003.

[106] E. R. Crosson, "A cavity ring-down analyzer for measuring atmospheric levels of methane, carbon dioxide, and water vapor," *Applied Physics B: Lasers and Optics*, vol. 92, pp. 403-408, 2008.

[107] C. Yver Kwok, O. Laurent, A. Guemri, C. Philippon, B. Wastine, C. W. Rella, C. Vuillemin, F. Truong, M. Delmotte, V. Kazan, M. Darding, B. Lebègue, et al., "Comprehensive laboratory and field testing of cavity ring-down spectroscopy analyzers measuring H2O, CO2, CH4 and CO," *Atmos. Meas. Tech.*, vol. 8, no. 9, pp. 3867-3892, 2015.

[108] I. Ventrillard, I. Xueref-Remy, M. Schmidt, C. Yver Kwok, X. Faïn, and D. Romanini, "Comparison of optical-feedback cavity-enhanced absorption spectroscopy and gas chromatography for ground-based and airborne measurements of atmospheric CO concentration," *Atmos. Meas. Tech.*, vol. 10, no. 5, pp. 1803-1812, 2017.

[109] G. Maisons, P. G. Carbajo, M. Carras, and D. Romanini, "Optical-feedback cavity-enhanced absorption spectroscopy with a quantum cascade laser," *Optics Letters*, vol. 35, no. 21, pp. 3607-3609, 2010.

[110] N. Lang, U. Macherius, M. Wiese, H. Zimmermann, J. Röpcke, and J. H. van Helden, "Sensitive CH4 detection applying quantum cascade laser based optical feedback cavity-enhanced absorption spectroscopy," *Optics Express*, vol. 24, no. 6, pp. A536-A543, 2016.

[111] J. B. Paul, L. Lapson, and J. G. Anderson, "Ultrasensitive absorption spectroscopy with a high-finesse optical cavity and off-axis alignment," *Applied Optics*, vol. 40, pp. 4904-4910, 2001.

[112] C. R. Markus, A. J. Perry, J. N. Hodges, and B. J. McCall, "Improving cavity-enhanced spectroscopy of molecular ions in the mid-infrared with up-conversion detection and Brewster-plate spoilers," *Optics Express*, vol. 25, no. 4, pp. 3709-3721, 2017.

[113] T. Werblinski, F. Mittmann, M. Altenhoff, T. Seeger, L. Zigan, and S. Will, "Temperature and water mole fraction measurements by time-domain-based supercontinuum absorption spectroscopy in a flame," *Applied Physics B*, vol. 118, no. 1, pp. 153-158, 2015.

[114] S. M. Ball and R. L. Jones, "Broad-band cavity ring-down spectroscopy," *Chemical reviews*, vol. 103, pp. 5239-5262, 2003.

[115] M. J. Thorpe, K. D. Moll, R. J. Jones, B. Safdi, and J. Ye, "Broadband cavity ringdown spectroscopy for sensitive and rapid molecular detection," *Science*, vol. 311, pp. 1595-1595, 2006.

[116] K. Stelmaszczyk, M. Fechner, P. Rohwetter, M. Queißer, A. Czyżewski, T. Stacewicz, and L. W "oste, "Towards supercontinuum cavity ring-down spectroscopy," *Applied Physics B: Lasers and Optics*, vol. 94, pp. 369-373, 2009.

[117] R. Engeln, G. von Helden, G. Berden, and G. Meijer, "Phase shift cavity ring down absorption spectroscopy," *Chemical Physics Letters*, vol. 262, no. 1-2, pp. 105-109, 1996.

[118] S. E. Fiedler, A. Hese, and A. A. Ruth, "Incoherent broad-band cavity-enhanced absorption spectroscopy," *Chemical Physics Letters*, vol. 371, pp. 284-294, 2003.

[119] H. Wang, J. Chen, and K. Lu, "Development of a portable cavity-enhanced absorption spectrometer for the measurement of ambient NO 3 and N 2 O 5: experimental setup, lab characterizations, and field applications in a polluted urban environment," *Atmospheric Measurement Techniques*, vol. 10, no. 4, p. 1465, 2017.

[120] B. Bernhardt, A. Ozawa, P. Jacquet, M. Jacquey, Y. Kobayashi, T. Udem, R. Holzwarth, G. Guelachvili, T. W. Hansch, and N. Picque, "Cavity-enhanced dual-comb spectroscopy," *Nat Photon*, vol. 4, no. 1, pp. 55-57, 2010.

[121] J. J. Scherer, J. B. Paul, H. Jiao, and A. O'Keefe, "Broadband ringdown spectral photography," *Applied Optics*, vol. 40, no. 36, pp. 6725-6732, 2001.

[122] G. Gagliardi and H.-P. Loock, *Cavity-enhanced spectroscopy and sensing*. Springer, 2014

[123] F. Adler, M. J. Thorpe, K. C. Cossel, and J. Ye, "Cavity-enhanced direct frequency comb spectroscopy: technology and applications," *Annual Review of Analytical Chemistry*, vol. 3, pp. 175-205, 2010.

[124] M. Triki, P. Cermak, G. Méjean, and D. Romanini, "Cavity-enhanced absorption spectroscopy with a red LED source for NO x trace analysis," *Applied Physics B: Lasers and Optics*, vol. 91, pp. 195-201, 2008.

[125] J. M. Langridge, T. Laurila, R. S. Watt, R. L. Jones, C. F. Kaminski, and J. Hult, "Cavity enhanced absorption spectroscopy of multiple trace gas species using a supercontinuum radiation source," *Optics Express*, vol. 16, pp. 10178-10188, 2008.

[126] P. S. Johnston and K. K. Lehmann, "Cavity enhanced absorption spectroscopy using a broadband prism cavity and a supercontinuum source," *Optics express*, vol. 16, no. 19, pp. 15013-15023, 2008.

[127] R. S. Watt, T. Laurila, C. F. Kaminski, and J. Hult, "Cavity Enhanced Spectroscopy of High-Temperature H2O in the Near-Infrared Using a Supercontinuum Light Source," *Applied spectroscopy*, vol. 63, pp. 1389-1395, 2009.

[128] C. F. Kaminski, R. S. Watt, A. D. Elder, J. H. Frank, and J. Hult, "Supercontinuum radiation for applications in chemical sensing and microscopy," *Applied Physics B: Lasers and Optics*, vol. 92, pp. 367-378, 2008.

[129] C. J. Young, R. A. Washenfelder, and S. S. Brown, "Cavity Enhanced Spectroscopy: Applications Theory and Instrumentation," *Encyclopedia of Analytical Chemistry*, 2010.

[130] K. Zheng, C. Zheng, Y. Zhang, and Y. Wang, "Review of Incoherent Broadband Cavity-Enhanced Absorption Spectroscopy (IBBCEAS) for Gas Sensing," *Sensors*, vol. 18, no. 11, p. 3646, 2018.

[131] S. M. Ball, J. M. Langridge, and R. L. Jones, "Broadband cavity enhanced absorption spectroscopy using light emitting diodes," *Chemical Physics Letters*, vol. 398, pp. 68-74, 2004.

[132] J. M. Langridge, S. M. Ball, and R. L. Jones, "A compact broadband cavity enhanced absorption spectrometer for detection of atmospheric NO 2 using light emitting diodes," *The Analyst*, vol. 131, pp. 916-922, 2006.

[133] W. Denzer, M. L. Hamilton, G. Hancock, M. Islam, C. E. Langley, R. Peverall, and G. A. D. Ritchie, "Near-infrared broad-band cavity enhanced absorption spectroscopy using a superluminescent light emitting diode," *Analyst*, vol. 134, pp. 2220-2223, 2009.

[134] P. S. Johnston and K. K. Lehmann, "Cavity enhanced absorption spectroscopy using abroadband prism cavity and a supercontinuumsource," *Opt. Express*, vol. 16, pp. 15013-15023, 2008.

[135] U. Platt, J. Meinen, D. Pühler, and T. Leisner, "Broadband Cavity Enhanced Differential Optical Absorption Spectroscopy (CE-DOAS)--applicability and corrections," *Meas. Tech*, vol. 2, pp. 713-723, 2009.

[136] T. Laurila, I. S. Burns, J. Hult, J. H. Miller, and C. F. Kaminski, "A calibration method for broad-bandwidth cavity enhanced absorption spectroscopy performed with supercontinuum radiation," *Applied Physics B: Lasers and Optics*, pp. 1-8, 2010.

[137] S. E. Fiedler, A. Hese, and U. Heitmann, "Influence of the cavity parameters on the output intensity in incoherent broadband cavity-enhanced absorption spectroscopy," *Review of Scientific Instruments*, vol. 78, pp. 073104-073104, 2007.

[138] W. R. Simpson, "Continuous wave cavity ring-down spectroscopy applied to in situ detection of dinitrogen pentoxide (NO)," *Review of scientific instruments*, vol. 74, pp. 3442-3442, 2003.

[139] K. Yin, B. Zhang, J. Yao, L. Yang, S. Chen, and J. Hou, "Highly stable, monolithic, single-mode mid-infrared supercontinuum source based on low-loss fusion spliced silica and fluoride fibers," *Optics letters*, vol. 41, no. 5, pp. 946-949, 2016.

[140] H. Kim, E. Plis, J. Rodriguez, G. Bishop, Y. Sharma, L. Dawson, S. Krishna, J. Bundas, R. Cook, and D. Burrows, "Mid-IR focal plane array based on type-II In As/ Ga Sb strain layer superlattice detector with n B n design," *Applied Physics Letters*, vol. 92, no. 18, p. 183502, 2008.

[141] R. F. Wolffenbuttel, "MEMS-based optical mini-and microspectrometers for the visible and infrared spectral range," *Journal of Micromechanics and Microengineering*, vol. 15, no. 7, p. S145, 2005.

[142] K. E. Jahromi, Q. Pan, L. Høgstedt, S. M. Friis, A. Khodabakhsh, P. M. Moselund, and F. J. Harren, "Mid-infrared supercontinuum-based upconversion detection for trace gas sensing," *Optics Express*, vol. 27, no. 17, pp. 24469-24480, 2019.

[143] P. Gelabert, E. Pruett, G. Perrella, S. Subramanian, and A. Lakshminarayanan. "DLP NIRscan Nano: an ultra-mobile DLP-based near-infrared Bluetooth spectrometer". in *Emerging Digital Micromirror Device Based Systems and Applications VIII*. 2016. International Society for Optics and Photonics.

[144] P. Nelson, "DLP Technology for Spectroscopy," *DLPA048 Texas Instruments*, 2014.

[145] J. S. Milne, J. M. Dell, A. J. Keating, and L. Faraone, "Widely tunable MEMS-based Fabry–Perot filter," *Journal of microelectromechanical systems*, vol. 18, no. 4, pp. 905-913, 2009.

[146] N. P. Ayerden, U. Aygun, S. T. Holmstrom, S. Olcer, B. Can, J.-L. Stehle, and H. Urey, "High-speed broadband FTIR system using MEMS," *Applied optics*, vol. 53, no. 31, pp. 7267-7272, 2014.

[147] E. Buchen, "SpaceWorks' 2014 nano/microsatellite market assessment," 2014.

[148] M. Kutila, P. Pyykönen, W. Ritter, O. Sawade, and B. Schäufele. "Automotive LIDAR sensor development scenarios for harsh weather conditions". in *2016 IEEE 19th International Conference on Intelligent Transportation Systems (ITSC)*. 2016. IEEE.

[149] W. Bao, H. Li, N. Li, and W. Jiang. "A liveness detection method for face recognition based on optical flow field". in *2009 International Conference on Image Analysis and Signal Processing*. 2009. IEEE.

[150] Y. Chen, E. Räikkönen, S. Kaasalainen, J. Suomalainen, T. Hakala, J. Hyyppä, and R. Chen, "Two-channel hyperspectral LiDAR with a supercontinuum laser source," *Sensors*, vol. 10, no. 7, pp. 7057-7066, 2010.

[151] S. Kaasalainen, T. Lindroos, and J. Hyyppa, "Toward hyperspectral lidar: Measurement of spectral backscatter intensity with a supercontinuum laser source," *IEEE Geoscience and Remote Sensing Letters*, vol. 4, no. 2, pp. 211-215, 2007.

[152] G. Méjean, J. Kasparian, E. Salmon, J. Yu, J.-P. Wolf, R. Bourayou, R. Sauerbrey, M. Rodriguez, L. Wöste, and H. Lehmann, "Towards a supercontinuum-based infrared lidar," *Applied Physics B*, vol. 77, no. 2-3, pp. 357-359, 2003.

[153] A. Manninen, T. Kääriäinen, T. Parviainen, S. Buchter, M. Heiliö, and T. Laurila, "Long distance active hyperspectral sensing using high-power near-infrared supercontinuum light source," *Optics express*, vol. 22, no. 6, pp. 7172-7177, 2014.

[154] D. Bradley and K. Matthews, "Measurement of high gas temperatures with fine wire thermocouples," *Journal of Mechanical Engineering Science*, vol. 10, no. 4, pp. 299-305, 1968.

[155] H. Y. Zhang, K. B. Xu, F. Q. Xie, and Y. Liu. "Temperature field reconstruction system based on ultrasonic time-of-flight technique". in *Applied Mechanics and Materials*. 2013. Trans Tech Publ.

[156] A. Farooq, J. B. Jeffries, and R. K. Hanson, "In situ combustion measurements of H2O and temperature near 2.5 μm using tunable diode laser absorption," *Measurement Science and Technology*, vol. 19, no. 7, p. 075604, 2008.

[157] J. Liu, J. Jeffries, and R. Hanson, "Wavelength modulation absorption spectroscopy with 2 f detection using multiplexed diode lasers for rapid temperature measurements in gaseous flows," *Applied Physics B*, vol. 78, no. 3-4, pp. 503-511, 2004.

[158] X. Zhou, J. Jeffries, and R. Hanson, "Development of a fast temperature sensor for combustion gases using a single tunable diode laser," *Applied Physics B*, vol. 81, no. 5, pp. 711-722, 2005.

[159] G. B. Rieker, J. B. Jeffries, and R. K. Hanson, "Calibration-free wavelength-modulation spectroscopy for measurements of gas temperature and concentration in harsh environments," *Applied optics*, vol. 48, no. 29, pp. 5546-5560, 2009.

[160] C. S. Goldenstein, R. M. Spearrin, J. B. Jeffries, and R. K. Hanson, "Infrared laser-absorption sensing for combustion gases," *Progress in Energy and Combustion Science*, vol. 60, pp. 132-176, 2017.

[161] T. Leffler, C. Brackmann, A. Ehn, B. Kaldvee, M. Aldén, M. Berg, and J. Bood, "Range-resolved detection of potassium chloride using picosecond differential absorption light detection and ranging," *Applied optics*, vol. 54, no. 5, pp. 1058-1064, 2015.

[162] B. Kaldvee, J. Bood, and M. Aldén, "Picosecond-lidar thermometry in a measurement volume surrounded by highly scattering media," *Measurement Science and Technology*, vol. 22, no. 12, p. 125302, 2011.

[163] B. Kaldvee, A. Ehn, J. Bood, and M. Aldén, "Development of a picosecond lidar system for large-scale combustion diagnostics," *Applied optics*, vol. 48, no. 4, pp. B65-B72, 2009.

[164] J. Borggren, W. Weng, A. Hosseinnia, P.-E. Bengtsson, M. Aldén, and Z. Li, "Diode laser-based thermometry using two-line atomic fluorescence of indium and gallium," *Applied Physics B*, vol. 123, no. 12, p. 278, 2017.

[165] J. Viljanen, T. Sorvajärvi, and J. Toivonen, "In situ laser measurement of oxygen concentration and flue gas temperature utilizing chemical reaction kinetics," *Optics letters*, vol. 42, no. 23, pp. 4925-4928, 2017.

[166] Z. Liu, S. Zhang, and F. W. Wise, "Rogue waves in a normal-dispersion fiber laser," *Optics Letters*, vol. 40, no. 7, pp. 1366-1369, 2015.

[167] A. F. J. Runge, C. Aguergaray, N. G. R. Broderick, and M. Erkintalo, "Raman rogue waves in a partially mode-locked fiber laser," *Optics Letters*, vol. 39, no. 2, pp. 319-322, 2014.

[168] S. Kobtsev, S. Kukarin, S. Smirnov, and I. Ankudinov, "Cascaded SRS of single- and double-scale fiber laser pulses in long extra-cavity fiber," *Optics Express*, vol. 22, no. 17, pp. 20770-20775, 2014.

[169] D. Richter, D. Lancaster, R. Curl, W. Neu, and F. Tittel, "Compact mid-infrared trace gas sensor based on difference-frequency generation of two diode lasers in periodically poled LiNbO3," *Applied Physics B: Lasers and Optics*, vol. 67, no. 3, pp. 347-350, 1998.

[170] I. Armstrong, W. Johnstone, K. Duffin, M. Lengden, A. L. Chakraborty, and K. Ruxton, "Detection of CH4 in the Mid-IR Using Difference Frequency Generation With Tunable Diode Laser Spectroscopy," *Journal of Lightwave Technology*, vol. 28, no. 10, pp. 1435-1442, 2010.

[171] W. Chen, G. Mouret, D. Boucher, and F. Tittel, "Mid-infrared trace gas detection using continuous-wave difference frequency generation in periodically poled RbTiOAsO4," *Applied Physics B*, vol. 72, no. 7, pp. 873-876, 2001.

[172] E. Malmqvist, J. Borggren, M. Aldén, and J. Bood, "Lidar thermometry using two-line atomic fluorescence," *Applied optics*, vol. 58, no. 4, pp. 1128-1133, 2019.

[173] E. Malmqvist, M. Brydegaard, M. Aldén, and J. Bood, "Scheimpflug Lidar for combustion diagnostics," *Optics Express*, vol. 26, no. 12, pp. 14842-14858, 2018.

PUBLICATIONS

PAPER
I

Extreme-value statistics in supercontinuum generation by cascaded stimulated Raman scattering

A. Aalto, G. Genty, and J. Toivonen

Optics express, vol. 18, no. 2, pp. 1234-1239, 2010.
https://doi.org/10.1364/OE.18.001234

Extreme-value statistics in supercontinuum generation by cascaded stimulated Raman scattering

Antti Aalto,* Goëry Genty, and Juha Toivonen

Tampere University of Technology, Optics Laboratory, FIN-33101 Tampere, Finland
*antti.2.aalto@tut.fi

Abstract: We study experimentally the statistical fluctuations observed in a supercontinuum generated in the normal dispersion regime through cascaded stimulated Raman scattering. Specifically, we show that the statistical distribution of shot-to-shot spectral variations evolves from a quasi-Gaussian in the saturated regime for Stokes orders near the pump to a long-tailed extreme-value distribution for Stokes orders at a large separation from the pump in the unsaturated regime.

OCIS codes: (190.4370) Nonlinear optics, fibers; (190.5650) Raman effect; (190.5890) Scattering, stimulated; (320.6629) Supercontinuum generation.

References and links

1. J. M. Dudley, G. Genty, and S. Coen, "Supercontinuum generation in photonic crystal fiber," Rev. Mod. Phys. **78**, 1135-1184 (2006).
2. D. Solli, C. Ropers, P. Koonath, and B. Jalali, "Optical rogue waves," Nature **450**, 1054-1057 (2007).
3. K. Hammani, C. Finot, J. M. Dudley, and G. Millot, "Optical rogue-wave-like extreme value fluctuations in fiber Raman amplifiers," Opt. Express **16**, 16467-16474 (2008), http://www.opticsinfobase.org/oe/abstract.cfm?URI=oe-16-21-16467.
4. D. Borlaug and B. Jalali, "Extreme value statistics in silicon photonics," in proceedings of the 21st Annual Meeting of the IEEE Lasers & Electro-Optics Society, Newport Beach, USA, 2008.
5. A. Maluckov, L. Hadžievski, N. Lazarides, and G. P. Tsironis, "Extreme events in discrete nonlinear lattices," Phys. Rev. E **79**, 025601 (2009).
6. J. Kasparian, P. Béjot, J. P. Wolf, and J. Dudley, "Optical rogue wave statistics in laser filamentation," Opt. Express **17**, 12070-12075 (2009), http://www.opticsinfobase.org/oe/abstract.cfm?URI=oe-17-14-12070.
7. M. Erkintalo, G. Genty, and J. M. Dudley, "Rogue wave like characteristics in femtosecond supercontinuum generation," Opt. Lett. **34**, 2468-2470 (2009) .
8. A. S. Grabtchikov, S. Ya. Kilin, V. P. Kozich, and N. M. Iodo, "Statistics of the energy fluctuations of Stokes pulses in stimulated Raman scattering in various situations," JETP Lett. **43**, 151-156 (1986).
9. A. S. Grabtchikov, A. I. Vodtchits, and V. A. Orlovich, "Pulse-energy statistics in the linear regime of stimulated Raman scattering with a broad-band pump," Phys. Rev. A **56**, 1666-1669 (1997).
10. E. Landahl, D. Baiocchi, and J. R. Thompson, "A simple analytic model for noise shaping by an optical fiber Raman generator," Opt. Commun. **150**, 339-347 (1998).
11. L. Garcia, J. Jenkins, Y. Lee, N. Poole, K. Salit, P. Sidereas, C. G. Goedde, and J. R. Thompson, "Influence of classical pump noise on long-pulse multiorder stimulated Raman scattering in optical fiber," J. Opt. Soc. Am. B **19**, 2727-2736 (2002).
12. A. Betlej, P. Schmitt, P. Sidereas, R. Tracy, C. G. Goedde, and J. R. Thompson, "Increased Stokes pulse energy variation from amplified classical noise in a fiber Raman generator," Opt. Express **13**, 2948-2960 (2005), http://www.opticsinfobase.org/oe/abstract.cfm?URI=oe-13-8-2948.
13. R. H. Stolen, C. Lee, and R. K. Jain, "Development of the stimulated Raman spectrum in single-mode silica fibers," J. Opt. Soc. Am. B **1**, 652-657 (1984).
14. K. X. Liu and E. Garmire, "Understanding the Formation of the SRS Stokes Spectrum in Fused Silica Fibers," IEEE J. Quantum Electron. **27**, 1022-1030 (1991).
15. B. R. Rankin, R. R. Kellner, and S. W. Hell, "Stimulated-emission-depletion microscopy with a multicolor stimulated-Raman-scattering light source," Opt. Lett. **33**, 2491-2493 (2008).

1. Introduction

It is now well known that supercontinuum (SC) generation in the long pulse regime is very sensitive to the input noise of the pump pulses resulting in poor coherence properties and stability [1]. Recently, it was shown that the large shot-to-shot fluctuations inherent to this particular regime originate from noise-seeded modulation instability (MI) that can trigger the generation of pulses with abnormally high intensity [2]. Such pulses are now commonly referred to as optical "rogue" waves and they have been shown to be associated with long-tailed statistical distributions indicating these extreme events occur with an increased probability in contrast to that predicted by Gaussian statistics [2]. These findings have attracted significant interest and stimulated a number of detailed studies reporting similar statistical characteristics in various nonlinear regimes of pulse propagation [3-7].

Extreme-value fluctuations have been found in various types of nonlinear systems where the noise of the initial state can have a dramatic effect on the final state of the system. For instance, in the context of fiber optics, Hammani *et al*. have demonstrated "rogue-wave-like" statistics in Raman amplification where the noise from a partially incoherent pump wave can lead to significant changes in the properties of the amplified wave [3]. Although the noise-driven nonlinear dynamics associated with "rogue" events have been primarily reported for fiber-based systems, research on extreme-value behavior has also recently expanded in other areas of optics and a range of nonlinear optical phenomena exhibiting similar rogue-like characteristics have been reported. Indeed, extreme-value behavior was observed in Raman amplification on a silicon chip [4], or during filamentation in air [6].

In this paper we report on another example of nonlinear pulse propagation where significant shot-to-shot variations occur as a result of nonlinear stimulated Raman scattering (SRS) dynamics leading to a long-tailed, "rogue-wave-like" statistical distribution. Noise transfer mechanisms in SRS leading to non-Gaussian statistics are well known and a number of earlier studies have investigated the statistical variations in the energy of the first Stokes pulse generated by SRS [8-12]. In particular, it was shown both experimentally and theoretically using a simple analytical model [13-14] that fluctuations in the intra-pulse modulation of nanosecond pulses due to longitudinal modes beating can induce significant variations in the energy of the first-order Stokes pulse and that the overall shape of the corresponding statistical distribution was also power-dependent [10].

Here we focus on the spectral fluctuations observed in the highly nonlinear regime of SRS where a large number of Stokes orders are generated leading to the formation of a broadband supercontinuum spectrum in the UV region where SRS is enhanced. Specifically, we use nanosecond pulses launched into a highly nonlinear fiber to generate a SC whose dynamics are mainly dominated by cascaded SRS. Using a short wavelength pump at 355 nm in combination with a single-mode fiber is one of the simplest and most cost-effective methods to generate a broadband UV-SC source. Therefore, this particular experimental configuration is of significant interest as this type of UV-SC light source can be used in a wide range of applications such as e.g. spectroscopy or microscopy [15]. Significant variations are observed in the SC spectrum and the fully captured single-shot spectra allow us to study in detail the shot-to-shot fluctuations of the SC at the output of the fiber. Our experimental results reveal that "classical pump noise" results in "rogue-wave-like" statistics for wavelengths close to the long wavelength edge of the SC spectrum. Furthermore, we quantify the variations across the entire bandwidth of the SC spectrum and show that the fluctuations are strongly wavelength-dependent, evolving from a quasi-Gaussian towards an L-shape distribution for increased detuning with respect to the pump wavelength.

2. Experimental setup

A broadband UV-SC was generated by launching nanosecond pulses into a 40 m long polarization-maintaining fiber with a 2.3 μm core diameter specially manufactured for low

UV attenuation (Nufern PM-S350-HP). The fiber has a pure-silica core and is single-mode for wavelengths above 350 nm. The 8-ns long laser pulses were produced by an electro-optically Q-switched, frequency-tripled Nd:YAG laser (EKSPLA NL202) operating at 355 nm with a 10 Hz repetition rate. The pulse energy was attenuated to the microjoule regime using a variable optical attenuator in order not to exceed the damage threshold of the fiber. Although in our experiments the input polarization was adjusted so as to match one of the principal axes of polarization of the fiber, we have checked that the observations reported here are in fact independent of the input state of polarization. In fact, we have also found experimentally (not shown here) that similar results are observed when a non polarization-maintaining fiber is used with the exception of a much less pronounced individual Raman peaks and smoother spectrum. The pulses were subsequently coupled into the fiber with a microscope objective specially designed for UV light (OFR-LMU-10X-λ) and the fiber input end was mounted on a highly sensitive *XYZ*-flexure stage for optimal coupling. A silicon photodiode with a 140 ps rise/fall time combined with a 2 GHz oscilloscope was used to monitor the temporal profile of the pulses prior to coupling. The output end of the fiber was connected to the entrance aperture of a spectrograph allowing to capture single-shot spectra through an ICCD camera mounted on the spectrograph exit aperture. The detection setup was connected to a PC allowing for automated measurements. Figure 1(a) shows a schematic of the experimental setup and an example of a generated SC is shown in Fig. 1(b).

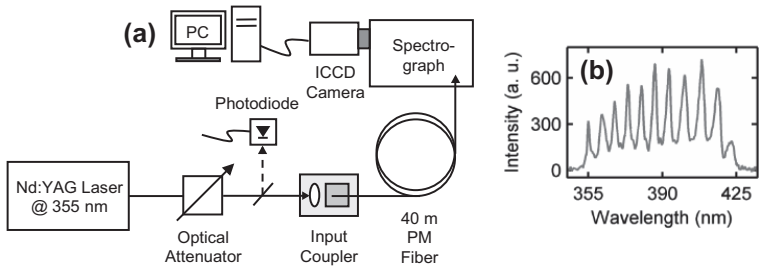

Fig. 1. (a) Experimental setup. (b) Example of a generated SC spectrum.

The extreme spectral broadening of the pump is mostly caused by cascaded stimulated Raman scattering, which results in distinct spectral peaks separated by c.a. 13 THz. When recording the SC spectra generated by subsequent pulses we observed significant shot-to-shot variations. In order to clarify the origin of these fluctuations we have first characterized the inherent fluctuations in the input pulse characteristics delivered by the Q-switched laser as one can expect these variations to influence the fluctuations of the SC spectra. Specifically, the temporal profile of the pump pulses was observed to be highly modulated due to the beating of multiple longitudinal modes inside the laser cavity. As the number of modes and relative phases are random the modulation varies strongly from pulse-to-pulse as shown in Fig. 2(a-d) where examples of different measured pulse envelopes are plotted. We emphasize that the 2 GHz bandwidth of the detection system is much larger than that used in earlier experiments on the characterization of the first-order Stokes pulse energy fluctuations [11]. On one hand, this allows us to characterize with better accuracy the temporal envelope compared to Ref. 11, where, most probably due to the limited bandwidth of the detection system, a nearly ideal sinusoidal modulation was measured. On the other hand, even with our detection system, it is possible that higher harmonics may still be filtered out and that the ultrafast modulation may thus be not fully resolved.

The variations in the characteristics of the input pump pulses are illustrated in a more quantitative way in Fig. 2(e) which shows a histogram representation of the input pulse peak power corresponding to 9000 input pulses. The peak power distribution is seen to be close to Gaussian but with a small tail and with a relative standard deviation of approximately 23 % of the mean. The tail corresponds to the rare cases where multiple modes are in phase, generating exceptionally high peak power pulses (see Fig. 2(c)). Here we choose to focus on the peak

power fluctuations of the input pulse rather than that of the pulse energy as we expect the cascaded SRS process to be more sensitive to the former quantity.

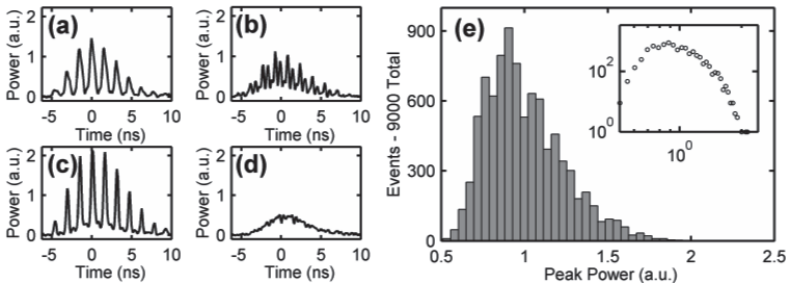

Fig. 2. (a-d) Examples of pump pulse envelopes captured prior to coupling together with the measured peak power distribution (e). Inset shows the histogram on a log-log scale.

In addition to the "classical pump noise" of the Q-switched laser, possible fluctuations in fiber-coupling efficiency were also quantified as they may impact the overall input noise level. For this purpose, a 10 cm piece of fiber was used to evaluate the shot-to-shot changes in coupling efficiency. A short length was intentionally used in order to prevent any nonlinear process which could alter the result. The coupling efficiency was found to exhibit a near-Gaussian distribution with a mean coupling efficiency of 0.50 and a relative standard deviation of 2.6 %. The shot-to-shot changes in coupling efficiency are therefore a negligible source of additional noise compared to the intrinsic fluctuations of the pulses. Finally, in order to eliminate contribution to the observed spectral fluctuations that would arise from possible multi-mode coupling, we have checked with a selection of spectral filters that all the spectral components generated along the fiber occurred in the fundamental mode.

3. Results and discussion

We recorded two sets of 9000 single-shot spectra at the fiber output corresponding to higher and lower mean energy values of the input pulses, respectively. We focus mainly on the experimental results obtained using the higher mean energy value which was estimated to be 1.0 μJ (coupled energy). The measurement results for the lower energy case of 0.2 μJ are presented briefly at the end of the section as we did not find any major qualitative difference between those two cases. Figure 3(a) superimposes 500 individual spectra recorded at the output of the fiber. The mean spectrum calculated over the whole set of 9000 spectra is also displayed. The spectra show significant broadening towards the longer wavelengths with as many as 6 to 12 Stokes lines generated in the cascaded SRS process. Significantly, the long wavelength edge of the SC spectrum shows large shot-to-shot variations in terms of both spectral location and overall shape. To illustrate further the large discrepancy observed in the recorded single-shot spectra, Fig. 3(b-d) shows selected cases corresponding to narrow, intermediate, and large spectral bandwidth, respectively. A difference as large as 6 Stokes orders between extreme cases can be observed in the output spectra.

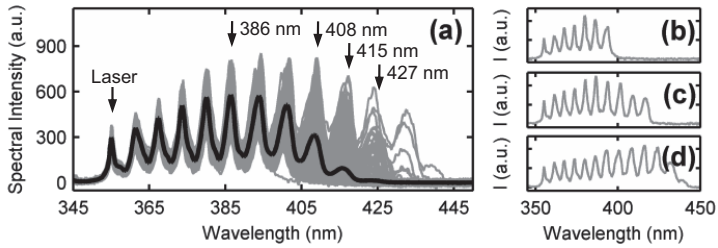

Fig. 3. (a) Superimposed experimental single-shot spectra (for clarity, only 500 spectra are shown) and the mean calculated over the 9000 spectra (black line). Arrows indicate the wavelengths at which the intensity histograms are calculated. (b), (c), (d) Examples of individual SC spectra highlighting the significant shot-to-shot variations.

To further characterize these variations quantitatively (and for consistency with other related studies [1,6,7]), histograms of spectral intensities were calculated at selected wavelengths of 386 nm, 416 nm, 421 nm, and 427 nm corresponding to the 5th, 8th, 9th, and 10th Stokes orders, as indicated by the arrows in Fig. 3(a). The histograms are presented in Fig. 4(a-d). The histograms show a rapid transformation from a bell-like shape distribution into an L-shape distribution for spectral intensities at wavelengths located further from the pump. This type of evolution has been recently observed in a different context where it was attributed to the formation of optical "rogue" waves [7]. Although here there are clearly no optical "rogue" waves in the sense observed in earlier experiments [2], the measured shot-to-shot fluctuations near the edge of the broadband SC spectrum are the manifestation of extreme-value events. The drastic change in the statistics is more conveniently observed on a log-log scale as shown in the insets in Fig. 4, where the initial bell-shape curve gradually evolves towards a quasi-linear shape, indicative of a power-law dependence.

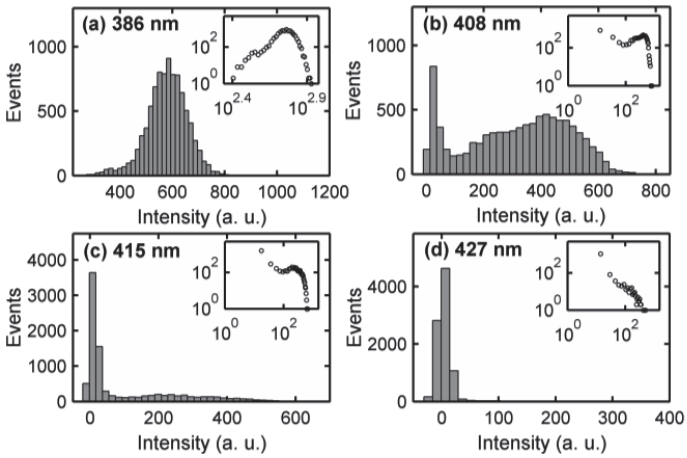

Fig. 4. Histograms of recorded spectral intensity at selected wavelengths of (a) 386 nm, (b) 408 nm, (c) 415 nm, and (d) 427 nm. Insets show the histograms on a log-log scale.

In addition to calculating histograms at few selected wavelengths, we took advantage of the fact that we could capture entire individual spectra and performed a full wavelength-dependence analysis of the statistics as recently introduced by Kasparian *et al*. [6]. Following the analysis of Ref. 6, we use the convenient "Pareto-like" metric $M(\lambda)$ (1) to characterize the skewness of the distribution across the full spectral bandwidth of the SC spetcrum. The metric M at a given wavelength λ_0 is defined as the contribution of 20% of the largest measured intensities to the total sum of all measured intensities and can be calculated from [6]

$$M(\lambda_0) = \sum_{i=1}^{0.2N} I_i(\lambda_0) \Big/ \sum_{i=1}^{N} I_i(\lambda_0), \qquad (1)$$

where the intensities I_i are sorted in a descending order from indices 1 to N. The lowest possible value for M is 0.2 for uniform distribution. $M \approx 0.44$ corresponds to a Gaussian distribution, while values exceeding 0.5 indicate long-tailed L-shape statistics. Figure 5 shows the mean spectrum together with the metric $M(\lambda)$ calculated for the two measurement ensembles performed at (a) low and (b) high input peak power level, respectively. The emergence of long-tailed L-shape distributions on the long wavelength edge of the spectrum as was observed in Fig. 4 (c-d) can be clearly seen to correlate with a rapid increase in the "Pareto-metric" $M(\lambda)$ in Fig. 5(b). For spectral components above 410 nm corresponding to the 9th Stokes order, the M-value exceeds 0.44 indicating a change in the statistical distribution towards an L-shape, which is consistent with what was observed from the histogram evolution. Figure 5(a) shows that the tendency of the SC to exhibit extreme-value behavior is also present in the lower peak power regime where much less Stokes order are

generated on average. Furthermore, we observe that the *M*-value or skewness of the statistical distribution remains low (i.e. below 0.44) for Stokes orders which are saturated, irrespective of the mean input energy value. Our experimental results are in agreement with the numerical predictions of Ref. 12 obtained with a pump noise similar to that of our experiments. In fact, we believe that similar results would be obtained independently of the source of noise.

In order to confirm that classical pump noise amplified through cascaded SRS process is responsible for the significant spectral fluctuations, we simulated the nonlinear propagation in our fiber for an ensemble of 1000 Gaussian pulses with a normal peak power distribution having a 23 % standard deviation. The numerical model we use is similar to that introduced in Refs. 13 and 14 and includes spontaneous and stimulated Raman scattering as well as the fiber losses. Although this is clearly a simplified model which neglects the instantaneous nonlinear response and the walk-off effects, it nevertheless reproduces our experimental results qualitatively well. Specifically, it predicts the correct number of Stokes orders generated along the fiber and the calculated *M*-value increases towards the longer wavelengths for unsaturated Stokes orders similarly to that observed experimentally. The small-scale variations of the measured Pareto metric are, however, not reproduced by the simple model used here. This is because the model does not account for self/cross-phase modulation (as seen from the narrower simulated Raman peaks), only includes spontaneous Raman noise and neglects dispersion effects which transform amplitude noise into phase noise. Yet, the wavelength-dependence of the simulated Pareto metric is well reproduced confirming that classical pump noise alone leads to extreme-value fluctuations through cascaded SRS.

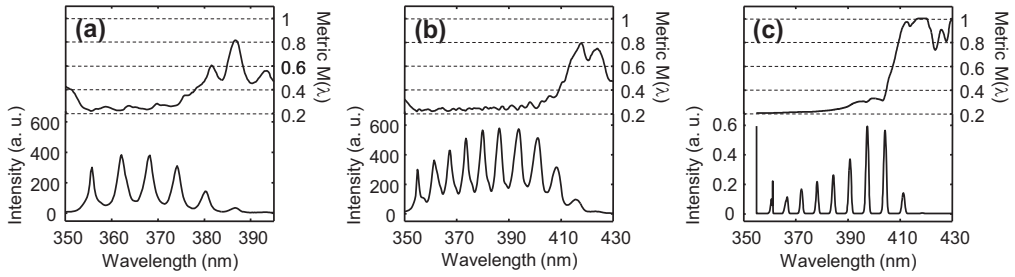

Fig. 5. Mean spectrum (left axis) together with Pareto metric M(λ) (right axis) for (a) low input energy measurement, (b) high energy measurement. (c) Simulated results (see text above for more details).

4. Conclusions

In conclusion, we have experimentally characterized the statistical fluctuations observed in SC generation in the cascaded SRS regime. Quantification of the spectral fluctuations is of high importance for improving the understanding of stability properties of SC generation in this particular regime and the subsequent interpretation of measurements that would employ this type of source. Specifically, we have shown that cascaded SRS can transform classical pump peak power fluctuations into large spectral variations. The statistics of the spectral fluctuations are wavelength-dependent and change from quasi-Gaussian to L-shape form the saturated to unsaturated regime. This constitutes another example of a nonlinear system where initial noise is transformed into extreme-value statistics, complementing other recent studies on extreme-value statistics in nonlinear optical systems.

Acknowledgments

We thank the Academy of Finland (research grants 130099, and 132279).

PAPER II

Incoherent broadband cavity enhanced absorption spectroscopy using supercontinuum and superluminescent diode sources

A. Aalto, G. Genty, T. Laurila, and J. Toivonen

Optics express, vol. 23, no. 19, pp. 25225-25234, 2015.
https://doi.org/10.1364/OE.23.025225

Incoherent broadband cavity enhanced absorption spectroscopy using supercontinuum and superluminescent diode sources

Antti Aalto,[1*] Goëry Genty,[1] Toni Laurila,[2] and Juha Toivonen[1]

[1]*Optics Laboratory, Department of Physics, Tampere University of Technology, FI-33101 Tampere, Finland*
[2]*Metrology Research Institute, Aalto University, FI-02150 Espoo, Finland*
[*]*antti.2.aalto@tut.fi*

Abstract: We investigate incoherent broadband cavity enhanced absorption spectroscopy using a tailored supercontinuum source. By tailoring the supercontinuum spectrum to match the high reflectivity bandwidth of the mirrors, we achieve an unprecedented spectral brightness of more than 7 dBm/nm at wavelengths where the effective absorption path length in the cavity exceeds 40 km. We demonstrate the potential of the source in spectrally broadband measurement of weak overtone transitions of carbon dioxide and methane in the near-infrared 1590 nm – 1700 nm range and evaluate its performance against that of a typical superluminescent diode source. Minimum detectable absorption coefficients (3σ) of 2.2×10^{-9} cm^{-1} and 6.2×10^{-9} cm^{-1} are obtained with the supercontinuum and the superluminescent diode sources, respectively. We further develop a spectral fitting method based on differential optical absorption spectroscopy to fully and properly account for the combined effect of absorption line saturation and limited spectral resolution of the detection. The method allows to cope with high dynamic range of absorption features typical of real-world multi-component measurements.

OCIS codes: (300.0300) Spectroscopy; (300.1030) Absorption; (120.0120) Instrumentation, measurement, and metrology; (320.6629) Supercontinuum generation.

References and links

1. A. O'Keefe and D.A.G. Deacon, "Cavity ring-down optical spectrometer for absorption measurements using pulsed laser sources," Rev. Sci. Instrum. **59**, 2544–2551 (1988).
2. A. O'Keefe, "Integrated cavity output analysis of ultra-weak absorption," Chem. Phys. Lett. **93**(5–6), 331-336 (1998).
3. J. Ye, L. Ma, and J. Hall, "Ultrasensitive detections in atomic and molecular physics: demonstration in molecular overtone spectroscopy," J. Opt. Soc. Am. B **15**, 6–15 (1998).
4. S. M. Ball and R.L. Jones. "Broad-band cavity ring-down spectroscopy," Chem. Rev. **103,** 5239–5262 (2003).
5. B. Bernhardt, A. Ozawa, P. Jacquet, M. Jacquey, Y. Kobayashi, T. Udem, R. Holzwarth, G. Guelachvili, T. W. Hänsch, and N. Picquet, "Cavity-enhanced dual-comb spectroscopy," Nat. Photonics **4**, 55–57 (2009).
6. S. E. Fiedler, A. Hese, and A.A. Ruth, "Incoherent broad-band cavity-enhanced absorption spectroscopy," Chem. Phys. Lett. **371**, 284–294 (2003).
7. T. Wu, Q. Zha, W. Chen, Z. Xu, T. Wang, and X. He, "Development and deployment of a cavity enhanced UV-LED spectrometer for measurements of atmospheric HONO and NO2 in Hong Kong," Atmos. Environ. **95**, 544–551 (2014).
8. P. V. Kelkar, F. Coppinger, A. S. Bhushan, and B. Jalali, "Time-domain optical sensing," Electron. Lett. **35**(19), 1661–1662 (1999).
9. C. F. Kaminski, R. S. Watt, A. D. Elder, J. H. Frank, and J. Hult, "Supercontinuum radiation for applications in chemical sensing and microscopy," Appl. Phys. B **92**, 367–378 (2008).
10. J. M. Langridge, T. Laurila, R. S. Watt, R S. Jones, C. F. Kaminski, and J. Hult, "Cavity enhanced absorption spectroscopy of multiple trace gas species using a supercontinuum radiation source," Opt. Express **16**, 10178–10188 (2008).
11. P. S. Johnston and K. K. Lehmann, "Cavity enhanced absorption spectroscopy using a broadband prism cavity and a supercontinuum source," Opt. Express **16**(19), 15013–15023 (2008).

12. R. S. Watt, T. Laurila, C. F. Kaminski, and J. Hult, "Cavity enhanced spectroscopy of high-temperature H_2O in the near-infrared using a supercontinuum light source," Appl. Spectrosc. **63**(12), 1389–1395 (2009)
13. W. Denzer, G. Hancock, M. Islam, C. E. Langley, R. Peverall, G. A. D. Ritchie, and D. Taylor , "Trace species detection in the near infrared using Fourier transform broadband cavity enhanced absorption spectroscopy: initial studies on potential breath analytes," Analyst **136**(4), 801–806 (2011).
14. W. Denzer, M. L. Hamilton, G. Hancock, M. Islam, C. E. Langley, R. Peverall, and G. A. D. Ritchie, "Near-infrared broad-band cavity enhanced absorption spectroscopy using a superluminescent light emitting diode," Analyst **134**(11), 2220–2223 (2009).
15. J. M. Dudley, G. Genty, and S. Coen, "Supercontinuum generation in photonic crystal fiber," Rev. Mod. Phys. **78**, 1135–1184 (2006).
16. J. M. Dudley, G. Genty, F. Dias, B. Kibler, and N. Akhmediev, "Modulation instability, Akhmediev Breathers and continuous wave supercontinuum generation," Opt. Express **17**, 21497–21508 (2009).
17. M. Triki, P. Cermak, G. Méjean, and D. Romanini, "Cavity-enhanced absorption spectroscopy with a red LED source for NO_x trace analysis," Appl. Phys. B **91**(1), 194–201, (2008).
18. U. Platt and J. Stutz, *Differential Optical Absorption Spectroscopy: Principles and Applications* (Springer, 2008).
19. S. E. Fiedler, A. Hese, and U. Heitmann. "Influence of the cavity parameters on the output intensity in incoherent broadband cavity-enhanced absorption spectroscopy," Rev. Sci. Instrum. **78,** 073104 (2007).
20. U. Platt, J. Meinen, D. Pühler, and T. Leisner, "Broadband Cavity Enhanced Differential Optical Absorption Spectroscopy (CE-DOAS)–applicability and corrections," Atmos. Meas. Tech. **2**(2), (713–723) 2009.
21. L.S. Rothman, I. E. Gordon, A. Barbe, D. C. Benner, P. F. Bernath, M. Birk, ... and J. Vander Auwera "The HITRAN 2008 molecular spectroscopic database," J. Quant. Spectrosc. Radiat. Transfer **110**, 533–572 (2009).
22. S. M. Ball, J. M. Langridge, and R. L. Jones, "Broadband cavity enhanced absorption spectroscopy using light emitting diodes," Chem. Phys. Lett. **398(**1–3), 68–74 (2004).
23. T. Laurila, I. S. Burns, J. Hult, J. H. Miller, and C. F. Kaminski, "A calibration method for broad-bandwidth cavity enhanced absorption spectroscopy performed with supercontinuum radiation," Appl. Phys. B **102(**2), 271–278 (2011).
24. W. R. Simpson, "Continuous wave cavity ring-down spectroscopy applied to in situ detection of dinitrogen pentoxide (N2O5)," Rev. Sci. Instrum **74**, 3442–3452 (2003).
25. J. Morville, D. Romanini, A.A. Kachanov, and M. Chenevier, "Two schemes for trace detection using cavity ringdown spectroscopy," Appl. Phys. B **78**, 465–476 (2004).
26. J. D. Ayers, R. L. Apodaca, W. R. Simpson, and D. S. Baer, "Off-axis cavity ringdown spectroscopy: application to atmospheric nitrate radical detection," Appl. Opt. **44**, 7239–7242 (2005).
27. W. P. Dubé, S. S. Brown, H. D. Osthoff, M. R. Nunley, S. J. Ciciora, M. W. Paris, ... and A. R. Ravishankara, "Aircraft instrument for simultaneous, in situ measurement of NO and NO via pulsed cavity ring-down spectroscopy," Rev. Sci. Instrum. **77**(3), 034101 (2006).

1. Introduction

Cavity ring-down spectroscopy (CRDS) [1], integrated cavity output spectroscopy [2], NICE-OHMS [3], broadband CRDS [4], and cavity-enhanced dual-comb spectroscopy [5] are all spectroscopy techniques which allow for significant increase in sensitivity as compared to direct absorption measurement due to the long optical path in the cavity. These techniques generally require the use of a narrowband continuous wave laser which limits their applicability to single species measurements, or of an optical parametric oscillator system for wavelength scanning, or of a mode-locked laser and a cavity mode matching scheme which increases the complexity and costs.

Incoherent broadband cavity-enhanced absorption spectroscopy (IBB-CEAS) [6] on the other hand offers similar sensitivity and allows for selective multi-component measurement due to the broad bandwidth of the light source. It is simple and robust, which makes it ideal for portable setups, and indeed in-situ measurements of NO_2 and HONO have been recently demonstrated using this technique [7]. One drawback, however, associated with IBB-CEAS is the resulting low total transmittance of the cavity due to the incoherent nature of the light source. This limits the measurement sensitivity by (i) decreasing the signal-to-noise ratio, and (ii) by limiting the maximum value of the mirrors' reflectivity that can be used. Yet, compared to coherent CW methods where the ring-down signal is obtained after momentarily locking the laser source to a cavity mode, IBB-CEAS possesses a higher duty cycle which partly compensates for this disadvantage.

Fiber-based supercontinuum (SC) sources exhibit unique characteristics including very high brightness, broad bandwidth and quasi-perfect spatial coherence, which makes them

attractive candidates for spectroscopic applications [8,9]. Recently, SC sources have been employed in IBB-CEAS measurement setups [10–13]. Yet, the bandwidth of the sources has been filtered significantly to match that of the mirrors' spectral reflectivity, resulting in total intensity of only a few milliwatts. Superluminescent diodes (SLDs) have also been used, as they are more cost-effective and may possess similar brightness [14]. In this work, we demonstrate the potential of cost-effective SC sources tailored for IBB-CEAS in the near-IR. Specifically, we use a compact source with extremely high spectral brightness over the whole high reflectivity bandwidth of the cavity mirrors, which allows us to take full advantage of the IBB-CEAS benefits. The source is built using a cost-effective nanosecond fiber laser pump and a standard single-mode fiber. Compared to previous studies, our SC source has about two orders of magnitude higher spectral brightness. In order to illustrate the advantages of our source over other traditional light sources, we perform a systematic comparison of the SC source performance vs. that of a SLD where the SLD was selected to best match the IBB-CEAS setup.

We further develop a convenient differential optical absorption spectroscopy (DOAS) method for the data analysis that correctly accounts for the saturation of absorption lines in a low-resolution measurement. In contrast to previous approaches, our method is able to cope with a wide range of strong and weak absorption features typical of real-world multi-component measurements, leading to a greatly enhanced detection dynamic range. This customized DOAS-method is then used in both, calibration of the instrument as well as the retrieval of trace gas concentrations from the measurement samples. Combined with our DOAS method, we demonstrate that our SC source results in a significantly enhanced sensitivity and bandwidth compared to the SLD.

2. Experimental setup

To generate the supercontinuum, we inject 700-ps-pulses from an ultra-compact fiber laser (Keopsys Kult) operating at 1.5 μm into the anomalous dispersion regime of a standard single-mode fiber (Ocean UltraWave SLA). The result is a broadband supercontinuum with more than 250 nm total bandwidth extending from 1500 nm to beyond 1750 nm (the limit of our spectrum analyzer) with a total output power of 800 mW. Figure 1(a) shows the output spectrum of the SC source for different values of input pulses peak power. In the anomalous dispersion and long pump pulse regime, SC generation is dominated by noise-seeded modulation instability and soliton dynamics [15]. These processes are clearly evident in Fig. 1(a); as the pump peak power is increased, the spectral intensity of the symmetrical sidebands around the pump resulting from modulation instability increases. In the time domain, this corresponds to a random modulation that develops on top of the pulse envelope. This process eventually breaks the long input pulse into a random train of breathers that evolve into short solitons as a result of higher-order dispersion and stimulated Raman scattering [16]. The solitons experience the soliton self-frequency shift, resulting in efficient energy transfer from the pump towards the long wavelengths. We note that although the spectrum of the SC generated in this way fluctuates heavily from pulse to pulse, the average spectrum is remarkably stable when using a high repetition rate laser. The sharp peak at the pump wavelength corresponds to the remaining background of the pulse envelope in the time domain (mostly at the leading and trailing edges where the intensity is too low for breathers to emerge). This spectral peak is typical for a SC generated with long pump pulses and may cause problems in specific applications. In particular, the coherent laser peak may momentarily lock to the IBB-CEAS cavity modes through optical feedback, causing high intensity transmission through the cavity at the laser pump wavelength and resulting in significant stray light noise in the spectrometer.

The SLD source on the other hand produces 17 mW of average power with a spectral bandwidth (FWHM) of 43 nm. A direct comparison between the SLD and SC spectra [see Fig. 1(b)] clearly illustrates the advantage of using the SC source for broadband spectroscopy with a power-bandwidth product more than 300 times that of the SLD. The SC spectrum also matches the overall spectral shape of the mirrors' reflectivity but does not significantly exceed

their usable bandwidth. This contrasts with previous approaches using SC sources where an extremely broadband source was filtered to match the mirrors' reflectance spectrum and using only a tiny fraction of the available optical power.

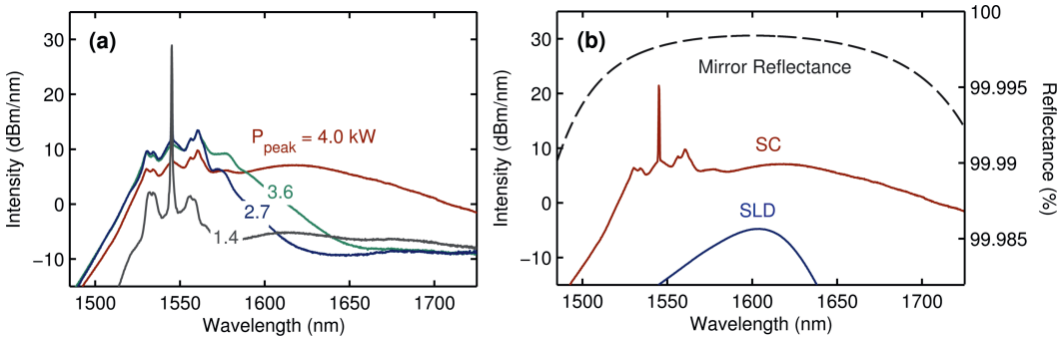

Fig. 1. (a) Supercontinuum spectrum as a function of pulse peak power. (b) Comparison of supercontinuum (SC) and superluminescend diode (SLD) spectra together with the mirror reflectance curve. The reflectance is calculated from the transmittance curve measured by the manufacturer assuming zero losses.

The experimental IBB-CEAS setup is illustrated in Fig. 2. Light from the SC is first collimated using a fiber collimator (D = 3.0 mm) and then slightly focused into a 1.17 meters long near-confocal cavity containing the trace gas sample using a plano-convex lens (f = 750 mm). The mirrors (Layertec 102103) have a radius of curvature of 1 m with a reflectivity exceeding 99.99 % between 1520 nm and 1670 nm. Such high reflectivity results in an effective path length exceeding 10 km, but the average transmission of the cavity is less than 0.5×10^{-4}, i.e. half of the transmission of a single mirror [17]. The maximum intensity of the SC spectrum corresponds to the maximum of the mirrors' reflectivity, thus corresponding to the wavelength of minimum transmission. This is particularly important as it allows to significantly increase the signal-to-noise ratio. Light exiting the output mirror of the cavity is coupled into a multi-mode fiber and the absorption spectrum is recorded using an optical spectrum analyzer (Ando AQ6315B) with a 0.1 nm resolution and integration time of 0.5 s, resulting in a scanning speed of c.a. 10 nm/min.

The cavity is airtight with valves for gas input and output, and the construction allows for easy angular adjustment of the mirrors. A visible He-Ne-laser is used for initial alignment of the cavity. We then switch to the SC or SLD source and adjust the mirrors' alignment to maximize the total transmission. The slightly non-confocal geometry of the cavity results in a quasi-continuous transverse mode-structure. To further average out the mode structure, and to prevent mode-locking effects resulting from optical feedback into the laser, the output cavity mirror is vibrated mechanically at 620 Hz. In the case of the SC source, a slight misalignment of the cavity is used to suppress any remaining mode-locking. All of the results presented here were measured using a small constant gas flow. The cavity was purged using N_2 flow between measurements.

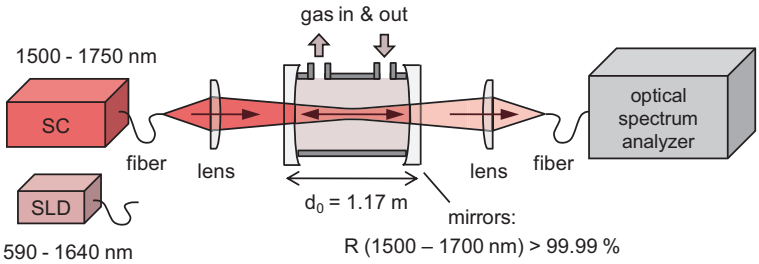

Fig. 2. Experimental setup. Light from the supercontinuum (SC) or superluminescent diode (SLD) source is collimated and focused into a cavity containing the gas sample. Light leaking through the output mirror is focused into a multi-mode fiber, which is connected to an optical spectrum analyzer.

3. DOAS analysis of IBB-CEAS data

Broadband measurement has many benefits beyond the obvious potential for multi-component analysis. However, retrieving accurately concentrations from broadband spectral data is a nontrivial task. Arguably, the most advanced method of broadband trace gas analysis is differential optical absorption spectroscopy (DOAS), originally developed for long-range atmospheric measurements [18]. In DOAS, a modeled differential absorption spectrum is fitted to the experimental spectrum using a least squares method. The concentrations are then retrieved as the fitting parameters. Because of its ability to reliably retrieve concentrations even in the presence of overlapping background absorbers, this method can be very useful in the measurement of large molecules such as many volatile organic compounds which have broad and smooth absorption spectra. When measuring smaller molecules, an important benefit is the ability to separate the absorption of molecules (which varies rapidly as a function of wavelength) from the smoothly varying background signal caused by e.g. aerosol extinction and system drifts. This can be achieved by high pass filtering the spectrum or by including a low-order polynomial in the fit. In order to use a DOAS based fitting method in IBB-CEAS, a model is required for cavity enhancement of broadband spectra. The model should account for the wavelength-dependent mirror spectral reflectivity, possible system drifts, and the instrument resolution.

The theory of cavity-enhancement for incoherent sources is well known. Originally derived in the time-domain [6], the same result can be obtained using a more intuitive frequency-domain approach [13]. Yet, the results derived in [6,17], when used in the context of IBB-CEAS [10–14] require modification for proper implementation of the limited spectrometer resolution. The results in [6,17] are given for the absorption coefficient and this has generally led authors to implement the resolution by convolving the absorption cross section with the instrument slit function, which is unphysical because the resolution affects the measured transmittance spectrum and not the properties of the sample. Accounting for the spectrometer resolution in this way can then lead to significant distortions in the measured spectrum of gas with strong and narrow absorption features that saturate in the cavity, since the saturation effect is now underestimated in the model. On the other hand, modeling accurately the limited spectrometer resolution is especially important because (i) saturation occurs in a regime where the cavity enhancement of the SNR is largest, (i.e. where the single pass absorption losses are comparable to mirror losses [19]), and (ii) the spectral resolution is typically a limiting factor when building a compact and cost-effective instrument making best use of the simplicity and robustness of IBB-CEAS technique. When the spectral resolution is properly accounted for in the model, the dynamic range of the detection can be greatly increased due to the fact that the weaker absorption features still provide information when the stronger lines are saturated. This will also reduce the error caused by strong saturated background absorbers such as water vapor. Similar complications affecting broadband CRDS spectra have been discussed in detail previously, together with a method for proper analysis of the affected spectra [4]. Here, we develop a specific model for IBB-CEAS that correctly accounts for the absorption line saturation and limited spectrometer resolution. The model can be used with a least squares method fitting procedure to retrieve concentrations (or other parameters) from measured spectra using DOAS principles.

The saturation of absorption lines is explicitly discussed in the context of IBB-CEAS in [20]. We start from the intermediate result given in Eq. (26) in [20] that considers the integrated “cavity enhanced differential transmittance”:

$$\frac{I(\lambda)}{I_0(\lambda)} = \frac{\rho(\lambda)}{\rho(\lambda)+\tau(\lambda)}, \tag{1}$$

where $I(\lambda)$ and $I_0(\lambda)$ are the output intensities in the presence and absence of absorbing species, respectively. The term $\rho(\lambda)$ represents the mirror losses (dominated by the mirror transmission, assuming high quality mirrors). Using this notation, the mirror reflectance is given by $R(\lambda) = 1 - \rho(\lambda)$. The wavelength-dependent term $\tau(\lambda)$ is the small single-pass gas

absorption given by the linear approximation of Beer-Lambert law, where transmittance of the sample gas sample can be written as $T(\lambda) = 1 - \tau(\lambda)$, and

$$\tau(\lambda) = \sum_j \sigma(\lambda)_j N_j d_0, \quad (2)$$

where $\sigma(\lambda)_j$ are the absorption cross sections of the gas species, N_j their number densities and d_0 is the cavity length. We model the measured transmittance in the presence of gas sample by convolving the cavity transmittance with an instrument slit function $g(\lambda)$. It is important to take the instrument resolution into account at this step, since it directly affects the transmittance spectrum. The optical density is then given as the inverse of the natural logarithm of the transmittance. Finally, we add a low degree polynomial (3rd degree typically is enough) to take into account background effects such as smoothly varying absorbers, aerosol extinction and system drifts. We arrive at the following equation for modeled optical density:

$$D_{fit}(\lambda) = -\ln\left(\frac{\rho(\lambda)}{\rho(\lambda) + \sum_j \sigma(\lambda)_j N_j d_0} * g(\lambda) \right) + \sum_k a_k \lambda^k, \quad (3)$$

where the number densities N_j and polynomial coefficients a_k are used as fitting parameters. The absorption cross sections $\sigma_j(\lambda)$ can be modeled beforehand using a spectral database, e.g. HITRAN 2008 [21], and well-known line broadening mechanisms.

4. Instrument calibration

In order to calibrate the instrument and retrieve concentrations from DOAS fits, mirror losses $\rho(\lambda)$ need to be characterized. Using a reference sample is the most common approach but a ring-down measurement using a diode laser [22] and broadband phase-shift CRDS [23] have also been employed. It is important to note that the total losses not only depend on the properties of the mirrors, but also on the coupling parameters and alignment of the cavity. Therefore, using a separate source such as in [22] may not allow to determine accurately the mirror losses. Here, we therefore use a reference sample to calibrate the instrument. More specifically, we measure the optical density spectrum from a sample of known concentration, then use a Levenberg-Marguardt algorithm to fit Eq. (3) to the measured spectrum with $\rho(\lambda)$ containing the fitting parameter. As a starting point for $\rho(\lambda)$, we use the mirror transmittance provided by manufacturer and add a small constant fitting parameter independent of wavelength to represent additional losses such that $\rho(\lambda) = \rho(\lambda)_{trans} + \epsilon$. This correction parameter ϵ is then the retrieved from the least squares fit. We note that a more accurate broadband calibration is also possible with this method, since the constant ϵ can be replaced with a curve $\epsilon(\lambda)$, for example a low degree polynomial, whose coefficients then act as the calibration parameters. Doing so could in principle increase the accuracy of the calibration at wavelengths away from the center wavelength, provided the reference sample has absorption features covering the whole high reflectivity bandwidth of the mirrors. This would result in a smoothly-varying calibration curve for the mirror losses as function of wavelength, similarly to what can be obtained using a point-by-point calibration approach [23].

Due to the different cavity alignment in each case, characterization of the mirror losses was performed separately for both the SC and SLD light sources using a reference sample of 100 ppm CO_2 and whose weak $3\nu_1 + \nu_3$ combination overtone transitions are at the center of the mirror bandwidth in the 1595 nm – 1620 nm range. The absorption cross-section $\sigma(\lambda)$ was modeled using the HITRAN 2008 database [21] and by applying the appropriate Voigt broadening of the lines at the measurement temperature and pressure. By fitting the modeled optical density spectrum to the experimentally recorded spectrum, we obtained a mirror loss parameter $\epsilon = 12.1 \times 10^{-6}$ for the SC source and $\epsilon = 8.8 \times 10^{-6}$ for the SLD source, respectively. The discrepancy arises from the fact that when employing the SC source, the cavity was intentionally slightly misaligned to prevent mode-locking effects resulting from optical feedback. The corresponding maximum effective path lengths were also calculated for

reference. The maximum effective path length is solely determined by the average lifetime of the photons in the cavity and depends on the mirror losses and cavity length [6]. Using a value $\rho(\lambda_0)_{trans} = 16 \times 10^{-6}$ for the minimum center bandwidth transmission losses (measured by the manufacturer) and the correction parameters ϵ given above, we estimate the maximum effective path lengths to be 40 km and 46 km for the SC and SLD source, respectively.

5. Results and discussion

The performance of the calibrated instrument with the SC and SLD sources was evaluated by measuring the concentration of CO_2 and CH_4 samples whose weak $3v_1 + v_3$ combination overtone and $2v_3$ overtone transitions, respectively, fall within the measurement bandwidth of the setup. We first measured the absorption spectrum of CO_2 with 200 ppm concentration. Figure 3 shows the experimental optical density spectrum measured using the SC source (red solid line). The result of the least squares fit using Eq. (3) is superimposed (blue solid line), in excellent agreement with the measured spectrum. A concentration of 194 ppm was retrieved from the fit. The experiment was subsequently repeated using the SLD source. The results (not shown here) are very similar to those obtained with the SC source except for a slightly noisier spectrum. In the case of the SLD source, a concentration of 196 ppm was retrieved from the fit. We note that in this regime of relatively high optical density and limited spectrometer resolution, applying the usual methodology [10–14] of implementing the spectrometer resolution in the model resulted in significant distortion of the modeled spectrum, causing a large error in the retrieved concentration.

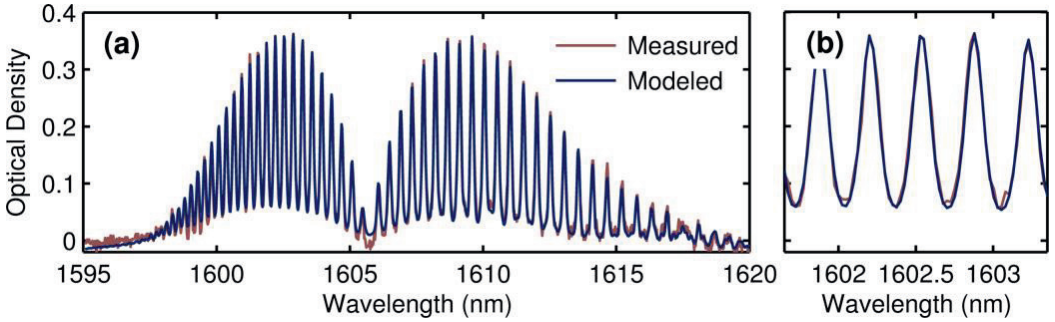

Fig. 3. (a) Experimental CO_2 absorption spectrum measured using the SC source from a sample containing 200 ppm of CO_2 (red) together with the modeled least squares fit (blue). Concentration of 194 ppm was retrieved from the fit. (b) Close-up of the fit, highlighting the excellent agreement between measured and modeled spectra.

In order to evaluate the performance in lower SNR conditions, we subsequently characterized a CO_2 sample with a lower concentration of 40 ppm. Figure 4 shows the experimentally recorded absorption spectra measured with the SC source [Fig. 4(a)] and the SLD source [Fig. 4(b)]. We can see how in this case the significantly lower brightness of the SLD source results in a much more noisy spectrum. There is also a noticeable baseline shift in both spectra, caused by system drifts including light source intensity and cavity coupling variations that can occur in-between and during the recording of the I and I_0 signals. Broadband DOAS spectral fitting methods are, however, rather effective in retrieving concentrations even in cases where the spectrum appears noisy and shows baseline drifts. By fitting Eq. (3) to the spectra of Fig. 4, concentrations of 38 ppm and 45 ppm were retrieved for the SC and SLD measurements, respectively. The error is larger in the SLD case as can be expected from the excess of noise. Nevertheless, in both cases, including the compensation for the baseline drift that was accounted for by the low-degree polynomial in Eq. (3), the modeled spectra showed good agreement with the measured spectra.

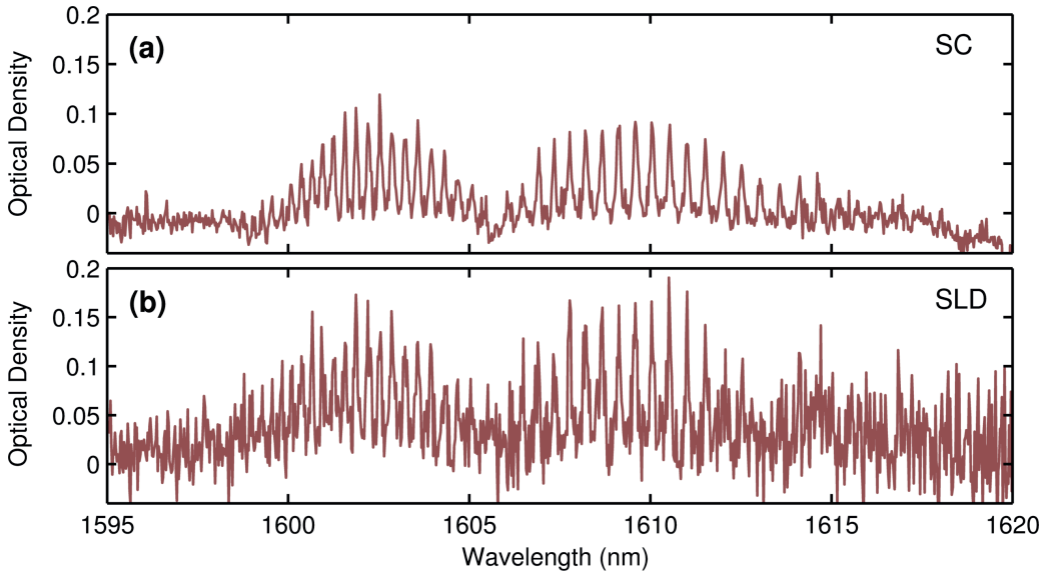

Fig. 4. Experimental CO_2 absorption spectrum measured from concentration of 40 ppm using (a) supercontinuum (SC) and (b) superluminescent diode (SLD) source. Concentrations of (a) 38 ppm and (b) 45 ppm were retrieved using DOAS fits.

We then evaluated the detection limit of the instrument for CO_2. For this purpose, we repeatedly measured the CO_2 concentration from the cavity when flushed with dry nitrogen, such that no CO_2 was actually present. For both light sources the background spectrum was scanned 67 times and 66 I/I_0 pairs were formed from the consecutive signals. We note that determining the detection limit by scanning I_0 and I spectra immediately one after another does not take into account the time needed to fill the cavity with the gas sample. However, we believe that this is not a major issue, since instrument drifts are effectively compensated by the polynomial in Eq. 3. Although the optical density spectra calculated from the 66 pairs showed no sign of trace gas absorption, the CO_2 absorption spectrum was nevertheless fitted to the measured spectra. Histograms of retrieved concentrations showed Gaussian distributions around zero concentration with standard deviations of 0.41 ppm for the SC source and 1.12 ppm for the SLD source. From these values, we can define the 3σ detection limits for CO_2 as 1.2 ppm and 3.4 ppm for the SC and SLD source, respectively, with a scanning time of 2.5 minutes. The factor of three difference in the detection limits is somewhat surprising given that the SC has roughly ten times more spectral brightness at the CO_2 measurement bandwidth. This would be the expected result if the detection was shot-noise limited, but because we are measuring weak signals that are also affected by the thermal noise of the detector, one might expect a larger benefit from the increased brightness. We attribute this discrepancy mainly to the complications caused by the slight misalignment of the cavity to decrease the unwanted effects of optical feedback. This intentional misalignment caused a 13 % reduction in the effective path length as well as a reduction in the effective transmission of the cavity, which contribute to decreasing the sensitivity enhancement in the SC case. There is also possibly small amplitude noise in the SC spectrum caused by residual optical feedback. The misalignment could be avoided by using an optical isolator or a spectral filter to suppress the optical feedback at the pump laser wavelength, which could improve the sensitivity. Finally, we note that evaluating the measurement stability for both sources by means of Allan variance analysis is an important task, best performed using a faster detection scheme, such as e.g. a detector array, and it is left here as a subject of future work. Here, the scanning speed of 10 nm/min was approximated to be a good compromise between minimizing detection noise and system drifts.

The detection limits can be generalized by calculating the minimum detectable absorption coefficients for equivalent single-wavelength measurements done using the strongest line in

the spectrum. In the $3\nu_1 + \nu_3$ band, the strongest line has an absorption cross section of 7.56×10^{-23} cm^2. By using this value for absorption cross section and by assuming that detection limits of 0.41 ppm and 1.22 ppm were achieved in hypothetical single-wavelength measurements using this line only, we calculate the minimum detectable absorption coefficients (3σ) of 2.2×10^{-9} cm^{-1} for the SC source, and 6.2×10^{-9} cm^{-1} for the SLD with a measurement time of 2.5 minutes. For convenience, the optical parameters and performance of both sources are summarized in Table 1.

Table 1. Optical parameters and performance of SC and SLD sources

	Supercontinuum	Superluminescent diode
Center wavelength (nm)	1598	1604
-3dB bandwidth[a] (nm)	142	55
Average power (mW)	800	17
Max. spectral brightness[b] (dBm/nm)	7.1	-4.7
Maximum path length (km)	40	46
CO_2 detection limit (ppm)	1.2	3.4
MDA[c] (10^{-9} cm^{-1})	2.2	6.2

[a,b]Ignoring the peaks around 1545 nm in SC spectrum. [c]Minimum detectable absorption coefficient.

The sensitivity of our measurements is comparable to that reported in [10] and [13]. The fact that the achieved sensitivity with our SC source is similar might be surprising at first sight, given that our SC source has roughly two orders of magnitude higher spectral brightness. However, these previous studies used detection schemes with a silicon CCD and an FTIR spectrometer, respectively, which allow to collect light much more efficiently than the scanning optical spectrum analyzer employed here. Yet, we anticipate that with a CCD or FTIR, our approach would allow for a significantly better sensitivity.

Besides providing a better sensitivity in the measurement due to its higher spectral brightness, the SC source has the additional benefit of a much broader bandwidth. We demonstrated the broadband potential of the SC source by measuring the absorption spectrum of methane that is over 80 nm wide and covers a large fraction of the mirrors' high reflectivity (R > 99.995 %) bandwidth. This could not be performed with the SLD source due to its limited bandwidth (see Fig. 1). The results for a sample with a nominal concentration of 4 ppm are shown in Fig. 5. The DOAS fit (not shown) using the same procedure as with CO_2 is in good agreement with the measurements and produces a concentration value of 3.2 ppm. The value differs by 20% from the nominal concentration, which is more than what could be expected. We attribute this discrepancy to two factors: the nonlinearity of the optical scanning spectrometer at wavelength ranges near the edge of its operational bandwidth at 1750 nm and the fact that the mirror loss calibration was performed using only a wavelength-independent correction parameter near the center of their spectral bandwidth. The latter issue could be addressed by using higher-order correction parameters as discussed in Section 3.

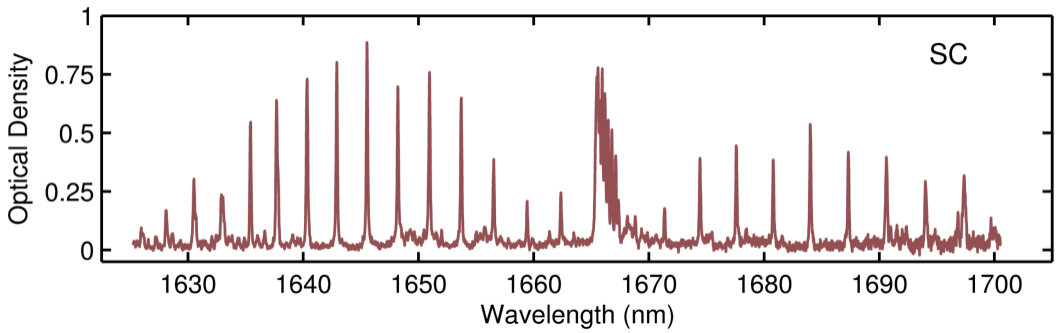

Fig. 5. Experimental broadband CH_4 absorption spectrum measured from a concentration of 4 ppm using a supercontinuum source. Concentration of 3.2 ppm was retrieved from the DOAS fit.

The IBB-CEAS setup presented here could be improved upon in a variety of ways. Firstly, replacing the scanning spectrometer with a detector array could greatly increase the SNR and thus the sensitivity through a higher duty cycle. This would also decrease the cost of the setup and make it more portable. In this case, the lower resolution would make the data analysis methods presented here even more crucial. Secondly, optimizing the cavity and coupling parameters according to guidelines given in [19] and suppressing optical feedback through the use of an optical isolator or spectral filters could increase the optical throughput and SNR even more. Using higher-order correction parameters in the mirror loss calibration would also improve the accuracy of the instrument. Finally, the measurement bandwidth could be further increased by using a prism cavity [11].

6. Conclusions

In conclusion, we have demonstrated incoherent broadband cavity-enhanced absorption spectroscopy using a tailored fiber-based supercontinuum source and very high reflectivity mirrors in the near-IR. Upon systematic comparison with a superluminescent diode source, the supercontinuum was shown to offer better sensitivity and much broader usable bandwidth. The minimum detectable absorption coefficients (3σ) were 2.2×10^{-9} cm^{-1} for the SC source and 6.2×10^{-9} cm^{-1} for the SLD source with a scanning time of 2.5 minutes. For both sources, the sensitivity is higher than what has been typically demonstrated for broadband CRDS [4] and does not fall greatly behind the most advanced single-wavelength CRDS methods where the minimum detectable absorption coefficients are of the order of 10^{-11} cm^{-1} – 10^{-10} cm^{-1} [24–27]. Compared to single-wavelength methods, IBB-CEAS has better selectivity, flexibility, and true potential for multi-component analysis. We have also developed and demonstrated a DOAS-type method for data analysis that that correctly accounts for the saturation of absorption lines in a low-resolution measurement, which is crucial for real-world high dynamic range multi-component detection. Finally, we note that extending the technique to mid-infrared wavelengths offers exciting possibilities for ultra-sensitive multi-component measurements in the molecular functional group region, where strong absorption bands associated with fundamental vibrational transitions can be used.

Acknowledgments

This work was conducted in the MMEA research program of the Cluster for Energy and Environment (CLEEN Ltd.), funded by Tekes – the Finnish Funding Agency for Innovation. In addition, Toni Laurila acknowledges the financial support from the Academy of Finland.

PAPER III

Cavity enhanced absorption spectroscopy in the mid-infrared using a supercontinuum source

C. Amiot, A. Aalto, P. Ryczkowski, J. Toivonen, and G. Genty

Applied Physics Letters, vol 111, no. 6, p. 061103, 2017.
https://doi.org/10.1063/1.4985263

Cavity enhanced absorption spectroscopy in the mid-infrared using a supercontinuum source

Caroline Amiot,[1,2,a)] Antti Aalto,[1] Piotr Ryczkowski,[1] Juha Toivonen,[1] and Goëry Genty[1]
[1]*Optics Laboratory, Physics Department, Tampere University of Technology, P.O. Box 692, FI-33101 Tampere, Finland*
[2]*Institut FEMTO-ST, UMR 6174 CNRS-Université Bourgogne Franche-Comté, 15B avenue des Montboucons, 25030 Besançon Cedex, France*

(Received 29 May 2017; accepted 23 July 2017; published online 8 August 2017)

We demonstrate incoherent broadband cavity enhanced absorption spectroscopy in the mid-infrared wavelength range from 3000 to 3450 nm using an all-fiber based supercontinuum source. Multi-component gas detection is performed, and the concentrations of acetylene and methane are retrieved with sub-ppm accuracy. A linear response to nominal gas concentrations is observed, demonstrating the feasibility of the method for sensing applications. *Published by AIP Publishing.*
[http://dx.doi.org/10.1063/1.4985263]

Gas detection and accurate concentration measurements are important in many fields ranging from the industrial process to emission control and pollution monitoring. Different spectroscopic methods have been developed to retrieve gas concentrations with very high accuracy, including cavity ring down spectroscopy[1,2] and its broadband implementation,[3] integrated cavity output spectroscopy,[4] noise-immune cavity-enhanced optical-heterodyne molecular spectroscopy,[5] and cavity enhanced absorption spectroscopy (CEAS).[6,7] Each of these methods presents advantages and drawbacks in terms of sensitivity, selectivity, footprint, and cost.

Cavity enhanced absorption spectroscopy is conceptually relatively simple, and a robust experimental setup can be implemented from off-the-shelf components. In CEAS, one uses a highly reflective cavity to increase significantly the optical path and thus the interaction length between the light beam and gas molecules, which leads to enhanced sensitivity. However, because of the mirrors' highly reflectivity, the light intensity at the cavity output is dramatically reduced such that a detector with high sensitivity is generally required to measure the absorption. CEAS can be selective for a particular gas absorption line if a source with a narrow linewidth is used, or it can also perform multi-component detection when a light source with a broad spectrum is employed.

The recent development of light sources operating in the mid-infrared has recently allowed to extend precise spectroscopic measurements to the molecular fingerprint region where many gases possess strong absorption lines, and indeed, several studies have reported measurements from pure gas in the 3–5 μm region.[8–12] All these recent studies used optical parametric oscillators based on difference-frequency generation or a quantum cascade laser. While some of the recent demonstrations allow for extreme sensitivity, the light source is single species specific, which may limit the usability. The development of broadband supercontinuum sources[13] on the other hand has revolutionized many applications ranging from frequency metrology to imaging and spectroscopy. Recently, supercontinuum (SC) has been shown to be particularly adapted to perform broadband CEAS in the near infrared.[14,15]

Here, taking advantage of the high spatial coherence and high brightness of this type of source, we demonstrate multi-components gas detection in the mid-infrared over a bandwidth as large as 450 nm using incoherent broadband cavity enhanced absorption spectroscopy. These results are significant not only because they illustrate the potential of incoherent supercontinuum sources for spectroscopy in the mid-IR but also because they represent the largest continuous detection window for gas reported using the CEAS method.

An all-fiber supercontinuum source with a spectrum spanning from 900 to 3700 nm was developed using a 1547 nm gain-switched pump laser producing 10 kW peak power sub-nanosecond pulses at a repetition rate of 100 kHz. The pulses are first injected into the anomalous dispersion regime of a 4 m long step-index, silica non-zero dispersion shifted fiber (DSF) with 9 μm core-diameter. The zero dispersion wavelength (ZDW) of the fiber is at 1510 nm, allowing for efficient noise-seeded modulation instability dynamics which breaks up the long pump pulses into a large number of solitons with a short duration.[16] The solitons experience the Raman self-frequency shift which expands the spectrum towards the long wavelengths up to 2400 nm, which is the transparency window limit of silica. The output of the DSF is then directly connected to a 7-m step-index fluoride (ZBLAN) fiber with low attenuation ($<$0.1 dB/m) up to c.a. 4 μm. The core size of the ZBLAN fiber is comparable to that of the DSF, which minimizes the coupling losses. Because a significant fraction of the spectral intensity after the DSF is located in the anomalous dispersion regime of the ZBLAN ($ZDW_{ZBLAN} = 1620$ nm), the short solitons undergo additional Raman self-frequency shift extending the supercontinuum spectrum up to 3700 nm with an average output power of 160 mW. The resulting SC spectrum illustrated in Fig. 1 is essentially spectrally incoherent with large fluctuations from pulse to pulse. Yet, the average spectrum is highly stable, a pre-requisite in the context of spectroscopic measurements.

a)caroline.amiot@tut.fi

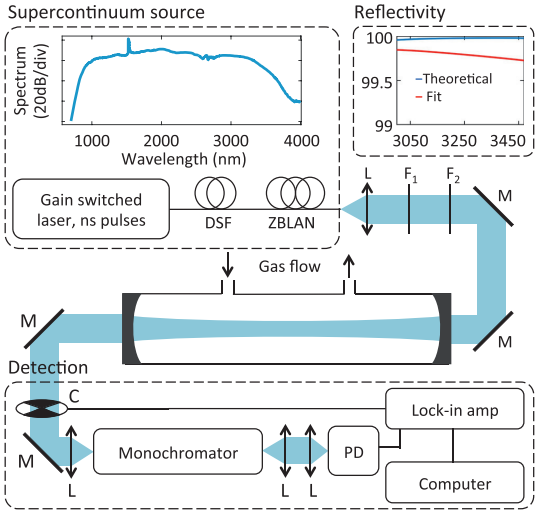

FIG. 1. Experimental setup. DSF: dispersion-shifted fiber, ZBLAN: fluoride fiber, L: lens, $F_{1/2}$: filter, M: mirror, C: mechanical chopper, and PD: photodetector. The top part of the figure shows the measured SC spectrum at the ZBLAN fiber output. The inset to the right compares the modelled mirrors reflectivity as provided by the manufacturer (blue line) with the fitted reflectivity from the experimental measurements (red line).

The all-fiber SC source was subsequently used to perform cavity-enhanced absorption spectroscopy measurements. The experimental setup is illustrated in Fig. 1. The SC beam is collimated to a 3 mm size using an aspheric lens coated for the 3–5 μm range. The beam propagates through a 1-m long confocal cavity constructed from an aluminium pipe and closed by two mirrors with 1 m radius of curvature and a high reflection coefficient ($R > 99.95$) between 3000 and 3450 nm. The SC power corresponding to the cavity spectral bandwidth is 4 mW. The high reflectivity of the mirrors results in a transmission of 2.5×10^{-4} and an effective path length of c.a. 300 m. In order to match the supercontinuum source spectrum with the spectral bandwidth of the cavity, the short wavelength components of the SC are filtered out using two long-pass filters F_1 and F_2 with cut-off wavelengths at 2333 nm and 2998 nm, respectively. The cavity has valves in both ends, allowing gas circulation with a constant flow during the measurements. Gas samples were diluted from 0.5 ppm of C_2H_2 and 0.25 ppm of CH_4 in nitrogen using mass flow controllers (5850S, Brooks Instrument). Using an uncoated MgF_2 lens with a focal length of 50 mm, the beam at the cavity output is focused onto the entrance slit of a computer-controlled monochromator (HR550 Horiba) with 300 grooves/mm grating, and the light intensity is detected with a liquid nitrogen-cooled InAs photodetector (Judson J10D). Wavelength scanning is performed in steps of 0.5 nm. Because only a small fraction of the 4 mW SC power is transmitted through the highly reflective cavity, we use lock-in detection (Lock-in amplifier + mechanical chopper at 245 kHz) and an integration time of 1 s to improve the signal-to-noise ratio.

We next perform measurements of different gases using the differential optical absorption spectroscopy (DOAS) method performed in sequential steps.[15] The spectral transmission of the cavity is first calibrated by a reference measurement with only N_2 flowing through the cavity such that no absorption is present. A second measurement is subsequently performed with the gas under study, and the spectral transmission from the cavity is then compared to that of the reference measurement

$$\frac{I(\lambda)}{I_0(\lambda)} = \frac{\rho(\lambda)}{\rho(\lambda) + \tau(\lambda)}, \tag{1}$$

where $I(\lambda)$ and $I_0(\lambda)$ correspond to the spectral intensities recorded for the gas under study and N_2 in the cavity, respectively. The parameter ρ represents the mirror spectral losses, and τ is the small single-pass absorption through the cavity of length d_0 and depends on the absorption cross section $\sigma(\lambda)_j$ and number density N_j of the gas species j present in the cavity as

$$\tau(\lambda) = \sum_j \sigma(\lambda)_j N_j d_0. \tag{2}$$

Retrieval of the gas species concentration is then achieved by fitting the experimentally measured ratio $I(\lambda)/I_0(\lambda)$ with Eqs. (1) and (2) using a least-square method. In the fitting procedure, we use the HITRAN 2012 database for absorption line strengths and apply the appropriate Voigt broadening of the lines at the measurement temperature and pressure. The model also accounts for the finite resolution of the monochromator and slit width, as well as for possible background drift caused, e.g., by light intensity or cavity coupling fluctuations during the measurement.[15]

One particular feature of broadband DOAS is its ability to retrieve accurately gas concentrations even when the signal-to-noise ratio is relatively low and the recorded absorption spectra are noisy. This arises from the fact that spectral fitting is performed over a large number of absorption lines, which effectively increases the integration time and thus reduces the noise.

The experimental setup is first calibrated by measuring the spectrum of a reference gas sample of known concentration, using only the monochromator resolution and mirror losses as free-running parameters. This allows us to determine precisely the spectral dependence of the mirrors' losses $\rho(\lambda)$, which slightly differs from the simulated data based on the mirrors' layer structure and provided by the manufacturer (see the inset in Fig. 1). Figure 2 shows the comparison between the fitted and measured absorption lines of acetylene [Fig. 2(a)] and methane [Fig. 2(b)] for nominal concentrations of 4 ppm and 5 ppm, respectively, and we can see excellent agreement between the DOAS measurement and the fit. The actual measurement resolution was found to be 1 nm, which is in agreement with the targeted resolution using the monochromator slits of 100 μm.

The calibrated instrument is then used to determine the response of the method by repeating the measurement for different gas concentrations and using the concentration as a free-running parameter in the fitting procedure. Figure 3 shows the results of the fit against the nominal gas concentrations set using the mass flow controllers. Linear responses

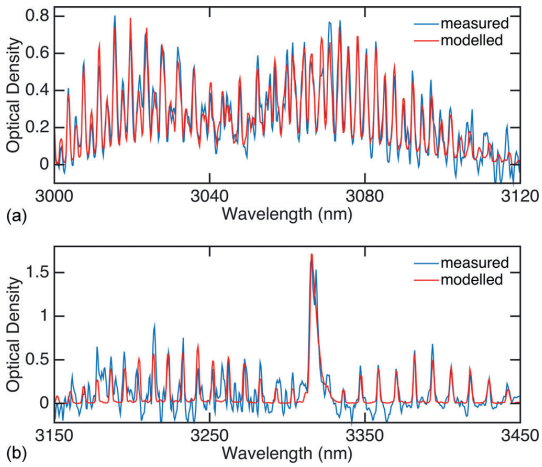

FIG. 2. Comparison between the modelled (red line) and the measured (blue line) absorption spectra of 5 ppm of acetylene (from 3000 to 3100 nm) and 4 ppm of methane (from 3150 to 3450 nm). Note that negative values in the measured optical density result from the detection noise.

are found for both gases, demonstrating the feasibility of the method for sensing applications. The smallest concentrations of 0.5 ppm for acetylene and 0.25 ppm for methane are still following the linear response function.

One major advantage of CEAS over other spectroscopic techniques is the possibility to perform detection over a very broad bandwidth. We next exploited this potential to demonstrate multi-component gas analysis over the full bandwidth of the cavity from 3000 to 3450 nm. For this purpose, both methane and acetylene were flown simultaneously through the cavity with nominal concentrations of 5 and 2 ppm, respectively. The results in Fig. 4 show very good agreement between the measured and modelled absorption using the nominal concentrations over the full 450 nm bandwidth. For the modelled absorption, only the low-order polynomial was

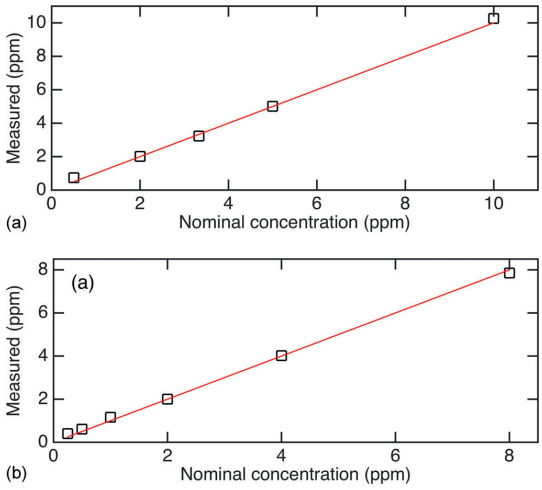

FIG. 3. Measured vs. nominal concentration for (a) acetylene and (b) methane.

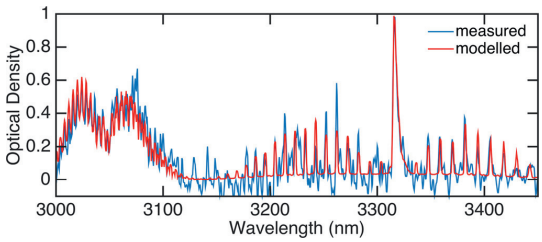

FIG. 4. Simultaneous multi-component detection of 5 ppm of acetylene (from 3000 to 3150 nm) and 2 ppm of methane (from 3150 to 3450 nm). The blue and red lines illustrate the measured and modelled spectra, respectively. Note that negative values in the measured optical density result from the detection noise.

used as a free running parameter to account for possible drift during the long measurement time. The present experiments have been performed with pure gas samples in a cavity flushed with N_2. From a more practical application viewpoint, it would be desirable to perform similar measurements but in the presence of air, especially because water absorption lines are present in the particular wavelength range used here for the detection. Numerical simulations based on the setup parameters indicate that several absorption lines of acetylene and methane do not overlap with those of water, and thus, it should be possible to retrieve the gas concentrations by taking the water peaks into account in the fitting procedure. Furthermore, enhanced spectral resolution in the detection and reduced pressure in the gas cell would yield better separation of different gas components.

In conclusion, using an all-fiber supercontinuum source, we have demonstrated for the first time CEAS in the mid-infrared over a wavelength range as large as 450 nm, allowing us to retrieve gas concentrations with sub-ppm accuracy. The sensitivity and measurement speed of the technique could be improved in various ways. The intensity of the light source could be increased, e.g., by fusion-splicing the DSF and ZBLAN fibers,[17] which would reduce the connection losses and allow to extend the spectrum further into the mid-infrared with increased power spectral density. Losses resulting from the non-perfect alignment of the cavity mirrors or from the chromatic aberration of the collimating lens could also be reduced with the use of a parabolic mirror. The measurement speed on the other hand is currently limited to 30 nm/min due to the monochromator scanning and long integration time needed to improve the signal-to-noise ratio. This could be significantly reduced by using a spectrometer with a detector array.[18]

This work was supported by the Academy of Finland (Grant No. 298463) and by the European Union Horizon 2020 research and innovation programme under Grant Agreement No. 722380 SUPUVIR. Caroline Amiot also acknowledges the Doctoral School of Tampere University of Technology.

[1]A. O'Keefe and D. A. Deacon, "Cavity ring-down optical spectrometer for absorption measurements using pulsed laser sources," Rev. Sci. Instrum. **59**, 2544–2551 (1988).

[2]D. A. Long, A. J. Fleisher, Q. Liu, and J. T. Hodges, "Ultra-sensitive cavity ring-down spectroscopy in the mid-infrared spectral region," Opt. Lett. **41**, 1612–1615 (2016).
[3]M. J. Thorpe, K. D. Moll, R. J. Jones, B. Safdi, and J. Ye, "Broadband cavity ringdown spectroscopy for sensitive and rapid molecular detection," Science **311**, 1595–1599 (2006).
[4]A. O'Keefe, "Integrated cavity output analysis of ultra-weak absorption," Chem. Phys. Lett. **293**, 331–336 (1998).
[5]J. Ye, L.-S. Ma, and J. L. Hall, "Ultrasensitive detections in atomic and molecular physics: Demonstration in molecular overtone spectroscopy," J. Opt. Soc. Am. B **15**, 6–15 (1998).
[6]R. Engeln, G. Berden, R. Peeters, and G. Meijer, "Cavity enhanced absorption and cavity enhanced magnetic rotation spectroscopy," Rev. Sci. Instrum. **69**, 3763–3769 (1998).
[7]S. E. Fiedler, A. Hese, and A. A. Ruth, "Incoherent broad-band cavity-enhanced absorption spectroscopy," Chem. Phys. Lett. **371**, 284–294 (2003).
[8]W. Ye, C. Li, C. Zheng, N. P. Sanchez, A. K. Gluszek, A. J. Hudzikowski, L. Dong, R. J. Griffin, and F. K. Tittel, "Mid-infrared dual-gas sensor for simultaneous detection of methane and ethane using a single continuous-wave interband cascade laser," Opt. Express **24**, 16973–16985 (2016).
[9]D. Richter, D. Lancaster, R. Curl, W. Neu, and F. Tittel, "Compact mid-infrared trace gas sensor based on difference-frequency generation of two diode lasers in periodically poled $LiNbO_3$," Appl. Phys. B **67**, 347–350 (1998).
[10]I. Armstrong, W. Johnstone, K. Duffin, M. Lengden, A. L. Chakraborty, and K. Ruxton, "Detection of CH_4 in the mid-IR using difference frequency generation with tunable diode laser spectroscopy," J. Lightwave Technol. **28**, 1435–1442 (2010).
[11]O. Mouawad, P. Béjot, F. Billard, P. Mathey, B. Kibler, F. Désévédavy, G. Gadret, J.-C. Jules, O. Faucher, and F. Smektala, "Filament-induced visible-to-mid-IR supercontinuum in a ZnSe crystal: Towards multi-octave supercontinuum absorption spectroscopy," Opt. Mater. **60**, 355–358 (2016).
[12]W. Chen, G. Mouret, D. Boucher, and F. Tittel, "Mid-infrared trace gas detection using continuous-wave difference frequency generation in periodically poled $RbTiOAsO_4$," Appl. Phys. B **72**, 873–876 (2001).
[13]I. Kubat, C. S. Agger, P. M. Moselund, and O. Bang, "Mid-infrared supercontinuum generation to 4.5 μm in uniform and tapered ZBLAN step-index fibers by direct pumping at 1064 or 1550 nm," J. Opt. Soc. Am. B **30**, 2743–2757 (2013).
[14]J. M. Langridge, T. Laurila, R. S. Watt, R. L. Jones, C. F. Kaminski, and J. Hult, "Cavity enhanced absorption spectroscopy of multiple trace gas species using a supercontinuum radiation source," Opt. Express **16**, 10178–10188 (2008).
[15]A. Aalto, G. Genty, T. Laurila, and J. Toivonen, "Incoherent broadband cavity enhanced absorption spectroscopy using supercontinuum and superluminescent diode sources," Opt. Express **23**, 25225–25234 (2015).
[16]J. M. Dudley, G. Genty, and S. Coen, "Supercontinuum generation in photonic crystal fiber," Rev. Mod. Phys. **78**, 1135–1184 (2006).
[17]K. Yin, B. Zhang, J. Yao, L. Yang, S. Chen, and J. Hou, "Highly stable, monolithic, single-mode mid-infrared supercontinuum source based on low-loss fusion spliced silica and fluoride fibers," Opt. Lett. **41**, 946–949 (2016).
[18]H. Kim, E. Plis, J. Rodriguez, G. Bishop, Y. Sharma, L. Dawson, S. Krishna, J. Bundas, R. Cook, D. Burrows *et al.*, "Mid-IR focal plane array based on type-II InAs/GaSb strain layer superlattice detector with nBn design," Appl. Phys. Lett. **92**, 183502 (2008).

PAPER IV

Short-range supercontinuum-based lidar for temperature profiling

A. Saleh, A. Aalto, P. Ryczkowski, G. Genty, and J. Toivonen

Optics letters, vol. 44, no. 17, pp. 4223-4226, 2019.
https://doi.org/10.1364/OL.44.004223

Optics Letters

Short-range supercontinuum-based lidar for temperature profiling

Abba Saleh,[1,2,*] Antti Aalto,[1] Piotr Ryczkowski,[1] Goery Genty,[1] and Juha Toivonen[1]

[1]Photonics Laboratory, Physics Unit, Tampere University, P.O. Box 692, FI-33101 Tampere, Finland
[2]Valmet Technologies Oy, Energy Services, Lentokentankatu 11, P.O. Box 109, FI-33101 Tampere, Finland
*Corresponding author: abba.saleh@tuni.fi

Received 24 June 2019; revised 20 July 2019; accepted 1 August 2019; posted 1 August 2019 (Doc. ID 370849); published 22 August 2019

We developed a short-range light detection and ranging system using a supercontinuum (SC) source spectrally tailored to cover the ro-vibrational transition energies of desired components of a flue gas. The system enables remote measurements of the gas parameters, including temperature and concentration which play a key role in the performance of combustion power plants. The technique requires only one inspection window and, thus, can be used in combustion units with limited access. It exploits differential absorption between specific wavelength bands of the gas absorption spectrum. The transmittance of an individual wavelength band is derived from the detected backscattered temporal intensity of the SC pulses. We demonstrate water vapor temperature measurement in the range of 400°C–900°C in a laboratory furnace with the use of only two wavelength bands. Using more than two wavelength bands, the technique can be further extended to simultaneously measure temperature and concentration. By varying the direction of the incident beam in a non-parallel plane, a full 3D profile is also obtainable.

https://doi.org/10.1364/OL.44.004223

Light detection and ranging (lidar) is a remote sensing technique [1] commonly used for the measurement of various atmospheric variables, including temperature, pressure, humidity, and trace gases concentration [1–6]. Lidar techniques have also been demonstrated for combustion diagnostics [7–10]. Typically, most of these methods are limited to the measurement of one species at a time as the laser wavelength is tuned to the absorption line of the investigated species. Recent advances in nonlinear fiber optics have led to the realization of spatially coherent and broadband light sources known as supercontinuum (SC) lasers. Under specific pumping conditions, the SC generation process exploits cascaded nonlinear dynamics resulting in highly directional broadband light [11]. This opens the door for simultaneous detection of multiple observables. Thus, supercontinuum light detection and ranging (SC-lidar) [12,13] and SC-based hyperspectral lidar [14,15] have shown great potential for simultaneous detection of multiple variables. To the best of our knowledge, an approach based on short-range (~1 – 10 m) SC-lidar for temperature measurement in combustion power plants is yet to be reported in the literature.

Temperature distribution inside a furnace is one of the main factors affecting the performance of combustion units (CUs). The ability to accurately measure the temperature inside a CU would pave the way for precise control and management of the combustion processes. Conventionally, thermocouples are used for temperature measurement in CUs [16]; however, this approach is inefficient because of its point-wise nature and ineffective for dynamic temperature monitoring due to the poor response of the thermocouple to fluctuating temperatures [17]. Other prior art solutions besides the lidar approach in Refs. [7–10] include spectroscopic methods such as thermometry based on thermographic phosphors [18], two-line thermometry employing wavelength modulation spectroscopy [19–21] and atomic fluorescence [22]. Another important technique is collinear photo fragmentation and atomic absorption spectroscopy, which utilizes chemical reaction kinetics to measure temperature [23]. The aforementioned promising optical spectroscopic methods detect signal transmitted through the examined space, thus requiring at least two openings in the furnace walls, which limits their detection area to the line between those openings.

Herein, we present a new method for non-intrusive combustion diagnostics based on an SC-lidar using just one opening. The approach is robust as the stringent requirement of a narrowband laser linewidth being precisely in tune with the absorption line of the probe gas, particularly in the aforementioned techniques, is mitigated by the broadband SC laser. The technique exploits the gas absorption cross-sectional dependence on temperature between wavelength bands. Consequently, the absorption strength of water vapor (H_2O) varies as a function of temperature, as shown in Fig. 1. We studied the temporal dynamics of H_2O temperatures in a laboratory furnace using just two wavelength bands. By measuring the temporal intensities of the backscattered SC light, the corresponding transmittance of individual wavelength band can be deduced, hence providing information indicative of differential absorption between the two wavelength bands. H_2O temperatures in the range of 400°C–900°C were inferred by comparing the transmittance ratio between these two wavelength bands.

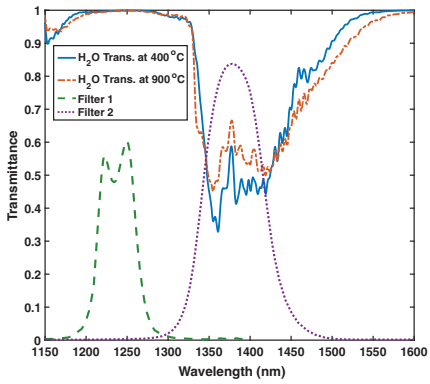

Fig. 1. Modeled H_2O transmittance spectra for two temperatures and an overlay of filter transmissions. Blue (—) and orange (– - -) are the H_2O transmittance spectra at 400°C and 900°C, respectively. Green (– –) and purple (.) are the corresponding filter transmissions for Ch1 and Ch2, respectively.

The SC-lidar signal (i.e., the detected back scattered signal) can be expressed as

$$S(t) = \frac{C_{\text{eff}}}{d_t^2} \int P_0(\lambda)\beta(\lambda) e^{\left(-\sigma(\lambda)\frac{N}{V}2l\right)} \mathrm{d}\lambda, \tag{1}$$

where $P_0(\lambda)$ is the initial spectrum of the SC laser; $\beta(\lambda)$ is the backscattering coefficient; C_{eff} is the collection efficiency; d_t is the distance travelled by the scattered light pulse at a given time t and can be obtained from the time of flight of the light pulse; l is the length of the absorbing medium, and the factor of two is attributed to the round trip by an SC light pulse; $\frac{N}{V}$ is the molecular number density and $\sigma(\lambda)$ is the wavelength-dependent absorption cross section (attenuation is considered to be only due to absorption). σ further depends on temperature via the line intensity in the spectrum and depends both on temperature and pressure via the line profile.

When two wavelength bands are used to probe flue gas parameters (as in Fig. 2), the corresponding signals detected at an individual wavelength band at a given time can be written as

$$S_1(t_1) = C_{\text{eff}1} \frac{\beta}{d_1^2} \int P_{01}(\lambda) \mathrm{d}\lambda, \tag{2}$$

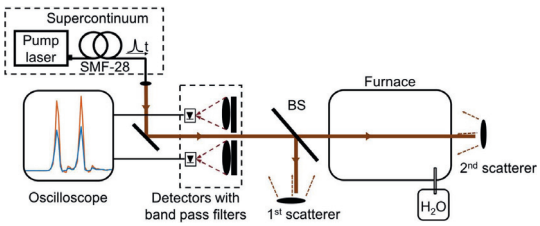

Fig. 2. Schematic diagram of the experimental setup. BS: beam splitter.

$$S_1(t_2) = C_{\text{eff}1} \frac{\beta}{d_2^2} \int P_{01}(\lambda) e^{\left(-\sigma_1(\lambda)\frac{N}{V}2l\right)} \mathrm{d}\lambda, \tag{3}$$

$$T_1 = \frac{S_1(t_2)}{S_1(t_1)} = \left(\frac{d_1}{d_2}\right)^2 \frac{\int P_{01}(\lambda) e^{\left(-\sigma_1(\lambda)\frac{N}{V}2l\right)} \mathrm{d}\lambda}{\int P_{01}(\lambda)\mathrm{d}\lambda}, \tag{4}$$

where S_1 is the signal detected at the first wavelength band (Ch1); t_1 and t_2 are the times of flight of the light pulse in relation to the first and second scatterers, respectively; d_1 and d_2 are the corresponding distances travelled by the light pulse at the time t_1 and t_2; β is the backscattering coefficient, which is considered to be constant because the scatterers are large compared to the wavelength of the light; $C_{\text{eff}1}$, $P_{01}(\lambda)$, $\sigma_1(\lambda)$, and T_1 are the collection efficiency, initial spectrum of the SC, absorption cross section, and transmittance at Ch1, respectively. Similarly, the transmittance at the second wavelength band (Ch2) can be given as

$$T_2 = \left(\frac{d_1}{d_2}\right)^2 \frac{\int P_{02}(\lambda) e^{\left(-\sigma_2(\lambda)\frac{N}{V}2l\right)} \mathrm{d}\lambda}{\int P_{02}(\lambda)\mathrm{d}\lambda}. \tag{5}$$

The transmittance ratio R of Ch2 to Ch1 is obtained by dividing Eq. (5) by (4):

$$R = \frac{\int P_{02}(\lambda) e^{\left(-\sigma_2(\lambda)\frac{N}{V}2l\right)} \mathrm{d}\lambda}{\int P_{02}(\lambda)\mathrm{d}\lambda} \frac{\int P_{01}(\lambda)\mathrm{d}\lambda}{\int P_{01}(\lambda) e^{\left(-\sigma_1(\lambda)\frac{N}{V}2l\right)} \mathrm{d}\lambda}. \tag{6}$$

Note that the process is self-calibrating, as the backscattering coefficients, as well as the collection efficiency of both Ch1 and Ch2 cancels out.

The transmission spectrum of H_2O, one of the main combustion products with a relatively high concentration and a rich absorption spectrum in the entire infrared, was thoroughly investigated. Specifically, the transmission spectrum of H_2O corresponding to a 100% concentration, a pressure of 1 atm, and an interaction length of about 1 m was modeled using the HITRAN 2012 database [24], as shown in Fig. 1. Note that the aforementioned H_2O parameters correspond to an equivalent optical thickness of the ideal power plant conditions. Typically 10% H_2O concentration, 10 m interaction length and a pressure of 1 atm. Based on the data presented in Fig. 1, two wavelength bands, namely, channel one (Ch1) and two (Ch2), were carefully selected. They are characterized by different responses of absorption to the temperature variation which allows for differential absorption measurement.

Figure 2 depicts the schematic of the experimental setup. The SC is generated by a cascaded Raman process in a 500 m long SMF-28 fiber (Thorlabs), pumped by KEOPSYS PYFL-KULT laser operating at 1064 nm and generating 2 ns long, 1 kW peak power pulses with a repetition rate of 280 kHz. The output spectrum of the source is presented in Fig. 3. SC light is collimated with a reflective collimator and guided towards ~1 m long quartz tube furnace containing 100% H_2O concentration at atmospheric pressure. Using a 50:50 beam splitter (BPD508-G, Thorlabs), part of the incident light is directed towards the 1st scatterer/diffuser (DG10-1500-P01, Thorlabs), placed just before the furnace. The rest of the beam traverses through the furnace undergoing absorption and, subsequently, scattered by the 2nd scatterer behind the furnace. In an ideal combustion environment, the role

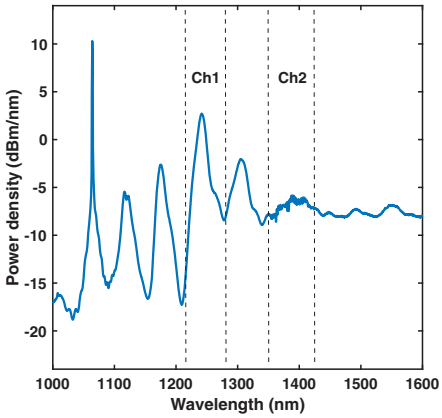

Fig. 3. SC spectrum and the corresponding FWHM position of the filters (Ch1 and Ch2) in the spectrum.

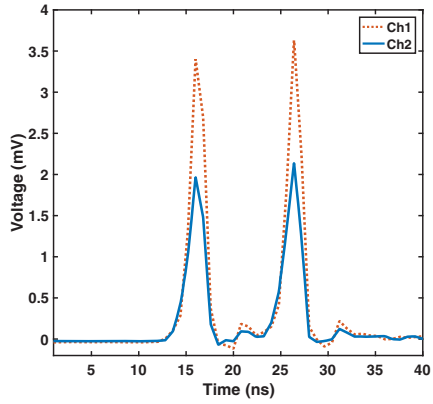

Fig. 4. Measured backscattered signals with no H_2O present in the furnace. The first and second peaks are the signals from the 1st and 2nd scatterers, respectively. The dotted line represents the Ch1 signal, while the solid line represents Ch2 signal.

of the scatterers is played by the naturally present aerosol particles which also provides sufficient scattering that enables signal detection over relatively long distances within the CU. Note that aerosol scattering is weak compared to that of the scatterers used in this experiment; hence, additional electronic pre-amplification of the signal will be required. The signal from the 2nd scatterer passes through the furnace again on the way back. The backscattered light from both scatterers is collected by two lens sets (AC254-030-C & AC254-075-C, Thorlabs) placed adjacent to each other, filtered by Ch1 and Ch2 filters (BP-1375-085 & BP-1240-050, Spectrogon) and focused on to the active area of two biased photodetectors (DET08C, Thorlabs). The temporarily resolved signal is recorded by a 12-bit oscilloscope (HDO6054, Lecroy). An example recorded signal is shown in Fig. 4.

The two distinct peaks separated in time represent the signals from the 1st and 2nd scatterers, respectively. The signal plotted in the figure is an average of 10,000 backscattered pulses, and the corresponding measurement time is about 40 ms. Furthermore, the measured temporal intensities of both channels are converted into individual channel transmittance using Eqs. (4) and (5). Figure 5 shows the measured transmittance of Ch1 and Ch2 at varying furnace temperatures of 400°C–900°C. The measurement at a given temperature composes 20 sets of measurement, with each measurement further composed of 10,000. Ch1 shows no change in transmittance with furnace temperature, while Ch2 shows an increase in transmittance with increasing furnace temperature, which is in good agreement with the modeled H_2O transmittance in Fig. 1. The standard deviation of the transmittance measurement, calculated based on 20 measurement repetitions of 10,0000 pulses, presented in Fig. 5 is 0.0024, with the mean value of transmittance ranging from 0.4704 to 0.5837, depending on the channel and temperature.

In order to infer the temperature of H_2O, the transmittance ratio R was calculated using Eq. (6). The mean value of all 20 measurements, which composes 200,000 pulses at a given temperature, was used in the calculation. The simulated and experimentally measured R as a function of the furnace

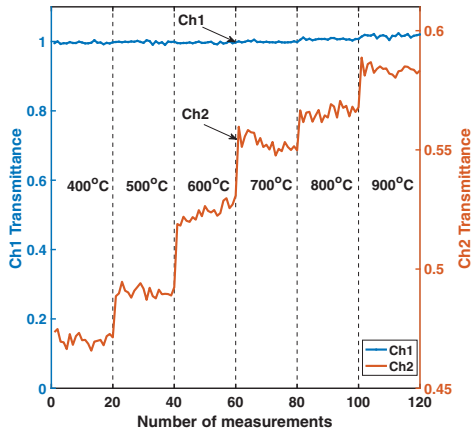

Fig. 5. Measured Ch1 (blue line) and Ch2 (orange line) transmittance with respect to furnace temperature. The measurement was carried out for a temperature range of 400°C–900°C, with 20 sets of measurement per temperature and each single measurement composing of 10,000 pulses.

temperature are compared in Fig. 6. We can see very good agreement between the simulated and experimentally measured ratios with a 50°C accuracy in the range 600°C–900°C. However, at lower furnace temperatures (400°C–500°C), the discrepancy between the simulated and measured ratios is more pronounced. This is because the quartz tube (i.e., the gas cell) extends a few centimeters outside the furnace heating zone on either sides of the furnace, thus creating a colder interface (i.e., temperature gradient) with respect to the internal part of the furnace (i.e., the heating zone). The colder region was measured to be less than 100°C. As a result, H_2O in these regions begins to condensate which yields additional loses on the beam

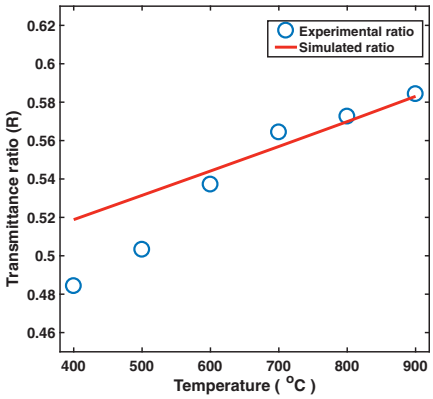

Fig. 6. Experimentally measured (circles) and simulated (solid line) transmittance ratios as a function of temperature.

path that are not accounted for in our model. Moreover, the temperature difference between the colder region and the heating zone was persistent, even at elevated furnace temperatures. Hence, the assumption of uniform H_2O temperature and concentration inside the furnace is partially violated by the presence of the colder regions in the test tube outside the furnace heating zone. Therefore, condensations of H_2O at lower furnace temperatures (400°C–500°C) coupled with the alteration of H_2O concentration due to interference from the colder regions at all furnace temperatures, have led to the observed discrepancies between the simulated and experimentally measured transmittance ratios in Fig. 6.

In summary, we have reported a novel technique based on a short-range SC-lidar for temperature measurement in CUs via a single opening. Water vapor with optical thickness equivalent to combustion power plant conditions was mimicked in a laboratory quartz tube furnace. H_2O temperatures were inferred from the transmittance ratio between two distinct wavelength bands. The measured and simulated H_2O temperatures were observed to be in a good agreement. The 2 ns duration of the spectrally filtered SC pulses should allow for a spatial resolution of about 30 cm with this technique in a case where scatterers are present all along the measurement path, as is the case in a combustion furnace. In addition, the SC pulses have significantly high peak power with a duty cycle of 0.0005, thus preventing any potential interference by thermal emissions such as black body radiations and chemiluminescence, from the furnace environment. Moreover, the same technique can be employed for simultaneous detection of temperature and concentration if multiple (i.e., more than two) wavelength bands of the SC spectrum are utilized in the combustion diagnosis, e.g., by adding an additional bandpass filter in the 1450–1550 nm spectral region. Finally, we emphasize that the technique possesses a great potential for simultaneous 3D mapping of both temperature and concentration, which can be achieved by varying the direction of the probe beam in a non-parallel plane.

Funding. Horizon 2020 Framework Programme (722380); Academy of Finland (320165).

REFERENCES

1. C. Weitkamp, *Lidar: Range-Resolved Optical Remote Sensing of the Atmosphere* (Springer, 2006), Vol. **102**.
2. S. H. Melfi, K. D. Evans, J. Li, D. Whiteman, R. Ferrare, and G. Schwemmer, Appl. Opt. **36**, 3551 (1997).
3. J. W. Hair, L. M. Caldwell, D. A. Krueger, and C.-Y. She, Appl. Opt. **40**, 5280 (2001).
4. G. Megie and R. T. Menzies, Appl. Opt. **19**, 1173 (1980).
5. Y. Zhao, Appl. Opt. **39**, 997 (2000).
6. J. L. Machol, T. Ayers, K. T. Schwenz, K. W. Koenig, R. M. Hardesty, C. J. Senff, M. A. Krainak, J. B. Abshire, H. E. Bravo, and S. P. Sandberg, Appl. Opt. **43**, 3110 (2004).
7. T. Leffler, C. Brackmann, A. Ehn, B. Kaldvee, M. Aldén, M. Berg, and J. Bood, Appl. Opt. **54**, 1058 (2015).
8. B. Kaldvee, A. Ehn, J. Bood, and M. Aldén, Appl. Opt. **48**, B65 (2009).
9. B. Kaldvee, J. Bood, and M. Aldén, Meas. Sci. Technol. **22**, 125302 (2011).
10. E. Malmqvist, M. Brydegaard, M. Aldén, and J. Bood, Opt. Express **26**, 14842 (2018).
11. J. M. Dudley, G. Genty, and S. Coen, Rev. Mod. Phys. **78**, 1135 (2006).
12. S. Kaasalainen, T. Lindroos, and J. Hyyppa, IEEE Geosci. Remote. Sens. Lett. **4**, 211 (2007).
13. G. Méjean, J. Kasparian, E. Salmon, J. Yu, J.-P. Wolf, R. Bourayou, R. Sauerbrey, M. Rodriguez, L. Wöste, H. Lehmann, B. Stecklum, U. Laux, J. Eislöffel, A. Scholz, and A. P. Hatzes, Appl. Phys. B **77**, 357 (2003).
14. Y. Chen, E. Räikkönen, S. Kaasalainen, J. Suomalainen, T. Hakala, J. Hyyppä, and R. Chen, Sensors **10**, 7057 (2010).
15. A. Manninen, T. Kääriäinen, T. Parviainen, S. Buchter, M. Heiliö, and T. Laurila, Opt. Express **22**, 7172 (2014).
16. D. Bradley and K. Matthews, J. Mech. Eng. Sci. **10**, 299 (1968).
17. M. Tagawa and Y. Ohta, Combust. Flame **109**, 549 (1997).
18. M. Aldén, A. Omrane, M. Richter, and G. Särner, Prog. Energy Combust. Sci. **37**, 422 (2011).
19. J. Liu, J. Jeffries, and R. Hanson, Appl. Phys. B **78**, 503 (2004).
20. X. Zhou, J. Jeffries, and R. Hanson, Appl. Phys. B **81**, 711 (2005).
21. G. B. Rieker, J. B. Jeffries, and R. K. Hanson, Appl. Opt. **48**, 5546 (2009).
22. J. Borggren, W. Weng, A. Hosseinnia, P.-E. Bengtsson, M. Aldén, and Z. Li, Appl. Phys. B **123**, 278 (2017).
23. J. Viljanen, T. Sorvajärvi, and J. Toivonen, Opt. Lett. **42**, 4925 (2017).
24. L. Rothman, I. Gordon, Y. Babikov, A. Barbe, D. C. Benner, P. Bernath, M. Birk, L. Bizzocchi, V. Boudon, L. Brown, A. Campargue, K. Chance, E. Cohen, L. Coudert, V. Devi, B. Drouin, A. Fayt, J.-M. Flaud, R. Gamache, J. Harrison, J.-M. Hartmann, C. Hill, J. Hodges, D. Jacquemart, A. Jolly, J. Lamouroux, R. L. Roy, G. Li, D. Long, O. Lyulin, C. Mackie, S. Massie, S. Mikhailenko, H. Müller, O. Naumenko, A. Nikitin, J. Orphal, V. Perevalov, A. Perrin, E. Polovtseva, C. Richard, M. Smith, E. Starikova, K. Sung, S. Tashkun, J. Tennyson, G. Toon, V. Tyuterev, and G. Wagner, J. Quant. Spectrosc. Radiat. Transf. **130**, 4 (2013).. HITRAN2012 special issue.